Turbulence and transport in magnetic islands in MST and DIII-D

by
Lucas Anthony Morton

A disseration submitted in partial fulfilment of
the requirements for the degree of

Doctor of Philosophy
(Physics)

at the
UNIVERSITY OF WISCONSIN - MADISON
2016

Date of final oral examination: 08/01/2016

The dissertation is approved by the following members of the Final Oral Committee:

Daniel J. Den Hartog, Research Professor, Physics

Chris Hegna, Professor, Engineering Physics

Carl Sovinec, Professor, Engineering Physics

John Sarff, Professor, Physics

Oliver Schmitz, Professor, Engineering Physics

Acknowledgments

> *It always takes longer than you think even when you take Hofstadter's Law into account.*
>
> — Hofstadter's Law

MST has been a very friendly and rewarding place to work. I am grateful to Daniel Den Hartog for his patience and support. Fellow Thomson scattering folks Eli Parke, Josh Reusch, Hillary Stephens, Steph Kubala, Mike Borchardt, Craig Jacobson, and Bill Young have also been helpful and pleasant to work with. Thanks also to the other IDA group members (including Lisa Reusch and Mark Nornberg) for their feedback on my presentations. Thanks to Brett Chapman for teaching me the ways of PPCD. Thanks to Andrew Seltzman for falling asleep at the operator's console, resulting in run-away density and leading to the hot island observation. Thanks to Bill Young for getting the Fast Laser to work.

I am appreciative of valuable discussions with Chris Hegna, Daniel Den Hartog, and John Sarff that have improved my understanding of plasma physics and academic life in general. I also thank Karsten McCollam for his dedication in asking good questions at student presentations.

The Hackers (Alex Squitieri, Andrey Levochkin, and Paul Wilhite) deserve a round of applause for holding the MST computing system together while still being approachable and helpful. Thanks to Christine Hrenak and Reneé Lefkow for their highly competent and friendly support in administrative matters. For technical support and instruction, Bill Zimmerman, Peter Weix, Don Holly, Mark Thomas, Mikhail Reyfman, and Dave Deicher all have my thanks. Thanks go out to the (late) Yuri Tsidulko for help with MAL.

A huge thank-you to George McKee for making it possible for me to travel to DIII-D and participate in the island turbulence experiment. Craig Petty, Morgan Shafer, Makoto Ono, Zheng Yan, and László Bardóczi were also particularly helpful during my visit and afterwards.

I thank my friends here in Madison for keeping me sane and entertained during my time in graduate school. It has been great getting to know you all and enjoying Madison together.

Special thanks to my family. To David, for keeping in touch and being a great listener. To Mom and Dad, for providing my education and encouraging my curiosity. Thanks to Dad for proofreading this thesis and asking good questions.

Abstract

Magnetic islands in the Madison Symmetric Torus (MST) reversed-field pinch (RFP) exhibit varying degrees of overlap, sometimes resulting in complex partially chaotic magnetic field regions. Although prior measurements of thermal confinement in highly chaotic magnetic field regions in MST showed good agreement with a stochastic transport model, the low-chaos case was not studied in detail. In this work, the high-repetition rate (25 kHz) Thomson scattering (TS) laser at MST probed electron temperature T_e fluctuations correlated with $m = 1, n = 5 - 7$ tearing modes, which rotate at 10 to 20 kHz. Bayesian statistical methods allow extraction of the modes' T_e structures from large datasets. The T_e fluctuations of adjacent modes overlap significantly, suggesting that magnetic chaos exists. Nonetheless, the strong higher-harmonic content of the $n = 6$ mode T_e fluctuations indicates confinement of Ohmic heating within the island leading to a local T_e peak. A new, higher repetition-rate (66 - 333 kHz) TS laser developed at MST captured for the first time in an RFP a 2D picture of the T_e structure of a magnetic island-shaped chaotic structure during a single discharge. This large $n = 6$ structure exhibited peaked internal T_e. Magnetic field modeling indicates that chaotic magnetic field lines fill most of the former island volume, due to overlap of the $n = 6$ island with the smaller neighboring $n = 7, 8$ islands. Modeling of transport in the chaotic magnetic field yields an effective perpendicular electron thermal conductivity of $\chi_{e,m} \approx 30\,\mathrm{m}^2/\mathrm{s}$, in good agreement with the inferred conductivity $\chi_{e,th} \approx 20\,\mathrm{m}^2/\mathrm{s}$ based on inferred Ohmic heating and the observed T_e gradient inside the island. This demonstrates that magnetic structures with reduced chaos can exhibit sufficient confinement to develop appreciable T_e peaking when Ohmically heated. A complimentary experiment probing turbulence in a magnetic island was conducted in the DIII-D tokamak. A large $m = 2, n = 1$ magnetic island was induced by an external control coil. The beam emission spectroscopy diagnostic provided a 2D map of long-wavelength electron density fluctuations as control coils rotated the island past the diagnostic. Preliminary analysis shows, as expected, strong turbulence suppression inside the island O-point and enhancement near the X-point, compared to the turbulence in the absence of an island.

Contents

List of Figures

1 Introduction

> *An argument which makes it clear intuitively* why *a result is correct is actually more trustworthy, and more likely of a permanent place in science, than is one that makes a great overt show of mathematical rigor unaccompanied by understanding.*
>
> — E. T. Jaynes, Preface to *Probability Theory: The Logic of Science [1]*

This thesis is focused on turbulence and transport inside magnetic islands in toroidal magnetic fusion experiments. The research in this thesis was conducted on two devices: the Madison Symmetric Torus (MST) reversed-field pinch (RFP) [2] and the DIII-D tokamak [3]. MST is a good test-bed for studying transport in chaotic magnetic fields created by the overlap of tearing mode magnetic islands. The experiments on MST focused on electron thermal transport in chaotic magnetic islands. On the other hand, DIII-D is well-equipped for studies of electrostatic drift wave turbulence. The experiment at DIII-D probed electron density turbulence in externally-imposed magnetic islands. The experiments conducted on each device relied on high-resolution diagnostics: Thomson scattering (TS) in MST for electron temperature measurements, and beam emission spectroscopy (BES) in DIII-D for electron density fluctuations measurements.

Although DIII-D and MST differ in important ways, the physics topics of magnetic islands, chaos, and turbulence are shared by both the RFP and the tokamak. Understanding tur-

bulence and transport within and around magnetic islands is important in several contexts. Control of transport and instabilities in the plasma edge may involve magnetic islands [4] and chaotic magnetic fields [5]. In the RFP, a promising route to improved confinement involves large magnetic islands or helical structures that reduce magnetic chaos [6]. Transport inside magnetic islands also influences neoclassical tearing mode stability, a major concern for tokamak fusion devices [7, 8]. This thesis adds to the knowledge base about transport and turbulence within magnetic islands.

Section 1.1 provides a brief description of some of the challenges of achieving fusion conditions and of how these challenges are addressed in magnetic confinement devices. In Section 1.2, key concepts and terminology of plasma physics and magnetically-confined fusion devices are reviewed. Section 1.3 describes the MST RFP, with which most of this thesis is concerned. The DIII-D tokamak, the subject of Chapter 4, is introduced in Section 1.4. Section 1.5 presents the main results.

1.1 Magnetic confinement fusion

Nuclear fusion offers the possibility for a practically unlimited supply of energy. Nuclear fusion powers the sun, transmuting hydrogen isotopes into helium. Compared to a nuclear fission reactor, a fusion reactor would produce less hazardous radioactive waste. Fusion reactors are inherently incapable of meltdowns, unlike nuclear fission reactors. Thus, many nations around the world are researching fusion energy as an alternative to fossil fuels and fission power.

Like chemical combustion, nuclear fusion reactions require the reactants to be heated to high temperature before the reaction can take place. However, fusion reactions involve colliding

nuclei at high velocity, thus requiring much higher temperatures (around one hundred million °C). At these temperatures, collisions strip the electrons away from atoms, resulting in a gas of ions and electrons. This is a state of matter called plasma. Unlike a gas, the free charges in a plasma allow it to carry electric current and react to magnetic fields. In some circumstances a plasma may be accurately described by the same set of equations (called magnetohydrodynamics or MHD) that apply to liquid metals or other conducting fluids.

Properly designed magnetic fields provide an effective means of confining plasma and preventing heat loss to the walls. Charged particles move in circular or helical gyro-orbits around magnetic field lines. Thus, plasma can travel freely along magnetic field lines, but motion perpendicular to field lines is impeded. (In an idealized situation, there would be no perpendicular transport at all. However, other factors such as electric fields and collisions between particles result in plasma transport perpendicular to field lines.) Plasma loss along field lines is eliminated by forming a closed surface in space with a strong magnetic field that is always parallel to the surface. In this arrangement, no field lines penetrate the surface. Such a surface is called a flux surface. In three-dimensional space, all closed flux surfaces with non-zero magnetic field must be topologically equivalent to a torus. Thus, the most effective magnetic confinement devices are toroidally-shaped. A review paper that covers the logic of magnetic confinement fusion design is Ref. [9].

Steep gradients in temperature and density exist between the hot plasma core and the cold plasma edge that contacts the walls. These gradients can become unstable to small-scale instabilities, resulting in turbulent transport. Turbulence can expel energy from the plasma much faster than the absolute minimum rate imposed by collisions between particles. Large-scale instabilities may also occur, disrupting the entire plasma. Understanding and controlling instabilities and turbulence in plasma is critical for making fusion a viable power source.

Heating the plasma may be achieved by inductively driving current through the resistance of the plasma (Ohmic heating), or by injecting radio waves (RF heating) or neutral particle beams (NBI heating). The heat generated by the fusion reactions may be used to run a steam turbine to produce electrical power. If the plasma is sufficiently well confined, the fusion reactions provide enough power to heat new fuel and overcome losses, without requiring external heating input power. This is called a 'burning' plasma. The first ignition of a burning plasma in the laboratory is tantalizingly close. For short periods, the JET tokamak produced almost the same amount of fusion power as the amount of input heating power (16 megawatts, which is several times the power of a large wind turbine) [10]. ITER, a very large tokamak under construction, is expected to demonstrate the world's first sustained burning plasma. The ITER website [11] is a good resource for general information about fusion energy.

1.2 Key concepts

Both the RFP and the tokamak are toroidal magnetic confinement devices which are nominally rotationally symmetric about their central axis. Refer to Figure 1.1 for depiction of a torus and definition of coordinates used to describe a toroidal system. Currents flowing poloidally in conductors outside the plasma create a toroidal magnetic field (pointing the long way around the torus) inside the plasma. A poloidal component to the magnetic field (the short way around the torus) is added by driving toroidal current in the plasma itself. The tokamak is characterized by a very strong toroidal magnetic field, and a weak poloidal field. The word 'tokamak' is derived from a Russian acronym for a toroidal chamber with a magnetic field. The RFP [12] has a poloidal magnetic field comparable to its toroidal magnetic field. The toroidal field in an RFP is directed oppositely in the plasma edge as it

is in the core, which is how the name 'reversed field pinch' originated. (The term 'pinch' refers to compression of plasma by magnetic forces.)

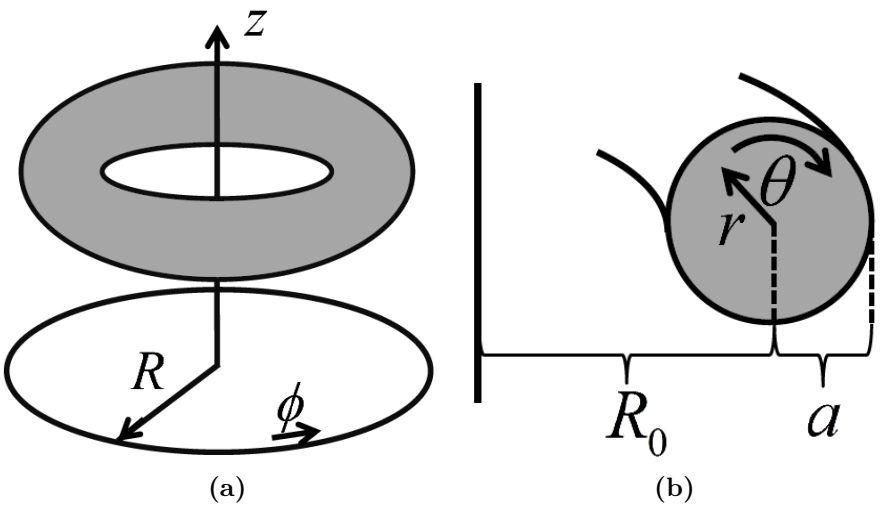

Figure 1.1: (a) A cylindrical coordinate system can be used to a describe a general toroid, produced by rotating a closed curve in the $R-z$ plane around the z-axis. R is referred to as the major radius, and ϕ is the toroidal angle. (b) The minor radius r and poloidal angle θ describe locations in the poloidal plane ($\phi = const.$ surface). The ratio R_0/a of device major radius R_0 to the device minor radius a is called the aspect ratio

1.2.1 Flux surfaces and safety factor

As mentioned in the previous section, a flux surface is a surface such that the magnetic field $\boldsymbol{B}$ on the surface is always purely tangent to the surface: $\boldsymbol{B} \cdot \boldsymbol{n} = 0$, where $\boldsymbol{n}$ is a normal vector, perpendicular to the flux surface. This implies that a magnetic field line which starts on the surface remains on it always, because there is no component of $\boldsymbol{B}$ that points off of the flux surface. Flux surfaces are not guaranteed to exist in general. The simplest way to ensure that a magnetic field has flux surfaces is to make the field rotationally symmetric about a central axis, as in an RFP or tokamak. Each flux surface is then a toroid. The flux surfaces are nested one inside the other in the interior of the device. This situation is

illustrated in Figure 1.2 for MST.

A purely toroidal magnetic field (B_ϕ) has poor confinement due to radially outward drifts of particles due to the compression of the magnetic field on the inboard side of the torus. Thus, RFP and tokamak devices have a toroidal current in the plasma to produce a poloidal magnetic field component (B_θ) that causes the field lines on a flux surface to wind helically around the surface (refer to Figure 1.2 for the RFP case). The safety factor $q(r)$ measures the helical pitch of the magnetic field lines on a flux surface. The safety factor can be calculated as the average over a flux surface of the local magnetic field line pitch:

$$q(r) = \left\langle \frac{rB_\phi}{RB_\theta} \right\rangle . \tag{1.1}$$

If the q-profile is a smooth function, it will take on irrational values at almost all radii. When the value is irrational, a field line never arrives again exactly where it started. Instead, a single field line comes arbitrarily close to any point on the surface if followed far enough. Because field lines in such a flux surface provide a direct connection between distant parts of the surface, flux surfaces tend to be surfaces on which other plasma properties (such as temperature and density) are constant. Thus in some respects the system is effectively one-dimensional in terms of the flux surface radius. The centermost flux 'surface' is a circle called the magnetic axis. The radius of the magnetic axis may be slightly larger than the device major radius due to the outward Shafranov shift of the flux surface (illustrated in Figure 1.6).

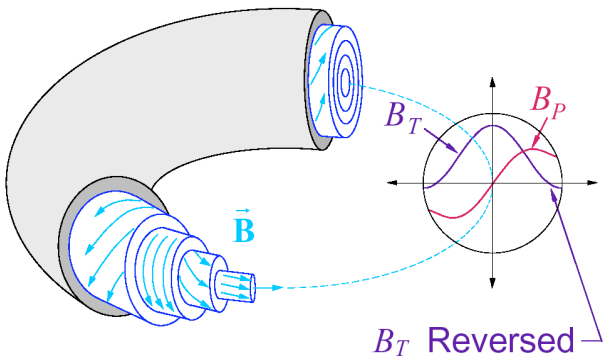

Figure 1.2: Flux surfaces in MST are nested toroids. The magnetic field lines wind around the flux surfaces at different pitches moving from the core to the edge. The toroidal component B_T of the magnetic field reverses direction in the edge, while the poloidal component B_p does not. The dashed line is magnetic axis. (Courtesy of Prof. John Sarff.)

1.2.2 Magnetic islands

In the laboratory, symmetry is difficult to achieve. It is natural to ask what happens when a non-axisymmetric magnetic field is added to the ideal picture of nested toroidal flux surfaces. If a helical perturbation is added, it may create a magnetic island. A magnetic island is a pocket or a 'blister' that opens in a magnetic flux surface (Figure 1.3). The wide part of the pocket contains the 'O-point', which forms a secondary, helical magnetic axis for the new closed flux surfaces of the island. The island is separated from the remaining toroidal flux surfaces on either side by a layer called the separatrix. The separatrix intersects itself at the 'X-point.' As the width of an island grows, flux surfaces are pushed toward the X-point where they 'tear' and reconnect in a process known as magnetic reconnection. Magnetic reconnection relies on some form of plasma resistance near the X-point to proceed. If the plasma were a perfect conductor (which is a good approximation in some other instances), no reconnection could take place. The tearing mode is an instability, driven by pressure or current density gradients, that results in the formation of a magnetic island.

Magnetic islands form at the location where the helicity of the original field lines is equal and opposite to the helicity of the perturbation. More formally, the perturbation is a wave described by $\boldsymbol{B}_{pert}(r,\theta,\phi) = \boldsymbol{B}_{pert}(r)\cos(\boldsymbol{k}\cdot\boldsymbol{x}+\delta)$, with $\boldsymbol{k} = m\hat{\boldsymbol{\theta}}+n\hat{\boldsymbol{\phi}}$ and $\boldsymbol{x} = r\hat{\boldsymbol{r}}+\theta\hat{\boldsymbol{\theta}}+\phi\hat{\boldsymbol{\phi}}$. The poloidal and toroidal mode numbers (integers m and n respectively) define how many periods of the wave there are in one poloidal or toroidal transit. The perturbation is said to be resonant where $\boldsymbol{k}\cdot\boldsymbol{B}_0 = 0$. This condition means that the wave vector $\boldsymbol{k}$ is perpendicular to the field lines of the background field $\boldsymbol{B}_0$. Where this condition holds, the wave displaces the flux surfaces the most. The resonance condition can be rewritten as $q(r) + m/n = 0$. The 'rational surface' is the flux surface for which $q(r) = -m/n$ is satisfied. The slope of q helps determines how wide a magnetic island will be. A shallower slope in q brings about a wider island, all else being equal. An approximate expression for the magnetic island width is [13]

$$w = 4\sqrt{\frac{rB_r}{nB_\theta(dq/dr)}}, \tag{1.2}$$

where B_r is from the perturbation and B_θ is from the background field, and all quantities are evaluated at the rational surface.

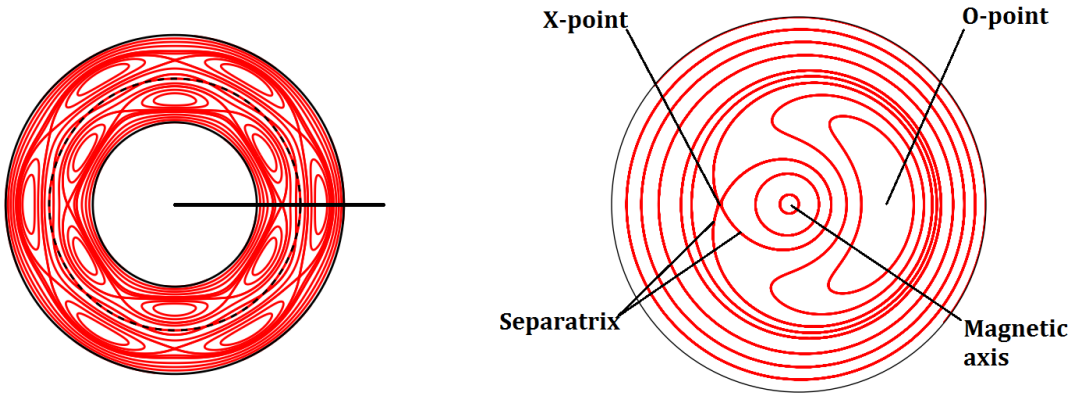

Figure 1.3: (a) Top view of MST with a very large $m, n = 1, 6$ magnetic island. The dashed black line is the geometric axis. (b) Poloidal cross-section of the same island, taken at the plane indicated by the solid black line in (a).

1.2.3 Magnetic chaos

When two or more magnetic islands with different helicities begin to interact, the behavior of the field lines becomes more complex. The field no longer has a direction of symmetry, and some field line paths no longer lie on flux surfaces, but instead move throughout a volume of space in a manner which appears random. This is called chaos. Figure 1.4 illustrates the development of chaos as two magnetic islands simultaneously grow in size. Varying degrees of chaos are possible. There may exist regions of chaos mixed interspersed with isolated regions of flux surfaces, as well as lingering order within the chaotic volume. One may be justified in approximating the field line motion as 'stochastic' or pseudo-random when the degree of chaos is sufficiently high.

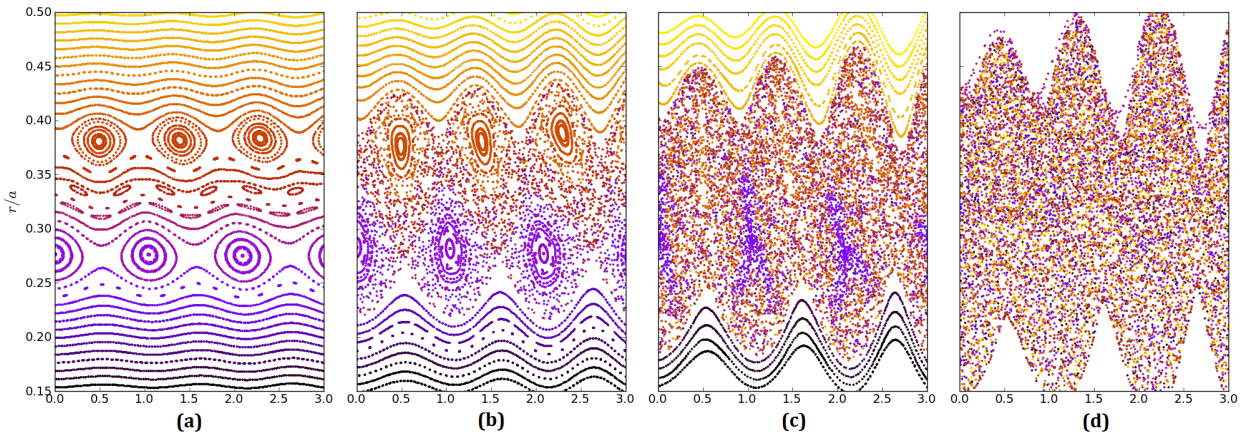

Figure 1.4: Development of field line chaos as two magnetic islands with different helicities (and hence different rational surfaces) are simultaneously increased in width (moving left to right). The horizontal axis is the toroidal angle ϕ in radians. The vertical axis is the minor radius r normalized to the vessel minor radius a. Only half of the full toroidal angle is shown for brevity. (a) At low amplitude, the islands are separated by good flux surfaces. (b) The separatrices are lost to chaos, and no good flux surfaces separate the islands, which are now remnant islands (c) All the island flux surfaces are gone, but effect of the lower island remains in the form of a 'Y'-shaped region where only field lines colored purple can enter (given a limited field line length). (d) At sufficiently large amplitude, no residual structure is visible inside the chaotic region.

Magnetic chaos can enhance transport of particles and energy in a plasma. In a fusion-energy context, enhancement of transport is often undesirable because the chief difficulty lies in containing plasma energy stably for a long time. However, in some experiments islands [4] or chaotic magnetic fields [5, 14] are induced at the edge of a plasma to control the flow of energy and particles toward the wall. In tokamaks, magnetic perturbations which cause magnetic chaos in the plasma edge can be used to prevent harmful instabilities called edge-localized modes [15, 16, 17].

1.2.4 The RFP dynamo and chaos

The RFP provides a good test case for studying transport in varying degrees of magnetic chaos. In standard RFP operations, magnetic chaos due to large tearing mode instabilities is the dominant transport mechanism [18, 19, 20, 21]. The tearing modes are driven unstable by current gradients that arise when the RFP is powered by a toroidal inductive electric field. The tearing modes exist at moderate amplitude as the current profile begins to steepen. At some point, the tearing modes become highly unstable, growing rapidly to much larger amplitude. During this event, called a 'sawtooth crash,' the interaction between tearing modes redistributes current to produce a shallower current profile [22]. This mechanism is referred to as the RFP dynamo, because it is responsible for generating the reversed toroidal magnetic field that would otherwise decay away due to plasma electrical resistance [23, 24]. After the sawtooth crash, the tearing modes fall rapidly back to a moderate amplitude. This 'sawtooth cycle' repeats itself many times throughout the duration of a standard MST discharge. During the crash, the magnetic field becomes extremely chaotic, resulting in rapid loss of heat from the plasma [21].

There are situations in which reduced chaos and improved confinement are possible in the RFP. It is possible to (transiently) suppress tearing modes by replacing the dynamo with inductive poloidal current drive in the plasma edge, resulting in much-improved thermal confinement [18, 25, 26, 27]. This technique is referred to as pulsed poloidal current drive (PPCD). The RFP may also exhibit spontaneous self-organization into an improved-confinement state. At high plasma current and low density, it is possible for a single tearing mode to grow very large (several percent of the background field) while simultaneously reducing the amplitude of all the other tearing modes. This quasi-single helicity (QSH) situation can restore good confinement while still providing the necessary RFP dynamo effect [6, 28].

1.2.5 Turbulence

Magnetic field line chaos is not the only mechanism that can enhance transport in a magnetized plasma. Electrostatic turbulence is another possible mechanism. Instabilities called drift waves can be driven by density or temperature gradients. Saturated drift wave turbulence causes transport across magnetic flux surfaces in the following way. In a magnetized plasma, electric fields applied perpendicular to the magnetic field cause a plasma flow $\mathbf{v}_E$ called the 'E cross B' drift velocity, given by $\mathbf{v}_E \propto \frac{\mathbf{E}\times\mathbf{B}}{B^2}$, where $\mathbf{E}$ is the electric field [29, p. 27]. The drift wave turbulence contains fluctuating electric fields and drift velocities that cause energy and particles to diffuse across magnetic flux surfaces due to correlations of the velocity with the density or pressure fluctuations. This is referred to as electrostatic transport due to the importance of the fluctuating electric field.

Drift wave turbulence is common in magnetized plasma experiments because most experiments produce strong gradients which drive the drift wave instabilities. In MST, electrostatic transport is the dominant transport mechanism in the plasma edge [30, 31]. Improved confinement RFP discharges may develop sufficiently large gradients to excite certain classes of drift waves [32]. Ion gyro-orbit scale turbulence has been well-characterized in DIII-D [33]. A recent review of experimental drift wave turbulence studies (with an accessible introduction to the theory and diagnostic techniques) is Ref. [34].

1.3 MST device

In MST, a toroidal magnetic field is produced by driving poloidal current in the aluminum vacuum vessel walls [2]. (Most most toroidal devices use a separate set of coils instead.) In the RFP, the weak, negatively-oriented toroidal field at the wall is produced externally, while

the large positive toroidal field in the core (up to 0.6 T) is due to poloidal currents flowing in the plasma itself, generated by the RFP dynamo. The relatively low applied toroidal field is one of the chief advantages of the RFP concept, because it reduces the size and cost of the external magnetic field coils compared to a similarly-sized tokamak [35]. The reversal parameter measures the ratio of the toroidal field at the plasma edge to the mean toroidal field over the plasma cross-section:

$$F \equiv \frac{B_\phi(r=a)}{\langle B_\phi \rangle}. \tag{1.3}$$

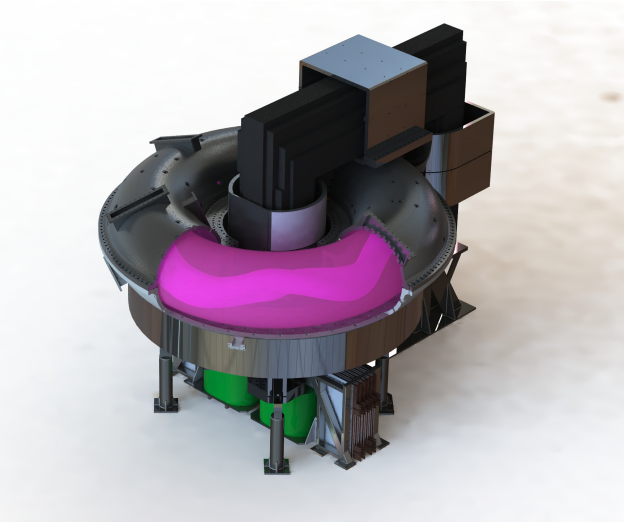

Figure 1.5: A CAD drawing of MST made by Steve Oliva featuring the 5-cm-thick aluminum vacuum vessel, iron core inductive transformer, and plasma (purple) with an internal helical structure.

The toroidal plasma current in MST is driven inductively by a large iron-core transformer that links the torus. (Most other devices use a solenoid placed upright in the center of the torus.) MST's plasma current I_p is limited to 0.6 MA, although this limit may be raised in the near future with the installation of a programmable power supply to drive the transformer

safely to higher current. The existing power supply is a large pulse-forming network that stores up to 2 megajoules of energy. The iron-core transformer is capable of a flux change of 2 webers when it is first reverse-biased to -1 weber. (One weber of flux provides one volt of inductive drive for one second.) MST inductive loop voltage peaks around 20 V, while discharges typically last 60 milliseconds. The plasma current is constant for period of about 20 ms.

The flux surfaces and q-profile for a standard MST discharge are shown in Figure 1.6. The core tearing modes have $m = 1$, $n = 5, 6, 7...$ due to the q-profile, which goes from $-q \approx 1/5$ in the core to $q = 0$ at the reversal surface (near $r/a = 0.75$). MST flux surfaces are circular. The plasma electron density is typically $n_e \approx 1 \times 10^{19}$ particles per cubic meter. In standard discharges, the electron temperature is up to 500 eV, although in improved-confinement discharges, temperatures up to 2 keV are possible. (One electron-volt is approximately 11,600 $C°$.)

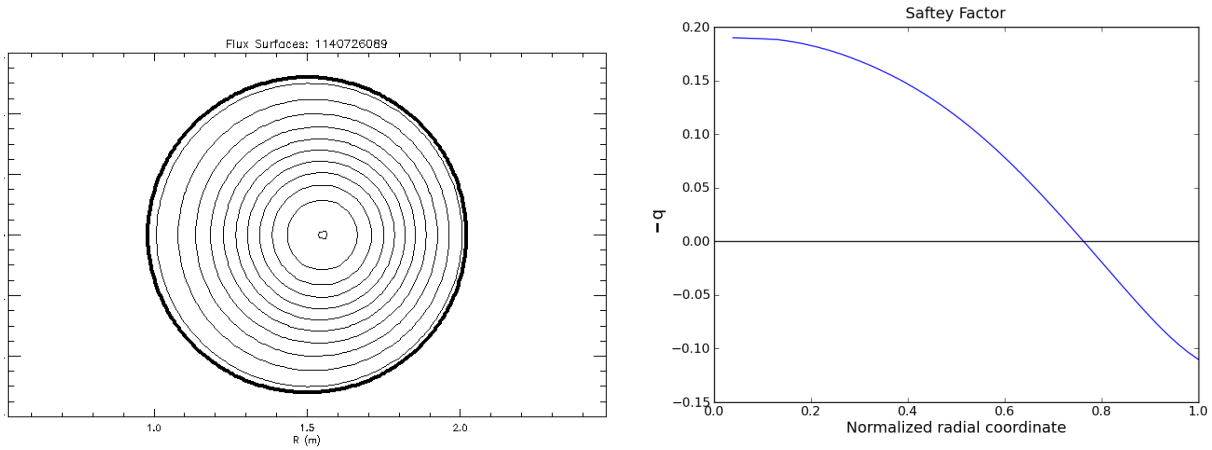

(a) **(b)**

Figure 1.6: (a)MST flux surfaces are circular, with a slight outward shift (the Shafranov shift) due to magnetic and plasma pressure. Plot produced by MSTFIT. (b) Typical q-profile in MST during a standard discharge. Using the coordinate system defined in this thesis (Chapter 8), q is negative in the core, so $-q$ is plotted here.

MST has a high-quality diagnostic suite. The Thomson scattering system (described in more detail in Section 2.1.2, Section 3.1.1, and Chapter 6) is the primary diagnostic used to gather data for this thesis. It measures electron temperature across the minor radius of MST with high temporal and spatial resolution. Another critical diagnostic for this work is the toroidal magnetic array, which yields the amplitude and phase of the tearing mode magnetic field at the plasma edge. Magnetic diagnosis is necessary for inferring the internal magnetic structure in MST for comparison with the temperature structures.

1.4 DIII-D device

DIII-D is a tokamak with major radius 1.67 m, and minor radius 0.67 meters. While these parameters are only a few percent larger than those of MST, the plasma volume is significantly larger because the poloidal cross-section of DIII-D is vertically elongated [3]. The flux surface shaping can be controlled by external coils, unlike MST where the flux surfaces remain circular. The flux surface shape used in the experiment described in this thesis is shown in Figure 1.7a.

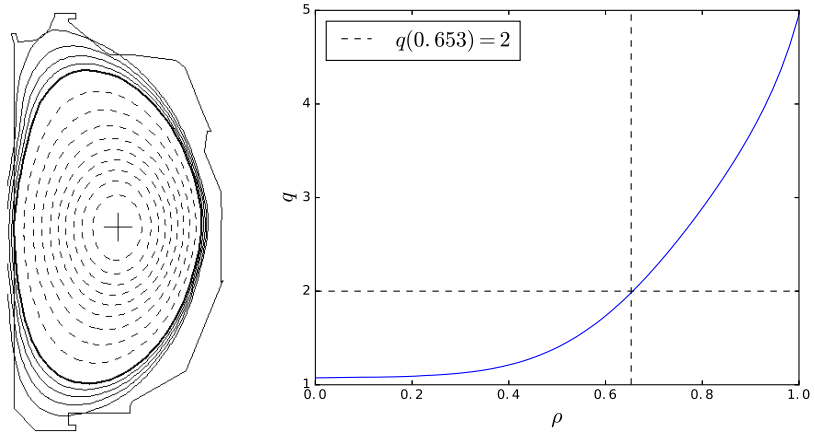

(a) **(b)**

Figure 1.7: (a) Flux surfaces of DIII-D in the configuration used during the experiment reported in this thesis. Plot produced using EFITVIEWER. The second 'D' in the name of the device refers to the characteristic shape of the flux surfaces. (b) The q-profile in DIII-D during the experiment described in this thesis. The horizontal axis is the normalized flux surface label ρ.

DIII-D's maximum current is about 3 MA, while the maximum field on axis is 2.2 T [3]. The DIII-D inductive current drive solenoid is capable of sustaining 10-second-long discharges while consuming 7.5 webers of flux. The q-profile in a tokamak is much higher than the q-profile in the reversed-field pinch, starting out around 1.0 in the core, and increasing outward. This causes the primary resonances to be $(m, n) = (m, 1)$ where $m = 1, 2, 3, ...$ Sometimes modes such as $(2, 3)$ are also observed. The q-profile from the DIII-D experiment is shown in Figure 1.7b.

Although many diagnostics were deployed for the DIII-D island turbulence experiment, the results presented in this thesis are from the beam emission spectroscopy (BES) diagnostic, which measures ion-gyro-orbit scale density fluctuations. Another important tool at the DIII-D facility is the external control coil system that was used to impose and rotate the $m = 2, n = 1$ magnetic island. Additional relevant details about DIII-D may be found in

Chapter 4.

1.5 Main results

The goal of this thesis is to relate improvements in understanding turbulence, chaos, and transport within large magnetic islands. The first three results directly contribute to this goal. The last two results, while somewhat tangential, are included for completeness.

(1) Electron temperature fluctuation harmonics indicate Ohmic heat confinement within overlapped magnetic islands in MST standard discharges. Chapter 2 focuses on results obtained from the Thomson scattering diagnostic at high repetition rate (25 kHz) with pulse trains of 8 pulses. The short pulse trains, and proximity of the sampling rate to the oscillation frequency of the tearing modes, necessitate statistical methods and large ensembles of data to extract temperature fluctuations correlated with the tearing mode magnetic fields. The information contained in the fluctuations suggests that the core-most resonant tearing mode $(m, n = 1, 6)$ island confines Ohmic heat deposited inside it, resulting in elevated internal temperature. However, the temperature fluctuations also indicate that adjacent magnetic islands overlap significantly, breaking the island flux surfaces and resulting in magnetic chaos. Magnetic chaos is generally associated with poor thermal confinement, making the observation of hot islands somewhat paradoxical.

(2) Thermal transport in a large hot island-like structures in an RFP may be consistent with magnetic chaos. Chapter 3 resolves the paradox by presenting evidence that chaotic magnetic structures can indeed confine Ohmic heating well enough to create a measurably peaked temperature structure. The new high-repetition-rate 'Fast Laser' for

Thomson scattering captured a two-dimensional image of a rotating hot island structure, the first such measurement in an RFP device. Magnetic modeling shows that the shape, size, and location of the $n = 6$ magnetic island match those of the temperature structure. However, incorporating the adjacent $n = 7$ magnetic island in the magnetic field modeling destroys almost all the flux surfaces within the $n = 6$ island, resulting in a chaotic magnetic field with residual structure. Transport modeling based on field line tracing yields an estimate of $\chi_{e,m} \approx 30\,\mathrm{m}^2/\mathrm{s}$ for the effective perpendicular electron thermal conductivity within the magnetic structure. This is within the range $\chi_{e,th} \approx 10\,\mathrm{to}\,40\,\mathrm{m}^2/\mathrm{s}$ for the thermal conductivity estimated from Ohmic power density and the observed temperature gradient.

(3) Large magnetic islands in DIII-D strongly modulate electron density turbulence in two dimensions. In Chapter 4, preliminary results are presented from an experiment on turbulence in and around a large, externally-imposed magnetic island in DIII-D. External control coils trigger the formation of the island and rotate it past the various turbulence diagnostics. The beam emission spectroscopy (BES) diagnostic measures density turbulence on the ion-gyroradius scale. A high-resolution two-dimensional picture of the turbulence intensity reveals strong suppression of turbulence within the island, and enhancement near the island X-point, relative to the turbulence without an island. This confirms expectations that gradient flattening at the O-point would reduce turbulence there. The island is sufficiently wide that turbulence spreading does not maintain significant turbulence inside the island. When the plasma rotation is too high, a large island does not form, even though the control coils still apply the same magnetic field perturbation. In this case, turbulence is still modified by the applied field, but in a less pronounced way.

(4) High-current improved-confinement discharges in MST do not reach thermal transport equilibrium. An explanation of the temperature profile dynamics in improved-confinement discharges in MST is put forward in Chapter 5. This result, which is only tangentially related to the focus of this thesis, is presented primarily for archival purposes. The application of a poloidal inductive electric field is known to rapidly suppress tearing mode amplitudes, chaos, and transport, leading to rapidly climbing core electron temperature. The rate of rise of the temperature is consistent with the entire Ohmic heating power being absorbed by the electrons, with transport playing a negligible role in the core thermal energy balance. This could explain the fact that Thomson scattering does not detect island temperature structures in improved-confinement discharges, even though islands are probably still present. It also suggests that the ultimate limits on confinement in the RFP have not yet been encountered, because the transient inductive current drive does not yet last long enough for the temperature to equilibrate (at least in high-current discharges). In one discharge studied, where the temperature does reach a stagnation point, the culprit is a resurgence of tearing mode activity just prior to the end of the inductive current drive.

(5) Improved Thomson scattering calibrations will enable better understanding of the $n = 5$ magnetic mode in MST. Attempts to elucidate the magnetic structure of the $n = 5$ magnetic mode in MST using Thomson scattering measurements have so far been unfruitful. It is shown in Chapter 2 that Thomson scattering calibration uncertainties are large enough to obscure the small mean temperature gradients that must be determined in order to infer the magnetic field structure from the $n = 5$ temperature fluctuations. This issue has been addressed in Chapter 6, where improvements made to the Thomson scattering calibration procedures are discussed. The improved calibrations should enable future efforts to understand the $n = 5$ mode by resolving small temperature gradients in the core.

References

[1] E. T. Jaynes, *Probability Theory: The Logic of Science*, edited by G. L. Bretthorst (Cambridge University Press, 2003).

[2] R. N. Dexter, D. W. Kerst, T. W. Lovell, S. C. Prager, and J. C. Sprott, Fusion Technology **19**, 131 (1991).

[3] J. Luxon, Nuclear Fusion **42**, 614 (2002).

[4] R. König, P. Grigull, K. McCormick, Y. Feng, J. Kisslinger, A. Komori, S. Masuzaki, K. Matsuoka, T. Obiki, N. Ohyabu, H. Renner, F. Sardei, F. Wagner, and A. Werner, Plasma Physics and Controlled Fusion **44**, 2365 (2002).

[5] M. W. Jakubowski, O. Schmitz, S. S. Abdullaev, S. Brezinsek, K. H. Finken, A. Krämer-Flecken, M. Lehnen, U. Samm, K. H. Spatschek, B. Unterberg, R. C. Wolf, and the TEXTOR team, Physical Review Letters **96**, 035004 (2006).

[6] P. Martin, L. Marrelli, A. Alfier, F. Bonomo, D. F. Escande, P. Franz, L. Frassinetti, M. Gobbin, R. Pasqualotto, P. Piovesan, D. Terranova, and the RFX-mod team, Plasma Physics and Controlled Fusion **49**, A177 (2007).

[7] L. Bardóczi, T. L. Rhodes, T. A. Carter, N. A. Crocker, W. A. Peebles, and B. A. Grierson, Physics of Plasmas **23**, 052507 (2016).

[8] F. A. G. Volpe, M. E. Austin, R. J. La Haye, J. Lohr, R. Prater, E. J. Strait, and A. S. Welander, Physics of Plasmas **16**, 102502 (2009).

[9] A. H. Boozer, Reviews of Modern Physics **76**, 1071 (2005).

[10] M. Keilhacker, A. Gibson, C. Gormezano, P. J. Lomas, P. R. Thomas, M. L. Watkins, P. Andrew, B. Balet, D. Borba, C. D. Challis, I. Coffey, G. A. Cottrell, H. P. L. De

Esch, N. Deliyanakis, A. Fasoli, C. W. Gowers, H. Y. Guo, G. T. A. Huysmans, T. T. C. Jones, W. Kerner, R. W. T. König, M. J. Loughlin, A. Maas, F. B. Marcus, M. F. F. Nave, F. G. Rimini, G. J. Sadler, S. E. Sharapov, G. Sips, P. Smeulders, F. X. Söldner, A. Taroni, B. J. D. Tubbing, M. G. von Hellermann, D. J. Ward, and the JET team, Nuclear Fusion **39**, 209 (1999).

[11] "www.iter.org," .

[12] H. A. B. Bodin and A. A. Newton, Nuclear Fusion **20**, 1255 (1980).

[13] S. Matsuda and M. Yoshikawa, Japanese Journal of Applied Physics **14**, 87 (1975).

[14] P. Ghendrih, A. Grosman, and H. Capes, Plasma Physics and Controlled Fusion **38**, 1653.

[15] T. E. Evans, R. A. Moyer, P. R. Thomas, J. G. Watkins, T. H. Osborne, J. A. Boedo, E. J. Doyle, M. E. Fenstermacher, K. H. Finken, R. J. Groebner, M. Groth, J. H. Harris, R. J. La Haye, C. J. Lasnier, S. Masuzaki, N. Ohyabu, D. G. Pretty, T. L. Rhodes, H. Reimerdes, D. L. Rudakov, M. J. Schaffer, G. Wang, and L. Zeng, Phys. Rev. Lett. **92**, 235003 (2004).

[16] T. E. Evans, Plasma Physics and Controlled Fusion **57**, 123001 (2015).

[17] T. E. Evans, M. E. Fenstermacher, R. A. Moyer, T. H. Osborne, J. G. Watkins, P. Gohil, I. Joseph, M. J. Schaffer, L. R. Baylor, M. Becoulet, J. A. Boedo, K. H. Burrell, J. S. Degrassie, K. H. Finken, T. Jernigan, M. W. Jakubowski, C. J. Lasnier, M. Lelmen, A. W. Leonard, J. Lonnroth, E. Nardon, V. Parail, O. Schmitz, B. Unterberg, and W. P. West, Nuclear Fusion **48**, 024002 (2008).

[18] J. S. Sarff, S. A. Hokin, H. Ji, S. C. Prager, and C. R. Sovinec, Phys. Rev. Lett. **72**, 3670 (1994).

[19] S. C. Prager, Plasma Physics and Controlled Fusion **41**, A129 (1999).

[20] T. M. Biewer, C. B. Forest, J. K. Anderson, G. Fiksel, B. Hudson, S. C. Prager, J. S. Sarff, J. C. Wright, D. L. Brower, W. X. Ding, and S. D. Terry, Physical Review Letters **91**, 045004 (2003).

[21] J. A. Reusch, J. K. Anderson, D. J. Den Hartog, F. Ebrahimi, D. D. Schnack, H. D. Stephens, and C. B. Forest, Physical Review Letters **107**, 155002 (2011).

[22] S. D. Terry, D. L. Brower, W. X. Ding, J. K. Anderson, T. M. Biewer, B. E. Chapman, D. Craig, C. B. Forest, R. O'Connell, S. C. Prager, and J. S. Sarff, Physics of Plasmas **11**, 1079 (2004).

[23] E. Caramana and D. Baker, Nuclear Fusion **24**, 423 (1984).

[24] R. G. Watt and R. A. Nebel, Physics of Fluids **26**, 1168 (1983).

[25] J. K. Anderson, J. Adney, A. Almagri, A. Blair, D. L. Brower, M. Cengher, B. E. Chapman, S. Choi, D. Craig, D. R. Demers, D. J. Den Hartog, B. Deng, W. X. Ding, F. Ebrahimi, D. Ennis, G. Fiksel, C. B. Forest, P. Franz, J. Goetz, R. W. Harvey, D. Holly, G. T. A. Huijsmans, M. Kaufman, T. Lovell, L. Marrelli, P. Martin, K. McCollam, V. V. Mirnov, P. Nonn, R. O'Connell, S. Oliva, P. Piovesan, S. C. Prager, I. Predebon, J. S. Sarff, G. Spizzo, V. Svidzinski, M. Thomas, and M. D. Wyman, Physics of Plasmas **12**, 056118 (2005).

[26] B. E. Chapman, J. K. Anderson, T. M. Biewer, D. L. Brower, S. Castillo, P. K. Chattopadhyay, C.-S. Chiang, D. Craig, D. J. Den Hartog, G. Fiksel, P. W. Fontana, C. B. Forest, S. Gerhardt, A. K. Hansen, D. Holly, Y. Jiang, N. E. Lanier, S. C. Prager, J. C. Reardon, and J. S. Sarff, Physical Review Letters **87**, 205001 (2001).

[27] B. E. Chapman, A. F. Almagri, J. K. Anderson, D. L. Brower, K. J. Caspary, D. J. Clayton, D. Craig, D. J. Den Hartog, W. X. Ding, D. A. Ennis, G. Fiksel, S. Gangadhara,

S. Kumar, R. M. Magee, R. O'Connell, E. Parke, S. C. Prager, J. A. Reusch, J. S. Sarff, H. D. Stephens, and Y. M. Yang, Plasma Physics and Controlled Fusion **52**, 124048 (2010).

[28] D. F. Escande, P. Martin, S. Ortolani, A. Buffa, P. Franz, L. Marrelli, E. Martines, G. Spizzo, S. Cappello, A. Murari, R. Pasqualotto, and P. Zanca, Physical Review Letters **85**, 1662 (2000).

[29] D. A. Gurnett and A. Bhattacharjee, *Introduction to Plasma Physics* (Cambridge University Press, 2005).

[30] T. D. Rempel, C. W. Spragins, S. Prager, S. Assadi, D. J. Den Hartog, and S. Hokin, Physical Review Letters **67**, 1438 (1991).

[31] J. Lei, P. M. Schoch, D. R. Demers, U. Shah, K. A. Connor, J. K. Anderson, and T. P. Crowley, Physical Review Letters **89**, 275001 (2002).

[32] D. Carmody, M. J. Pueschel, J. K. Anderson, and P. W. Terry, Physics of Plasmas **22**, 012504 (2015).

[33] M. W. Shafer, R. J. Fonck, G. R. McKee, C. Holland, A. E. White, and D. J. Schlossberg, Physics of Plasmas **19**, 032504 (2012).

[34] G. R. Tynan, A. Fujisawa, and G. McKee, Plasma Physics and Controlled Fusion **51**, 113001 (2009).

[35] F. Najmabadi, R. W. Conn, R. A. Krakowski, K. R. Shultz, and D. Steiner, *The TITAN Reversed-field-pinch fusion reactor study: final report, vol. I*, Tech. Rep. (1990).

2 Thomson Scattering Electron Temperature Fluctuation Analysis

Those who ignore Statistics are condemned to reinvent it.

— attributed to Brad Efron [1]

This chapter presents studies of tearing modes in MST using electron temperature fluctuations measured with the Thomson scattering system. In Section 2.1, the Thomson scattering diagnostic is introduced, with emphasis on the capabilities which enable tearing mode studies. Section 2.2 introduces the statistical techniques developed previously at MST for the statistical fluctuation analysis, along with the basic model relating the island structure to the temperature fluctuations. In Section 2.3, these techniques are extended, resulting in new observations. In particular, investigation of the higher-harmonic content of the fluctuations provides strong evidence that the symmetric, isothermal island model is not adequate to describe the $n = 6$ mode's temperature structure (Section 2.3.1). It is also shown in Section 2.3.2 that extension of the isothermal model to asymmetric islands is also not sufficient to produce the observed harmonic content. This leads toward the conclusion, confirmed in the following chapter, that the $n = 6$ mode fluctuations reflect a heat-confining island. Finally, novel autocorrelation measurements demonstrate that the majority of the electron temperature fluctuation variance is attributable to the tearing modes, and that plasmas with tearing

mode suppression or lack of mode rotation do not show appreciable temperature fluctuations (Section 2.3.3).

2.1 MST Thomson scattering diagnostic

The TS System at MST is a highly capable diagnostic, providing both equilibrium and fluctuation measurements of electron temperature with low uncertainty. This overview of the system also highlights some of the challenges faced in achieving good TS measurements. The use of a high-repetition-rate laser to enable (effectively) 2D measurements of rotating tearing modes via their perturbations of the electron temperature was first proposed for MST by Den Hartog in 2003 [2]. This vision has been realized in full with the development of the Fast Thomson Laser [3, 4]. In this chapter, the focus is on what can be learned from the measurements made with the Spectron lasers, which are the precursor to the Fast Laser, and are still the workhorse laser system for the MST TS diagnostic. The results from the Fast Laser are presented in the next chapter.

2.1.1 Principles and practice of Thomson scattering diagnostic

Non-collective Thomson scattering is a nearly ideal way to measure the temperature and density of the electrons in a plasma. Thomson scattering is a particular case of the more general Compton scattering, which describes the interaction of a photon (or electromagnetic wave) with a charged particle. Thomson scattering is simply the limit in which the photon energy is much less than the mass-energy of the charged particle, so that the scattering is nearly elastic. Non-collective Thomson scattering occurs when the incident wavelength is much smaller than the Debye length, so that only the motion of individual electrons

contributes, while collective motion (which is sensitive to the motion of ions through Debye screening) is canceled out [5].

If the plasma electrons are in thermal equilibrium, the velocity distribution of electrons will be a simple Maxwellian distribution. The second moment of the distribution function is related to the temperature, the first to the mean flow velocity, and the zeroth to the density. If a mono-energetic photon beam (typically a laser) is injected into the plasma, the scattered photons will carry the imprint of this distribution via a Doppler shift, resulting in a distribution of received wavelengths. Measuring the spectrum of the scattered light yields the density and temperature. Temperatures are typically quoted in energy units as electron-Volts (eV), and densities in particles per cubic meter or centimeter.

Interpretation of the measurements is very direct, and when calibrated the systematic errors can be small. Thomson scattering can also be used in so-called overdense plasmas, where the electron plasma frequency exceeds the cyclotron frequency, which prevents electron-cyclotron emission diagnostics (which also measure electron temperature) from operating. This is applies for MST and other reversed field pinches, which are inherently overdense. Unlike probes, Thomson scattering does not perturb the plasma, and is capable of operating in very hot plasmas. Intersection of the laser beam with the viewing line-of-sight of the collection system localizes the measurement (unlike soft x-ray (SXR) emission diagnostics of electron density and temperature which receive signal from the entire line-of-sight). The primary shortcoming of Thomson scattering diagnostics is the small scattering cross-section, which necessitates high power pulsed lasers to achieve good signal-to-noise ratio. Unlike emission diagnostics or interferometry, which can operate continuously, Thomson scattering is limited to the repetition rate of the pulsed laser system.

2.1.2 MST Thomson Scattering Diagnostic System

Figure 2.1a shows the layout of the TS system on MST. The bulk of the TS equipment is located in a separate room, across a public hallway from the MST machine area. The laser beams are passed underneath the hallway and into MST. Fiber optics return the scattered light to the TS clean room, where the polychromators decompose the scattered spectrum onto detectors. Digitizers then store the signals on a server for processing.

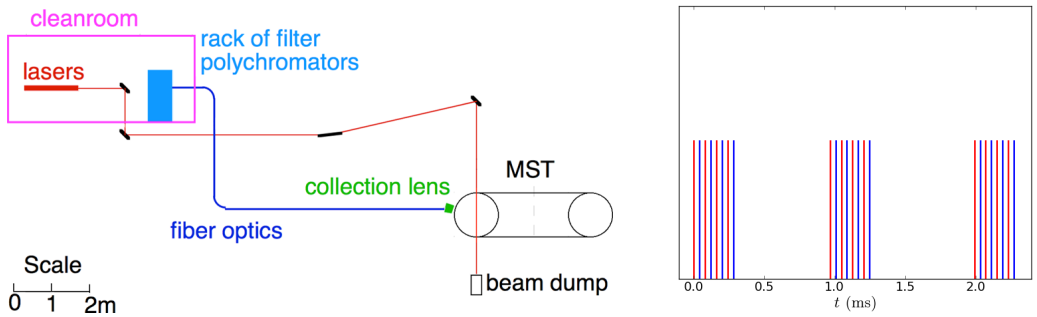

Figure 2.1: (a) Diagram of the TS system layout. (b) Laser pulses produced in two bursts by the Spectron laser system.

The MST TS system is distinguished by its flexible high-power repetitively-pulsed laser systems. Two laser systems are now in routine use, with many commonalities. The older system is a pair of commercial Spectron SL858g lasers, while the new system (the Fast Laser) is custom-built [4, 6, 7]. Both systems operate at 1064 nm using Nd-doped glass or YAG crystal rods, and achieve up to 2 Joules of laser energy per pulse, as required for adequate signal-to-noise ratio. The pulse widths are about 20 nanoseconds. The lasers fire in burst mode, providing one or several bursts during an MST discharge. Each burst is composed of multiple laser pulses. The length of a burst is limited by hardware constraints on the amount of energy which the laser can deliver at a given pulse repetition rate and pulse energy.

The Spectron laser pair can produce a single long burst of 30 pulses at 1-2 kHz, which covers 15-30 ms, approximately the length of the current flat-top in MST plasmas. The Spectrons can also produce bursts of 8 pulses at 25 kHz; 3 such bursts can be produced during one MST discharge (Figure 2.1b). In these modes, each laser is operating at half the nominal frequency, and the two lasers are staggered such that every other pulse comes from a different laser. However, the timing between the two lasers can be shifted, so that two pulses (one from each laser) arrive within an arbitrarily short time. This mode can be used to probe higher-frequency phenomenon, as will be discussed in Section 2.3.3. The Fast Laser has demonstrated the capability to operate up to 125 kHz for single bursts with 63 pulses. The maximum achieved repetition rate for a burst was 333 kHz for 8 pulses. More detail about the Fast Laser performance can be found in [4].

The laser beams exit the laser with diameter ≈1 cm, and are collimated. The two beams from the Spectron lasers are injected parallel but offset to each other onto the first mirror in the beamline. In order to inject the Fast Laser beam, one mirror must be translated out of the beam path. There are five mirrors in the common beamline, along with a focusing lens located after the final turning mirror above the MST vessel, which minimizes the beam diameter in the scattering region. The scattered light is collected by a large retractable 7-element lens system, illustrated in Figure 2.2. The lens images the laser beam onto a curved surface outside the vessel, where an array of fiber optic bundles collects the light [8]. The intersection of the fiber bundle line-of-sight with the laser beam path fixes the measurement location. There are 21 optical fibers, but 34 possible fiber locations, leaving some flexibility (for example, concentrating on edge or core phenomena). Positions of the measurement points along the beamline are denoted z, with $z = 0$ at the center of the plasma, and $z = a$ at the bottom of the vessel.

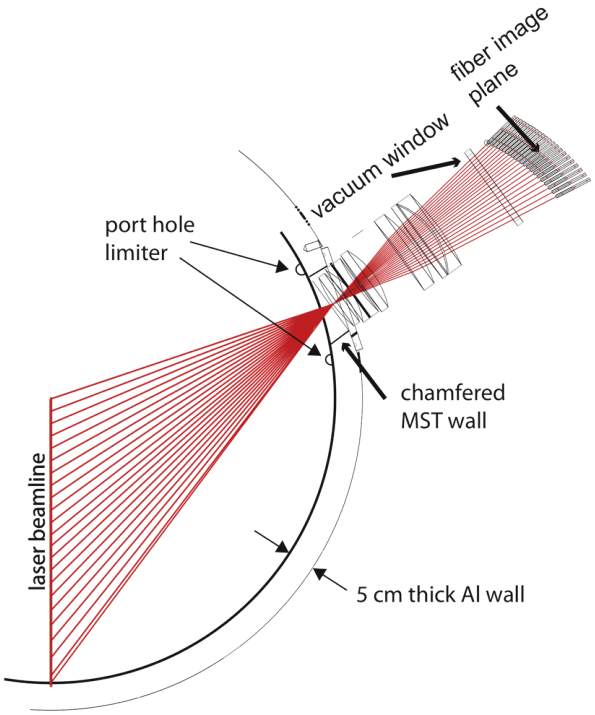

Figure 2.2: MST Thomson Scattering geometry, showing laser beam path through MST vacuum vessel and location of collection optics and fiber bundles.

2.2 Temperature fluctuation analysis overview

Previous studies of tearing mode temperature fluctuations on MST have successfully used Bayesian statistical analysis to detect the existence of tearing mode islands and to infer properties of the magnetic structure. Stephens [9, 10] developed this technique and was able to observe fluctuations associated with both $n = 5, 6$ tearing modes in standard plasmas. The $n = 6$ fluctuations (at the fundamental frequency) were interpreted in terms of the symmetric, isothermal island model. The island width and the location of the rational surface were inferred and were compared to expectations from models of the magnetic fields. The $n = 7, 8$ modes were also investigated and appear similar to the $n = 6$ results, although

with smaller amplitude and hence lower signal-to-noise. Overlap of the radial extent of the $n = 6, 7$ fluctuations was noted, with the suggestion that remnant islands might be responsible for producing these fluctuations. The $n = 5$ fluctuations had a different character, showing no phase inversion surface, and hinting that the $n = 5$ mode was a heat-confining structure rather than an isothermal one. A simple model was used to estimate the degree of confinement within the $n = 5$ structure, with $\chi_e = 30\,\mathrm{m}^2/\mathrm{s}$ estimated. Comparisons were also made with Poincare plots from MAL to trace the magnetic field from DEBS simulations of MST, which showed the existence of remnant islands within the chaotic magnetic field.

Kasten [11, 12] investigated fluctuations correlated with the $m = 0, n = 1$ mode which is resonant at the reversal surface. Evidence was found that in some situations, this mode could have a heat-confining island or an isothermal island.

Parke [13] took the analysis of the core tearing modes a step further. Using the Bayesian technique, the rational surface location and island width were calculated from the fluctuation profiles using the isothermal model of Ref. [14]. This allowed the rational surface locations for the $n = 6, 7, 8$ modes (with uncertainties) to be used as constraints on the MSTFit reconstruction process. Suppression of the tearing modes by current profile modification due to injection of a neutral beam was also observed. Additionally, the phase shift introduced by the Shafranov shift was accounted for, which led to studies of the fluctuation-driven dynamo (current transport). An illustration of the observed fluctuations and the application of the fitting model developed by Parke is shown in Figure 2.3.

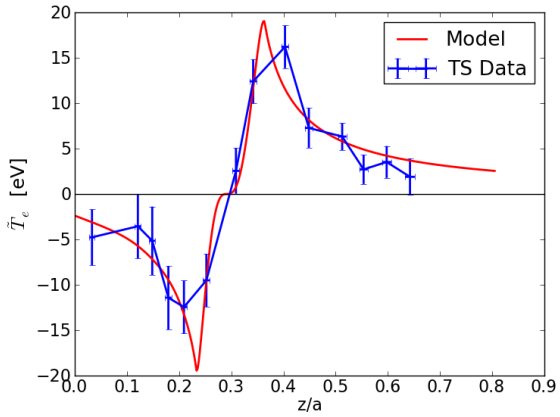

Figure 2.3: Fitting to MST temperature fluctuation profile using the isothermal island model implemented by Parke [13], allowing the island width and rational surface location to be inferred.

2.2.1 Symmetric, isothermal island model

This section provides a general overview of the analytic model developed by Fitzpatrick [15] for the fluctuations expected from an isothermal symmetric island. The island shape is defined by the contours of the island flux function Ω (Figure 2.4). In the special case that the island is so narrow that the curvature of the rational surface is negligible (the 'slab approximation'), and so are other higher-order derivatives of the magnetic field (the 'constant-ψ' approximation), the island flux function is:

$$\Omega = 8\frac{x^2}{W^2} + \cos\zeta. \tag{2.1}$$

Here $\zeta \equiv m\theta - n\phi$ is the helical phase angle of the tearing mode; W is the width of the island; $x = r - r_s$ is the distance from the rational surface. Ω goes from -1 at the O-point ($x = 0, \zeta = \pi$) to 1 at the separatrix (X-points at $x = 0, \zeta = 0, 2\pi$).

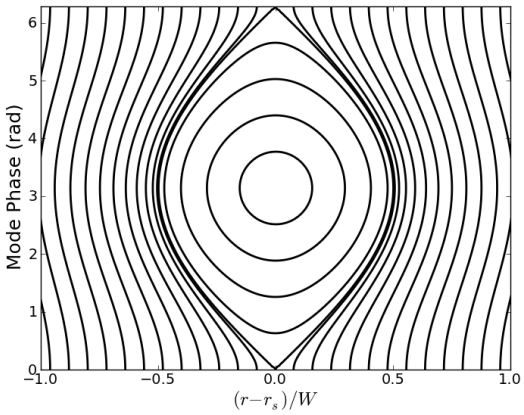

Figure 2.4: Contours of flux Ω in the symmetric island model.

First it is necessary to solve the heat conduction problem across these flux surfaces. The amount of heating taking place in the island is assumed to be small ($\nabla \cdot \mathbf{q} \approx 0$), compared to the heat flux $\mathbf{q}$ flowing through the rational surface from the interior of the plasma toward the edge. Steady-state temperature is assumed to have been reached ($\frac{dT}{dt} = 0$). The heat flux is assumed to be due to conduction, with conduction coefficients $\kappa_{\|} \gg \kappa_{\perp}$for the heat conduction parallel and perpendicular to the magnetic field, respectively. Thus, the thermal energy equations read:

$$\begin{aligned} \mathbf{q} &= \kappa_{\|}\nabla_{\|}T + \kappa_{\perp}\nabla_{\perp}T \\ \nabla \cdot \mathbf{q} &= 0 \end{aligned} \tag{2.2}$$

Fitzpatrick's calculation is done in terms of differentials and requires multiple coordinate transforms. With the assumption of strong parallel conductivity, the temperature becomes constant on flux surfaces, which simplifies the problem conceptually. Ren *et al* [14] show how to do a volume integral to find the heat flux through the (toroidal) flux surfaces outside

the island. Since the heat source in the region is assumed to be zero, the radial heat flux (integrated over a flux surface) is constant over radius. Since the temperature is purely a function of flux, the perpendicular temperature gradient can be written as $\frac{dT}{d\Omega}\nabla\Omega$.

$$\frac{dT}{d\Omega}\int |\nabla\Omega| dl \propto \int \mathbf{q}\cdot d\mathbf{A} = const. \tag{2.3}$$

The area integral in the center of Equation 2.3 would need to be taken over a flux surface, but by symmetry it can be reduced to a line integral (in the left-hand side of Equation 2.3) around the perimeter of a flux surface in a plane that cuts through the flux surface. Once the integral (which is determined purely by the flux surface geometry) is solved, the temperature is determined as a function of the flux using the mean temperature and the mean temperature gradient as boundary conditions. Then one can Fourier transform in ζ to get the harmonics of the temperature fluctuation: $T_\nu(x,\zeta) = \sum_{\nu=1}^{\infty} T_\nu(x)\cos\nu\zeta$. The result is not closed-form, and must be evaluated numerically.

However, the form of the fundamental harmonic ($\nu = 1$) fluctuation can be understood qualitatively, based on the following asymptotes derived by Fitzpatrick [15]. For $x > W$, the fluctuation is basically due to the displacement of the flux surfaces, which are to a good approximation surfaces of constant temperature. The perturbation of the flux surfaces due to the island (and hence the fluctuation amplitude) falls off with distance from the rational surface as

$$T_{\nu=1}(x) \approx \frac{W^2 T_s'}{16x} \propto x^{-1} \tag{2.4}$$

where T_s' is the mean temperature gradient. For $x < W$, the fluctuation is basically due to jumping between the temperature inside the island and the temperature outside the island.

This results in the scaling

$$T_{\nu=1}(x) \approx \frac{8WT_s'}{3}(\frac{x}{W})^3 \propto x^3. \tag{2.5}$$

The fluctuation goes to zero at the rational surface because the rational surface lies entirely inside the island, where the temperature is constant. Increasing distance results in increasing fluctuations, up to the peak amplitude which occurs at $x = W/2$. Note that both of these functions are odd: the fluctuation changes sign across the rational surface. The numerical solution for the first three harmonics along with the asymptotes are illustrated in Figure 2.5.

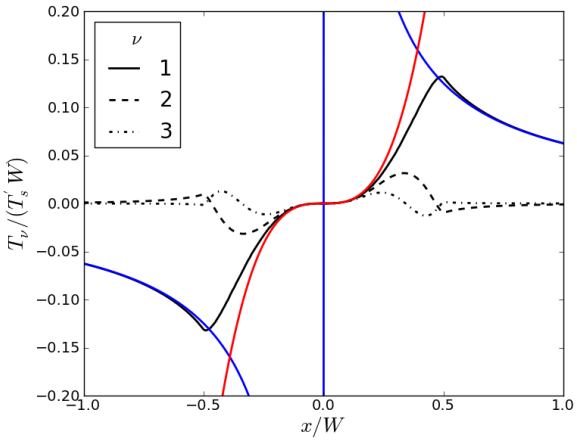

Figure 2.5: Temperature fluctuation harmonic profiles for the symmetric, isothermal island model derived by Fitzpatrick [15]. The red and blue curves are the asymptotes for the fundamental ($\nu = 1$) for small and large x. Note that all harmonics are zero at the rational surface. The higher harmonics are much smaller than the fundamental, and do not extend significantly outside the island width.

2.2.2 Bayesian analysis

The goal of the statistical analysis is to detect these temperature fluctuations with the Thomson scattering diagnostic if possible. However, as mentioned, this is difficult to do when using the Spectron lasers. First, there are only 8 pulses in each burst. Second, the fluctuations are at most 5-10% of the mean temperature, which is comparable with the

statistical uncertainty of an individual measurement. Third, the rotation rate of the plasma in the toroidal direction is ~ 25-50 km/s, which means that the fundamental frequency is 10-20 kHz. This is close to the repetition rate of the laser (25 kHz). Thus, the Nyquist frequency of the measurement is at or below the frequency of interest.

A simple way to inspect the temperature data for the presence of fluctuations correlated to the magnetic mode phase is to make a scatter plot of the temperature measurements against the phase of the mode when the measurement was made. However, any potential trends may be smeared out by the shot-to-shot variation of the mean temperature. Instead, one can plot $\Delta T_e[i] = T_e[i] - \frac{1}{8}\Sigma_{i=1}^{8} T_e[i]$ which is the deviation of each temperature in a burst from the mean temperature of that burst. Of course, since 8 points is not a large enough sample to pin down the mean temperature precisely, this method introduces some error that is not present in the Bayesian calculation outlined below. It does, however, produce an illustrative result.

Figure 2.6 demonstrates a temperature fluctuation correlated to the phase of a given mode ($n = 5$). This technique allows one to look for effects that might not be detected by the Bayesian model (such as outliers). The plot confirms the cosine dependence of the temperature on the mode phase, and even suggests a higher harmonic component $\cos(2\zeta_{n=5})$ due to the sharpness of the peak around $\zeta_{n=5} = 0$.

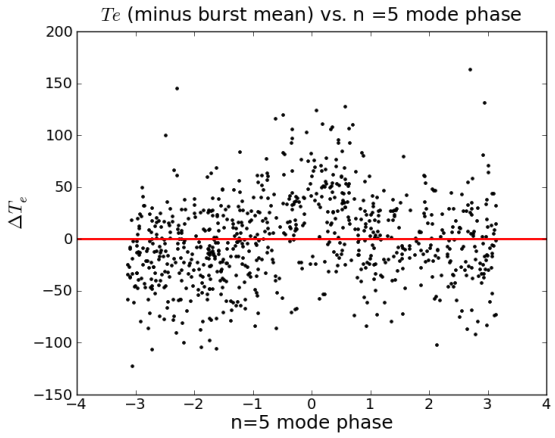

Figure 2.6: Scatter plot of the temperature deviation from the burst mean (ΔT_e) versus the $n = 5$ magnetic mode phase $\zeta_{n=5}$, at $z/a = 0.2$ for a large ensemble of burst measurements. The cosine-dependence of the temperature on the mode phase is clearly visible despite the noise.

In order to extract the maximum possible information from the measurements, a Bayesian statistical process is used in which a model of the fluctuations is fitted to the observed data to infer values for the model parameters. The knowledge of the phase of the tearing mode from the magnetic array allows to overcome the Nyquist limit. The model for the electron temperature is

$$T_{model}(z,t,b) = T_0(z,b) + \tilde{T}(r)\cos(\zeta(t,b) + \delta(z)) \tag{2.6}$$

where b identifies the burst, t is the time during the burst, ζ is the phase of the tearing mode at the Thomson scattering location, δ is the phase shift of the temperature fluctuation with respect to the magnetic mode phase, $\tilde{T}$ is the fluctuation amplitude, and T_0 is the mean temperature profile for each shot. Note that the temperature fluctuation amplitude and phase are assumed constant over the set of bursts in the ensemble.

The first step in the analysis is to write down the probability for having obtained the data

given the temperature predicted by the model. This is called the likelihood function:

$$\begin{aligned} P(T_{meas}(z,b)|T_{model}(z,b)) &= \frac{1}{\prod_i^N \sigma_i \sqrt{(2\pi)^N}} \exp\left(-\frac{1}{2}\chi^2\right) \\ \chi^2(z,b) &= \sum_i^N \left(\frac{T_{meas}(z,t_i,b) - T_{model}(z,t_i,b)}{\sigma_i}\right)^2 \end{aligned} \tag{2.7}$$

Here N is the number of measurements (laser pulses) in the burst. This model assumes there is no systematic error. There are finite random errors with standard deviations σ that are independent, but not necessarily identical. The σ are supplied along with the measured temperature values by the code that fits the raw spectral data (for more information, see Chapter 6). This equation defines how likely the observed measurements were, given knowledge of the mode phase, particular values of the model parameters, and the uncertainties in the measurement. If the difference between the modeled temperature and the measured temperature is large compared to the expected error of the measurement, then it is unlikely that the model parameters values are correct. This provides information about the parameters.

Bayes' Theorem is a way to formally calculate the probability of the parameter values given the data and model:

$$P(M|D,I) = \frac{P(D|M,I)P(M|I)}{P(D|I)} \tag{2.8}$$

Here $M = \{\tilde{T}, T_0, \delta\}$ is the set of model parameters, and $D = \{T_{meas}\}$ is the observed data, and I represents any other assumptions or information used (such as the mode phase ζ). This equation gives the probability of the model parameter values $P(M|D,I)$, called the

posterior distribution, in terms of three other functions: the likelihood (discussed above), the evidence, and the prior distribution. The distribution $P(D|I)$ is called the evidence. Once the data, the model, and the error distribution are specified, the evidence becomes simply a constant normalization factor. It is obtained by integrating the numerator over the model parameters M, a process called marginalization:

$$P(D|I) \equiv \int P(D|M,I)P(M|I)dM \tag{2.9}$$

$$= \int P(D,M|I)dM \tag{2.10}$$

The final term is called the prior distribution: $P(M|I)$. This distribution must encode a probability for the model parameters prior to having done the experiment. One must be careful to construct the prior distribution so that it does not introduce unintended bias in the results. Classical statistics (as opposed to Bayesian) simply stops with the likelihood, rather than going on to produce the posterior distribution. The Bayesian approach has the advantage of being explicit about how prior information may be incorporated, which can be useful [16].

Another benefit of the Bayesian approach is the marginalization of nuisance parameters. In the fluctuation model, equilibrium temperature is a nuisance parameter. Rather than carrying the mean temperature of each burst as a separate parameter through the entire calculation, the equilibrium can be marginalized out of the posterior distribution of each burst. The result is a probability distribution for $\tilde{T}, \delta$ encoding the information obtained from a particular burst:

$$P(\tilde{T},\delta|T_{meas}(z,b),\zeta(z,b)) = \int dT_0 P(T_0(z,b),\tilde{T}(z),\delta(z)|T_{meas}(z,b),\zeta(z,b)) \tag{2.11}$$

One may take Bayes' theorem iteratively. If conducting a series of experiments, the posterior distribution after the first experiment can be considered as the prior distribution before the next experiment [17]. Assuming the outcomes are independent:

$$P(M|D_b, D_{b-1,}..., D_1, I) \quad = \quad \Pi_b P(M|D_b, I)\frac{P(M|I)}{P(\{D_b\}|I)}. \tag{2.12}$$

$P(M|D_b, I)$ stands for $P(\tilde{T}, \delta|T_{meas}(z, b), \zeta(z, b))$ here, while D_b is the set of data from all the bursts b. The information from each burst can be combined by multiplying the probability distributions from many bursts. To summarize the results, the most probable value for each parameter is plotted as a data-point, while error bars represent the point where the probability distribution reaches $1/e$ of the maximum. This is a generalization of the standard deviation error bars known as a confidence interval. See Ref. [18] for a discussion of confidence intervals and other topics relating to Bayesian and classical statistics.

2.2.3 Finding the magnetic mode phase

Determining the magnetic mode phase at the Thomson scattering location is done using information from the toroidal magnetic array on MST. The toroidal array measures only the toroidal and poloidal components of the magnetic modes. (The highly-conductive aluminum vacuum vessel of MST is very close to the plasma edge. For short times or rapidly rotating modes, image currents in the wall resist field penetration so that $B_r(r = a) \approx 0$.) The toroidal array provides the amplitude and phase of the Fourier decomposed fluctuations in the toroidal direction only, with resolution up to $|n| = 15$. One can infer that the $|n| > 5$ toroidal modes of $B^n_\theta(a)$ are $m = 1, n > 0$ modes as follows.

For typical discharges, the $n < 0$ modes, which might be resonant at the edge of the plasma where the q-profile reverses sign, are only resonant for very large wavenumbers, which are generally stable. The $m = 0$ modes of all toroidal wavenumbers n are resonant at the reversal surface near the edge of the plasma. However, because the $m = 0$ modes are poloidally symmetric, they produce predominantly toroidal magnetic fluctuations. Thus, the poloidal field is best for measurement of the core $m = 1$ modes. Modes with $n \leq 4$ are never resonant in the core (since $-q(0)$ never reaches 0.25), so the $0 < n \leq 4$ fluctuations are assumed to have $m = 0$. Higher-order ($m \geq 2$) modes are not expected to have significant amplitude. Thus, one can interpret $B_\theta^n(a)$ fluctuations for $5 < |n| < 15$ toroidal mode numbers as belonging to core modes with $m = 1, n > 0$.

The toroidal array, however, provides the phase of the mode referenced to the origin of its own coordinate system, so a coordinate transformation to the Thomson scattering location is needed. This results in a phase shift $\Delta\zeta = m\Delta\theta + n\Delta\phi$. Additionally, as first noted in Parke's thesis [13], because the magnetic axis of the plasma is displaced from the coordinate axis by the Shafranov shift, a further coordinate transform is needed. In this chapter, unless noted otherwise, results are displayed in terms of the vertical position z rather than the r coordinate, which is reserved for the distance from the Shafranov-shifted magnetic axis. The Shafranov shift is discussed in more detail in the next chapter.

Another issue is the sign convention adopted by the automatic mode analysis program which is used to obtain the phase and amplitude of the tearing modes from the toroidal array. The program rectifies the mean poloidal magnetic field before performing the analysis. In the coordinate system used in this thesis (Chapter 8), the usual plasma current direction ($-\hat{\boldsymbol{\phi}}$) causes the mean $B_\theta(a)$ to be negative. This means that the mode amplitudes $B_\theta^n(a)$ reported from the program should take on the opposite sign (or equivalently, the phase should be shifted by π) in the coordinates used in this thesis. (Running MST with 'reversed' plasma

current would eliminate this problem.)

2.3 New fluctuation results

2.3.1 Higher-harmonic content

The previous section describes how tearing mode temperature fluctuation analysis has been conducted to obtain information about the inner workings of an MST plasma. Previously, only the fundamental of the fluctuations have been examined. There might be more fluctuation information available in the form of higher harmonics. The temperature model was modified slightly as follows to probe for the existence of higher harmonics:

$$T(z,t,b) = T_0(z,b) + \tilde{T}_\nu(z)\cos(\nu[\zeta(t,b) + \delta(z)]) + T_{err}(z,t,b). \tag{2.13}$$

Including both the fundamental and the harmonics in the same model would be more computationally-demanding. Instead, note that $\cos\nu\zeta$ is orthogonal to $\cos\zeta$ when integrating over a full period (for $\nu \neq 1$). Thus, it is assumed that each harmonic can be modeled individually, treating the others as part of the background noise.

The ensemble of data was chosen from a set of over one hundred MST discharges for which the Thomson bursts were acquired within 1-3 ms after a sawtooth event (and more than 1 ms before the next). During this time, the q-profile is evolving, and consequently the mode amplitudes and their resonant surfaces change with time after the sawtooth. The evolution of the mode amplitudes is shown in Figure 2.7. The plasma current was between 410 and 385 kA. Densities ranged from 0.8 to 1.5 $\times 10^{19}\mathrm{m}^{-3}$. The core temperature was 300 to 400 eV. In the full ensemble, the mode amplitudes are not restricted. In the restricted ensemble,

the $n = 5, 6$ mode amplitudes were used to select a subset of the full ensemble. The ratio of the $n = 5$ mode edge B_θ to the same quantity for the $n = 6$ mode was limited to be 25 to 75%. Additionally, the root-mean-square (RMS) amplitude for the two modes was limited to 0.4-0.6% (as a percentage of the mean edge poloidal field). These limits select the central one-third of the burst population according to each respective metric (ratio and RMS of the two amplitudes). This ensemble was chosen to ensure that the modes were large enough to interact, while neither mode was sufficiently dominant to count as a quasi-single helicity state.

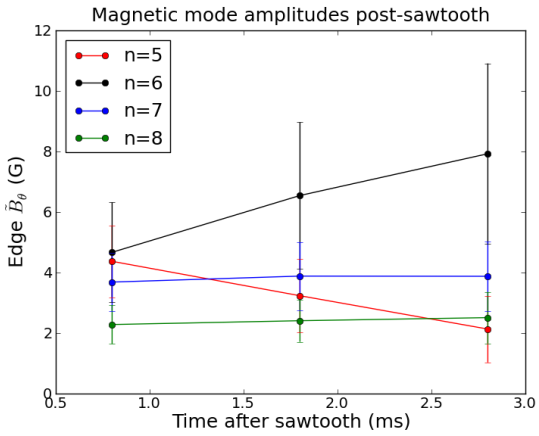

Figure 2.7: Mean and standard deviation of $B_\theta^{(1,n)}(z = a)$ mode amplitudes over time (t=0 is the last sawtooth crash) for the four core-most resonant modes. The q-profile is changing such that the $n = 5$ mode goes out of resonance and drops in amplitude, while the $n = 6$ mode becomes more strongly driven.

The higher-harmonic content of the $n = 6$ mode in the two ensembles is shown in Figure 2.8. There is significant higher harmonic amplitude visible in both the full and restricted ensembles. The higher harmonic structure does not agree with the symmetric, isothermal slab model predictions. First, the amplitude of the higher harmonics ($\nu > 1$) relative to the fundamental $\nu = 1$ is far too large for a symmetric isothermal island. Second, while the isothermal model predicts that all harmonics will be antisymmetric about the rational

surface, the higher harmonics shown here remain finite (as shown) and do not change phase (not shown) at the radius where the fundamental does.

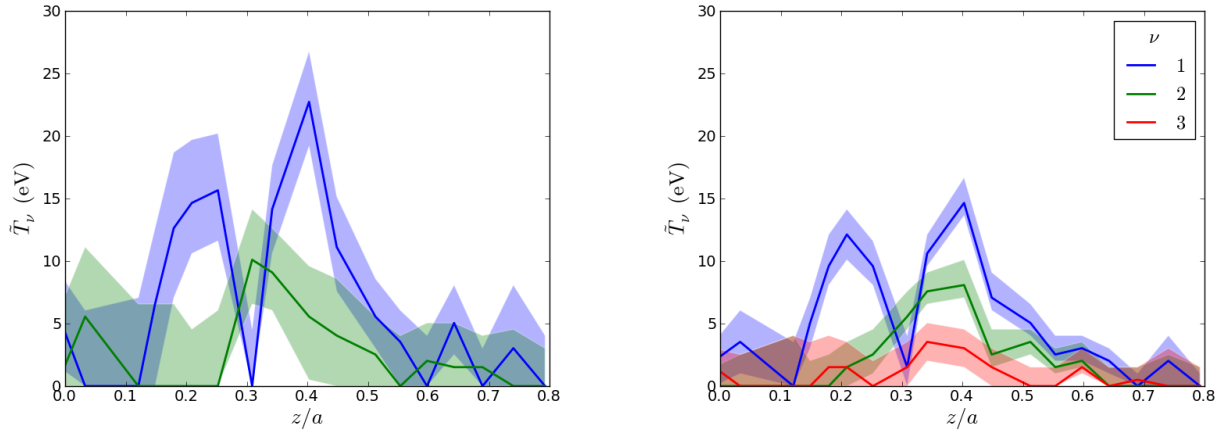

(a) **(b)**

Figure 2.8: (a)Comparison of the fundamental and second harmonic of the $n = 6$ tearing mode temperature fluctuation over the restricted ensemble. The dataset is too small to resolve the third harmonic. (b) The larger dataset allows a sharper view of the harmonics, at the expense of introducing more variability to the mode amplitude, which makes interpretation more ambiguous. However, the qualitative picture of the first two harmonics is the same. The third harmonic is now detectable. It too disagrees with the predictions for the symmetric, isothermal island.

It is also possible to construct a synthetic picture of the mode structure by adding the harmonics of the $n = 6$ mode together with the equilibrium temperature. This provides a more intuitive way of understanding the relative phases of the harmonics. It also reintroduces the information contained in the equilibrium gradient. However, in order to overcome the unevenness of the equilibrium profile due to systematic calibration differences between adjacent polychromators, the equilibrium profile was smoothed by fitting to a 4th-order polynomial (Figure 2.9a). (The equilibrium temperature was obtained by averaging all the temperature measurements, rather than by using a Bayesian method. The statistical uncertainties in the profile are negligible. The jaggedness results from the systematic uncertainties in the

calibrations of the different polychromator units that measure different radial points.)

Figure 2.9b shows the result when the fluctuations are included at their nominal amplitude. The structure appears to be a poloidally narrow island O-point that is approximately isothermal, with an elongated X-point. It is unlikely that the magnetic mode would have the significant higher-harmonic content necessary to produce flux surfaces that would agree with the temperature contours shown in this figure. A possible explanation is that the fluctuations are predominantly coming from a small subset of the bursts (say one-third of the total population) that have larger temperature fluctuations. In this case, the maximum fluctuation amplitude could be much larger than the ensemble-averaged result. Figure 2.9c shows that if the $n = 6$ fluctuation amplitude is increased by a factor of three, the resulting temperature structure looks more like a hot island. While this is not conclusive evidence for a hot island, it does at least demonstrate that the relative phasings of the higher harmonics is consistent with a hot island.

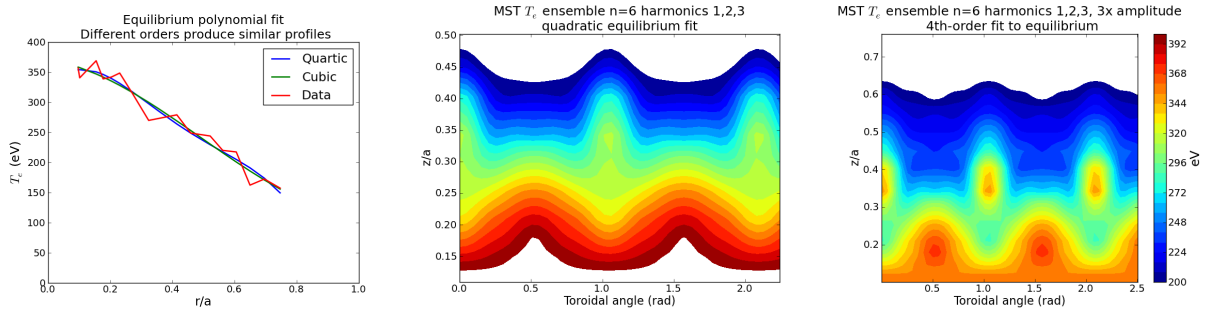

(a) **(b)** **(c)**

Figure 2.9: (a) Fitting the equilibrium temperature with a polynomial in order to remove profile jaggedness resulting from systematic calibration errors. (b) Adding the $n = 6$ fluctuations from Figure 2.8b to the quadratic fit to the equilibrium temperature produces a polodially narrow temperature flattening. (c) Tripling the amplitude of the fluctuations relative to the equilibrium, on the hypothesis that most of the fluctuation is obtained from a small number of shots in the ensemble with larger amplitudes, yields a hot-island type fluctuation.

It is also possible to investigate the harmonic content of the $n = 5$ mode. Figure 2.10 shows that the higher harmonic content is insignificant, despite the fact that the fundamental is larger compared to the $n = 6$ mode. This is an indication that the character of the n=5 mode is different from the $n = 6$. Stephens [9] speculated that the $n = 5$ mode is a kink-type (or ideal) mode which causes a helical distortion of the core flux surfaces without having a separatrix.

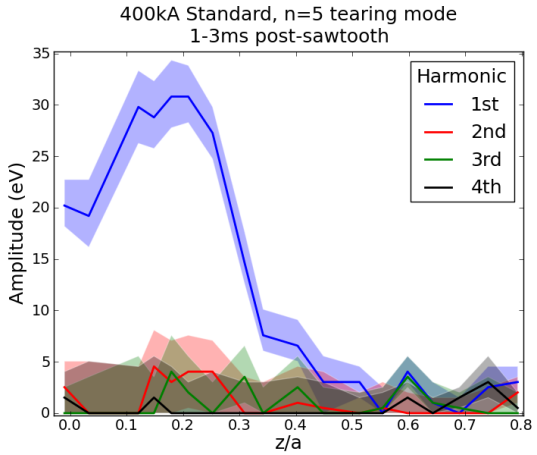

Figure 2.10: Harmonics of then $= 5$ mode for the full ensemble. None of the higher harmonics has significant amplitude. The fundamental amplitude is larger than that of the $n = 6$ mode.

Again, combining the equilibrium temperature with the $n = 5$ fluctuation also produces more illuminating results than simply looking at the fluctuation by itself. In this case, the uncertainty in the equilibrium is enough to obscure the desired conclusions about the flux surface perturbations. In Figure 2.11, the Shafranov-shift-corrected coordinate r/a is used, rather than z/a, because the $n = 5$ mode is resonant near the core. This emphasizes the fact that the Thomson diagnostic does not measure all the way to the magnetic axis. Figure 2.11a shows two possible ways of fitting the equilibrium profile, using a linear fit or a trapezoidal one which constrains the equilibrium gradient to be zero in the core. Both of these fits are

consistent with the data given the systematic uncertainties evidenced by the jaggedness of the profile.

Figure 2.11b and Figure 2.11c show the effect of using the two different fits on the resulting temperature contours. The linear fit results in more circular temperature contours. This would be consistent with flux surfaces for a mode that is far from resonance (that is, with $-q(0)$ significantly less than $1/5$). The trapezoidal fit produces 'D'-shaped temperature contours, which would correspond to a marginally-resonant mode. A reversed gradient in the core is necessary to produce crescent-shaped temperature structure which would be indicative of a resonant mode (not pictured). Thus, it is uncertain from present observations whether the $n = 5$ mode is resonant or not. In order to obtain this information, it would be necessary to reduce the systematic errors in the polychromator system such that the gradient could reliably be established. This was in part the motivation for the efforts to improve the calibration method, documented in Section 6.6.

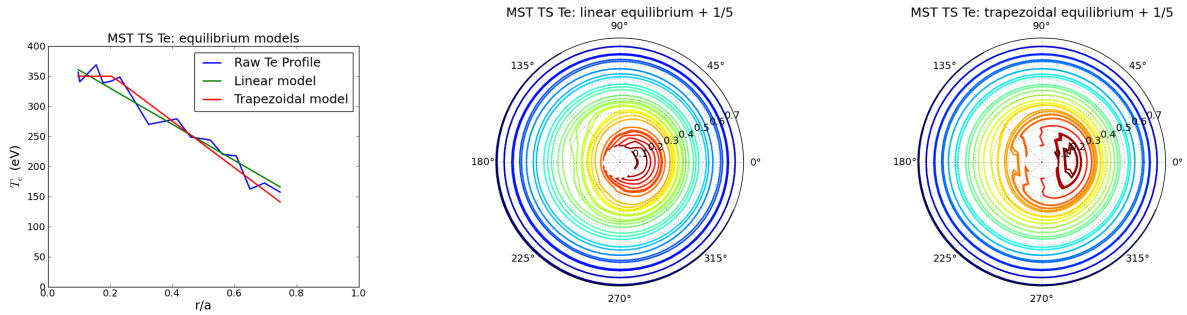

(a) **(b)** **(c)**

Figure 2.11: (a) Fitting the equilibrium profile near the core can be done with or without constraint on the temperature gradient in the core. (b) The effect of using the linear profile is to produce a temperature structure with contours that are convex everywhere. (c) Using a profile with zero gradient in the core causes the temperature contours to be straight in the core. Note that in these figures, the Shafranov shift has been taken into account in both the radius and the phase determination. The radial coordinate here is measured from the shifted magnetic axis rather than the geometric center of the device.

It is helpful to compare the fundamental fluctuation profiles of the various modes. Doing so (Figure 2.12) reveals that the mode fluctuations are overlapping in radius, in agreement with Ref. [10]. This is particularly revealing in terms of the $n = 6$ mode, since this confirms that the island does in fact overlap with the adjacent modes in this ensemble. One would thus expect chaos to develop, which raises the question: why are fluctuations detected that are qualitatively consistent with a model based on closed flux surfaces of a single mode? As argued in the following chapter, magnetic chaos and coherent temperature structures are not always mutually exclusive, at least in the case of marginal chaos.

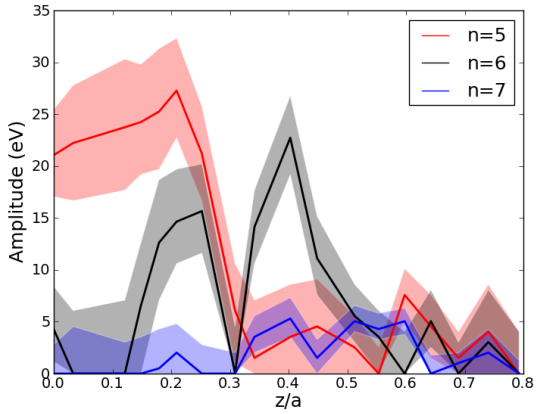

Figure 2.12: The fundamental fluctuation profiles for the $n = 5, 6, 7$ modes. The $n = 5, 6$ mode profiles are from the restricted ensemble, while the $n = 7$ profile was taken from the full ensemble in order to sufficiently resolve the fluctuation. Since the $n = 7$ mode amplitude does not evolve significantly over the inter-sawtooth period, this profile is expected to be representative.

2.3.2 Asymmetric island theory

It is possible to extend the symmetric, isothermal island fluctuation model in slab geometry to include asymmetry or heating/cooling inside the island. Ren *et al* [14] identify two distinct next-order asymmetry terms that modify the shape of the flux surfaces:

$$\Omega \;=\; 8(\frac{x}{W})^2(1+\epsilon_1 x)+(1+\epsilon_2 x)\cos\zeta. \tag{2.14}$$

The ϵ_2 factor causes the X and O-points of the magnetic island to be displaced from the rational surface (in opposite directions), while ϵ_1 causes the island width to be wider on one side of the rational surface than the other (see Figure 2.14). The asymmetry ϵ_1 is related to the curvature of the axisymmetric magnetic field profiles, while ϵ_2 contains information about the tearing mode stability parameter Δ' but also has a contribution from the finite (cylindrical) curvature of the rational surface. For the core modes in MST, the ratio w/r_s is near unity, so this contribution is large.

The fluctuations are described in [14] in terms of the peak-to-peak fluctuation, rather than the harmonic decomposition sought here. Note that in [13], the peak-to-peak fluctuation model (with $\epsilon_1 = \epsilon_2 = 0$) was fit to the fundamental fluctuation. This is not strictly correct. However, it is expected that the parameters of interest (the rational surface location and the island width) will only be minimally affected by the difference between the models (shown in Figure 2.13).

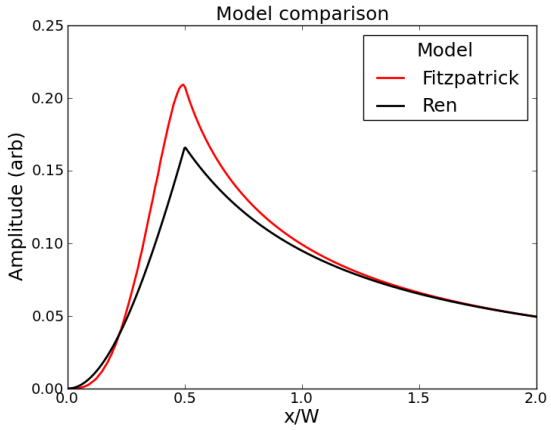

Figure 2.13: Discrepancy between the symmetric, isothermal island fluctuation model of Fitzpatrick [15] and the symmetric case of the more general model of Ren *et al* [14]. Note that the former predicts only the fundamental harmonic, while the later predicts the peak-to-peak fluctuation. The models are scaled to agree at $x/W = 2$.

Asymmetry alone cannot cause the type of harmonic spectrum observed for the $n = 6$ mode in MST. In the symmetric isothermal island model, the zero-crossing of the fundamental indicates the location of the rational surface. In fact, all harmonics go to zero at the same location, as seen in Figure 2.5. This is because the rational surface lies entirely within the island, since it passes through the X-points. Thus, the temperature is constant over mode phase at this radius. It was initially suspected that an asymmetry term such as ϵ_2 could account for the observation of higher harmonics which did not go to zero at the rational surface, without invoking island heating. It is true that an asymmetric island does cause higher harmonic content at the rational surface. However, it also causes the fundamental fluctuation to be finite at the rational surface. In fact, there is still a point in the fluctuation profile where all harmonics must go to zero: the new X-point radius. Referring to Figure 2.8b, note that at no point inside the island are all harmonics zero simultaneously. The fundamental does go to zero, but the higher harmonics remain positive at that point. Thus, the isothermal model, even with asymmetry terms, is not sufficient

to explain the harmonic content observed. A starting point for considering heating inside islands is Ref. [19].

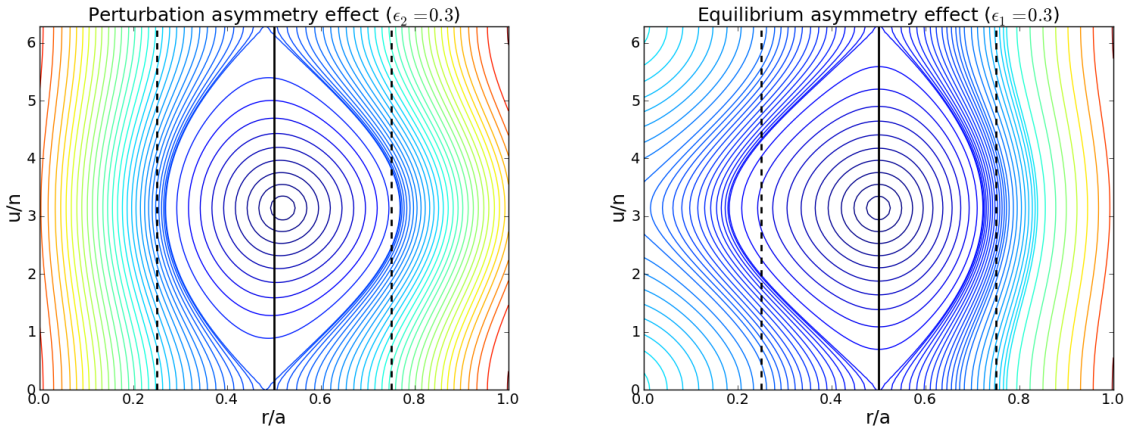

(a) **(b)**

Figure 2.14: Effect of the two asymmetry terms on the flux surfaces of a large island. (a) The ϵ_2 asymmetry term causes the X- and O-points to be displaced displaced radially from the rational surface. Note that there still exists a cylindrical surface ($r = r_X$, where r_X is the radial location of the X-points) which is entirely inside the isothermal island. (b) The ϵ_1 asymmetry causes the island width to be wider on one side, but leaves the X- and O-points in the same place.

This analysis also demonstrates that for an island with asymmetry, the zero-crossing of the fundamental may not be precisely at the rational surface. Asymmetry thus should be accounted for when inferring the rational surface location from fluctuation measurements. For instance, in Refs. [13, 20], the zero-crossing of the fundamental of the temperature fluctuation is interpreted as the rational surface location. This information is used to infer the current density profile changes caused by neutral beam injection (NBI). Although the displacement of the fluctuation zero-crossing from the rational surface is likely to be significantly less than the width of the island (that is, on the order of a centimeter) and more or less stable over time, the displacements in the zero-crossing of the modes due to NBI

are also on the centimeter scale. The possibility of X-point displacement should be taken seriously. Parke found [20] that the higher harmonics were negligible in his dataset. This was favorable, since the symmetric, isothermal model implies small higher harmonics. Going forward, similar analyses should still involve checking for higher harmonic content before a symmetric, isothermal model is applied.

2.3.3 Autocorrelation TS measurement

Tearing modes may not be the only source of temperature fluctuations in the plasma. Other waves and instabilities may be present, particularly at higher frequency. However, the edge toroidal magnetic array might not detect these fluctuations, so it cannot be used as a reference signal. It is possible, however, to autocorrelate the Thomson scattering electron temperature measurements. This technique makes use of the ability to adjust the relative firing times of the two Spectron lasers down to very small ($\sim$ 1 μs) separations δt as illustrated in Figure 2.15a, in order to access information about high-frequency (100's of kHz) fluctuations. (The pulsing period of each individual laser Δt is held fixed at its minimum value, 80 μs.)

Since the pulse sequences are no longer evenly spaced, a simple Discrete Fourier Transform is not usable. Instead one may find the correlation between the temperature measurements from the two lasers. This correlation will include both low and high-frequency waves. However, the sensitivity to the low-frequency waves is virtually independent of the inter-laser timing for $\delta t \ll \Delta t$, since the two samples are practically at the same point on the wave. On the other hand, the sensitivity of the correlation to a given high-frequency wave depends on the relation between the wave period and the relative firing time of the two laser. Thus, if by changing the inter-laser timing, a change in the correlation occurs, a high-frequency fluctuation must be present.

To calculate this specifically, the sample covariance of the two series is written as:

$$\begin{aligned} C &\equiv \frac{1}{N-1}\Sigma_{i=1}^{4}[X(t+i\Delta t)-\bar{X}][X(t+i\Delta t+\delta t)-\bar{X}] \\ \bar{X} &\equiv \frac{1}{8}\Sigma_{i=1}^{8}[X_i] \end{aligned} \tag{2.15}$$

where the mean $\bar{X}$ is taken over all the samples in the burst. The goal is to calculate the expectation of the sample covariance when exposed to an oscillation of a particular frequency, averaging over the phase of the mode. Priestley [21] derives the following relations, essentially a special case of the Wiener–Khinchin theorem. If $S(\omega)$ is the power spectral density of a well-behaved random process with only real values, then:

$$S_+(\omega) = \frac{2}{\pi}\int_0^\infty \cos(\omega\tau)R(\tau)d\tau, \tag{2.16}$$

where the one-sided spectral density for a real process is

$$S_+(\omega) \equiv \begin{cases} 2S(\omega), & \omega > 0, \\ S(0), & \omega = 0, \\ 0, & \omega < 0, \end{cases} \tag{2.17}$$

and the autocovariance function of the random process is

$$\begin{aligned} R(\tau) &\equiv E[(X(t)-\mu)(X(t+\tau)-\mu)] \\ \mu &\equiv E(X) \end{aligned} \tag{2.18}$$

noticing that both R and μ must be independent of t, because this is a stationary process. The operator $E(...)$ is the statistical expectation value over instances of the random process

(not over time). For this case, these relations are used to write the expected value of the sample covariance C in terms of the spectrum S_+ using the spectral sensitivity A of the sample covariance:

$$E(C) = \int_0^\infty A(\omega)S(\omega)d\omega \tag{2.19}$$

$$A(\omega) = \frac{N}{N-1}\cos(\omega\delta t) - \frac{1}{N(N-1)}\sum_{i,j}^{N,N}\cos(\omega\Delta t(i-j)) \tag{2.20}$$

The spectral sensitivity A is plotted for two different values of the inter-laser timing δt in Figure 2.15b. Note that a fluctuation in the 200 kHz range would result in a positive covariance for $\delta t = 5\mu$s and a negative covariance for $\delta t = 1.675\mu$s, while a low-frequency fluctuation would yield a positive fluctuation for both cases. This demonstrates that the technique allows detection of high-frequency fluctuations, in principle.

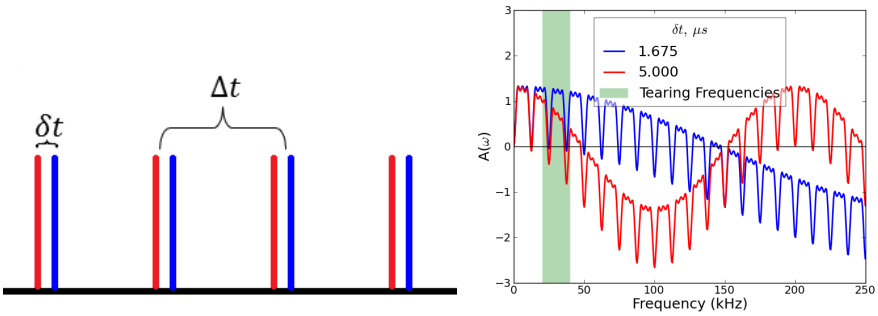

Figure 2.15: (a) Pulse-burst from Spectron lasers with adjustable inter-laser fire time $\delta t \geq 1\ \mu$sand fixed single-laser repetition period $\Delta t = 80\mu$s (not to scale). The two lasers are represented by pulses of different colors. (b) The spectral sensitivity of the sample covariance of a burst measurement for two different inter-laser time separations, illustrating sensitivity to fluctuations at high frequency ($>$ 100 kHz). Note that the sensitivity to the low-frequency fluctuations does not change drastically with pulse separation, while the response to high-frequency fluctuations does. This in principle allows detection of high-frequency fluctuations as distinct from usual tearing mode fluctuations.

Unfortunately, in practice, no conclusive evidence for high-frequency fluctuations was observed. However, three interesting pieces of data emerged. First, this method produced an estimate of the total fluctuation content at low frequency independent of the assumptions of correlation to the tearing modes. The covariance is compared to the squared fluctuation amplitudes from the tearing mode correlation modeling for the same ensemble in Figure 2.16a. (A factor of two is necessary for a correct comparison since the RMS of a coherent signal is $1/\sqrt{2}$ times the amplitude.) The burst covariance shows that there is slightly more total fluctuation power in the temperature measurements than can be extracted by the correlation with the tearing modes. This observation was what initially prompted the investigation of the higher harmonics in Section 2.3.1. It is possible that some of the unexplained fluctuation content is due to inaccuracy in the phase measurement of the tearing modes. More interestingly, it might be possible that some fluctuation depends on the joint phase of two modes

(for instance, the $n = 5, 6$) together. A preliminary check of this hypothesis at $z/a = 0.2$, where both modes are active, did not show any joint correlation.

Second, the fluctuations were reduced to zero (within uncertainties) in the case that the plasma rotation ceased due to mode-locking (not shown), which provides a check on the technique. Finally, in 400 kA PPCD plasmas, the burst covariance was also consistent with zero (Figure 2.16b). (For more about PPCD see Chapter 5.) While the error bars were larger, the relative error levels were comparable between the standard and PPCD cases since the PPCD temperatures are also higher than standard plasmas at the same current. This lack of observation of tearing mode fluctuations in PPCD is consistent with the findings of Stephens [10]. The reduction of the tearing mode amplitude in PPCD and the flattening of the equilibrium gradient in the core appears to eliminate the correlated and uncorrelated fluctuations.

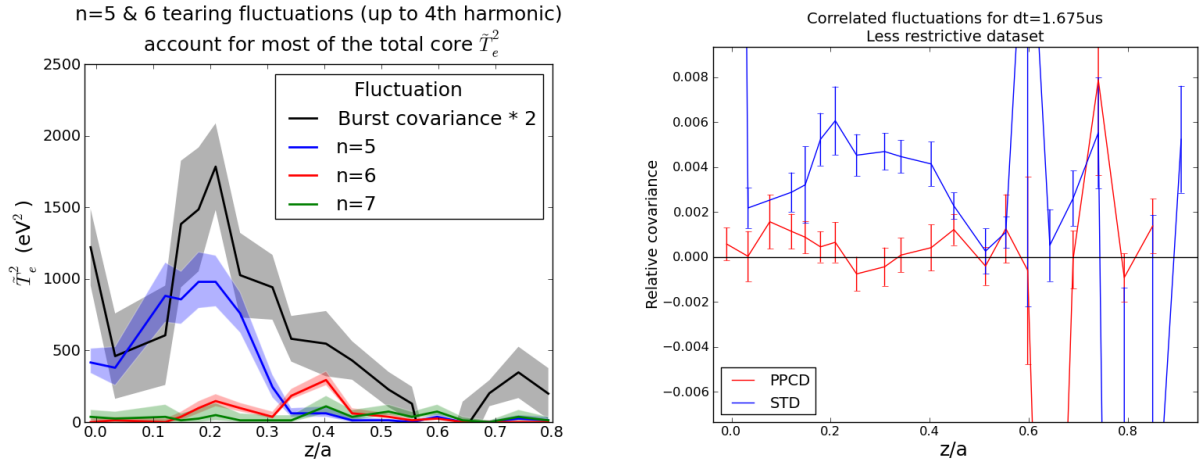

(a) **(b)**

Figure 2.16: (a) The burst covariance ($\delta t = 1.675\mu$s) is compared with the fluctuation energy $\tilde{T}^2$ for the various core tearing modes. (b) Comparison of the burst covariance normalized by the square of the mean temperature for standard and PPCD plasmas at 400 kA. The core-most point and the points beyond $z/a > 0.6$ are unreliable in this analysis. PPCD has much smaller relative electron temperature fluctuations.

References

[1] J. H. Friedman, International Statistical Review **69**, 5 (2001).

[2] D. J. Den Hartog, D. J. Holly, R. O'Connell, R. J. Beach, S. A. Payne, and T. N. Carlstrom, Review of Scientific Instruments **74**, 1653 (2003).

[3] D. J. Den Hartog, J. R. Ambuel, M. T. Borchardt, J. A. Reusch, P. E. Robl, and Y. M. Yang, Journal of Physics: Conference Series **227**, 012023 (2010).

[4] W. C. Young and D. J. Den Hartog, Journal of Instrumentation **10**, C12021 (2015).

[5] I. H. Hutchinson, *Principles of Plasma Diagnostics*, 2nd ed. (Cambridge University Press, 2002).

[6] W. S. Harris, D. J. Den Hartog, and N. C. Hurst, Review of Scientific Instruments **81**, 10D505 (2010).

[7] D. J. Den Hartog, N. Jiang, and W. R. Lempert, Review of Scientific Instruments **79**, 10E736 (2008).

[8] J. A. Reusch, M. T. Borchardt, D. J. Den Hartog, A. F. Falkowski, D. J. Holly, R. O'Connell, and H. D. Stephens, Review of Scientific Instruments **79**, 10E733 (2008).

[9] H. D. Stephens, D. J. Den Hartog, C. C. Hegna, and J. A. Reusch, Physics of Plasmas **17**, 056115 (2010).

[10] H. D. Stephens, *Electron Temperature Structures Associated With Magnetic Tearing Modes in the Madison Symmetric Torus*, Phd thesis, University of Wisconsin - Madison (2010).

[11] C. P. Kasten, *Electron Temperature Fluctuations During Magnetic Reconnection in the Reversed-Field Pinch*, Undergraduate thesis, University of Wisconsin - Madison (2011).

[12] C. P. Kasten, D. J. Den Hartog, H. D. Stephens, C. C. Hegna, and J. A. Reusch, Plasma Physics and Controlled Fusion **53**, 112001 (2011).

[13] E. Parke, *Diagnosis of Equilibrium Magnetic Profiles, Current Transport, and Internal Structures in a Reversed-Field Pinch Using Electron Temperature Fluctuations*, Phd thesis, University of Wisconsin - Madison (2014).

[14] C. Ren, J. D. Callen, T. A. Gianakon, C. C. Hegna, Z. Chang, E. D. Fredrickson, K. M. McGuire, G. Taylor, and M. C. Zarnstorff, Physics of Plasmas **5**, 450 (1998).

[15] R. Fitzpatrick, Physics of Plasmas **2**, 825 (1995).

[16] R. Munroe, "Frequentists Vs. Bayesians," .

[17] Z. Weinersmith, "Bayesian Drinking Game," (2014).

[18] R. D. Cousins, American Journal of Physics **63**, 398 (1994).

[19] J. Berrino, E. Lazzaro, S. Cirant, G. D'Antona, F. Gandini, E. Minardi, and G. Granucci, Nuclear Fusion **45**, 1350 (2005).

[20] E. Parke, J. K. Anderson, D. L. Brower, D. J. Den Hartog, W. X. Ding, C. A. Johnson, and L. Lin, Physics of Plasmas **23**, 056108 (2016).

[21] M. B. Priestley, *Spectral Analysis and Time Series.* (Academic Press, London;New York, 1981).

3 Observation and Modeling of a Hot Remnant Island

> *Remember that all models are wrong; the practical question is how wrong do they have to be to not be useful.*
>
> — George E. P. Box and Norman R. Draper [1]

The previous chapter contained an analysis of tearing modes based on the electron temperature fluctuations captured using the Spectron lasers. The limited sampling rate and number of samples per burst required statistical analysis of large ensembles of data from many shots. In this chapter, the focus is on new results using the Fast Laser, which has provided clear two-dimensional observations of rotating tearing mode temperature structures in a single discharge. Section 3.1 introduces the Fast Laser and the best example of the temperature structures it has captured to date: a large hot spot in the shape of a magnetic island. Section 3.2 explains how the internal magnetic field structure of the plasma is modeled in order to understand the origin of the temperature structure. The $n = 6$ tearing mode produces a large island of the correct size, radial location, and phase to explain the temperature structure. However, the $n = 6$ island is disrupted by overlap with the neighboring $n = 7$ island, producing chaos (Section 3.3). The conventional understanding holds that chaotic field lines imply very large values of thermal transport. However, in the present case, the thermal con-

ductivity ($\chi_{e,m} \approx 30\,\mathrm{m}^2/\mathrm{s}$) estimated from field line tracing is consistent with the inferred thermal conductivity ($\chi_{e,th} \approx 10 - 40\,\mathrm{m}^2/\mathrm{s}$) in the Ohmically-heated island.

3.1 Hot island observation

3.1.1 Fast Laser

Both the Spectron lasers and the Fast Laser employ a master oscillator (which generates 'seed' pulses) with multiple power amplifier laser rods which build up the energy of the seed pulse as it passes through them. There are two primary features of the Fast Laser which enable the high performance it achieves [2, 3, 4]. First, the Fast Laser has an optimized set of amplifier rods to increase the output energy (and hence the number of pulses). The first 4 amplifier rods in the Fast Laser are Nd:YAG crystal rods (the same type used in the Spectrons). The final two amplifier rods in the Fast Laser are large Nd:glass rods, which have lower gain than Nd:YAG rods but are capable of storing more energy. This combination allows the Fast Laser to amplify the small seed pulses produced by its master oscillator while simultaneously delivering more optical energy in a burst than the Spectron lasers.

The second improvement is the high-repetition-rate master oscillator. At the time when the data presented in this chapter was taken, the Fast Laser contained a diode-pumped solid state master oscillator [2]. The highest achieved repetition rate with this configuration was 75 kHz. The data in this chapter was obtained with the laser operating at 66 kHz, producing 3 bursts of 25 pulses each during a single MST discharge. The temperature measurement sampling rate could then be greater than typical tearing mode fluctuation frequencies (10-50 kHz), allowing the structure of the tearing mode to be resolved with great detail.

Since then, the Fast Laser has been upgraded with a continuous master oscillator whose

output is rapidly chopped with an acousto-optic modulator (AOM) to produce seed pulses for subsequent amplification [3, 4]. The modulator has a very high switching rate (50 MHz bandwidth), which allows 20 ns seed pulses to be produced at up to 1 MHz repetition rate. The maximum achieved repetition rate of the Fast Laser with the AOM is 333 kHz with bursts of 4 laser pulses each. At 125 kHz repetition rate, the burst length is extended to 63 pulses, with one burst per MST discharge. In this mode of operation, the Fast Laser provides almost 8 times as many consecutive datapoints in a burst, and more than twice as many total datapoints in an MST discharge, compared to the Spectron system.

3.1.2 Rotating hot island observation

A remarkably clear observation of a rotating electron temperature structure associated with a large $n = 6$ tearing mode was captured in MST discharge 1140726089. Figure 3.1a shows the electron temperature over radius and time, exhibiting three consecutive periods of the mode rotation past the diagnostic. The presence of a locally peaked electron temperature structure is obvious at $r/a \approx 0.3$. Figure 3.1b shows that the fluctuation is much larger than the uncertainties in the measurements.

Three factors made this observation so definitive. First, the $n = 6$ mode was the dominant mode in the plasma, with edge-measured amplitude $B_\theta = 13\,\mathrm{G}$. The other modes with $n > 6$ had amplitudes $B_\theta < 2.6\,\mathrm{G}$. The $n = 5$ mode had very low amplitude: $B_\theta = 0.75\,\mathrm{G}$. While this shot had the same plasma current $I_p = 400$ kA as the shots from the previous chapter, it had lower reversal parameter ($F = -0.3$) compared to the shots of the previous chapter ($F = -0.2$). This caused the $n = 5$ tearing mode to be non-resonant ($-q_{max} < 1/5$).

Second, the electron density was unintentionally increased to $n_e = 1.6 \times 10^{19}\,\mathrm{m}^{-3}$ during this shot (the target for the day was $0.5 \times 10^{19}\,\mathrm{m}^{-3}$), which increased the number of scattered

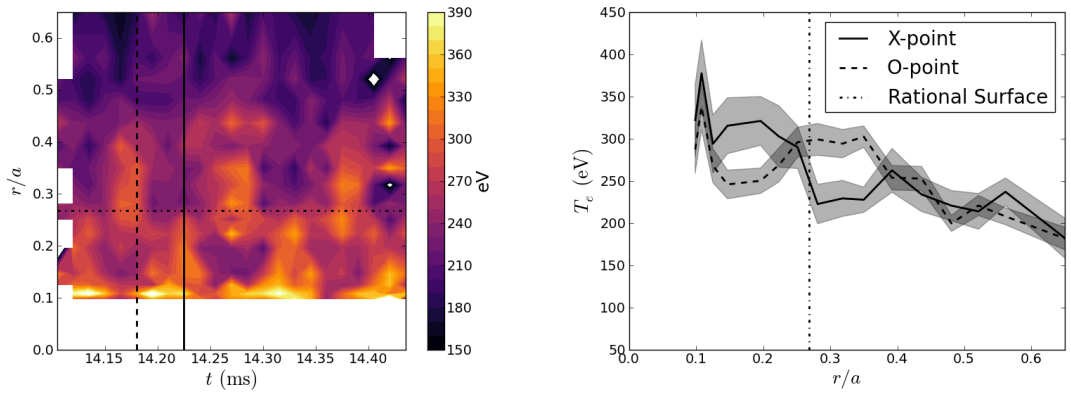

(a) **(b)**

Figure 3.1: (a) Contour plot of the electron temperature as a function of time and radial location exhibiting three rotations of a localized temperature peak at $r/a \approx 0.3$. Also note the heated core region at $r/a < 0.3$ and the colder plasma separating the two. (b) Temperature profiles with uncertainty ranges for the two time points denote by the corresponding vertical lines in (a). The peak-to-trough temperature fluctuation is $\approx 100\,\text{eV}$, several times the one-standard-deviation uncertainty range (shaded).

photons and hence the signal-to-noise ratio of the TS diagnostic. Third, while the Fast Laser was operating at 65 kHz, the rotation frequency of the large $n = 6$ tearing mode also happened to be low (10 kHz), allowing several temperature profiles to be obtained during each period of the structure's rotation past the diagnostic. Several other possible island structures were observed as well, but with lower signal-to-noise ratio due to reduced n_e.

Applying the fluctuation analysis techniques of the previous chapter to this data provides insight into the higher harmonic content of the $n = 6$ temperature fluctuations. Figure 3.2 shows that the second harmonic is similar in relative amplitude and radial profile compared to the second harmonic content in the ensemble-averaged data of the previous chapter. This lends further credence to the conclusion that the ensemble-averaged data reflects the presence of hot islands.

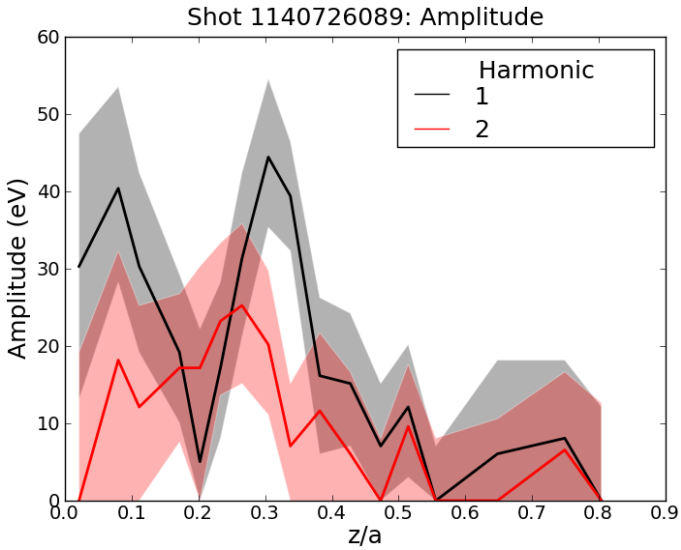

Figure 3.2: The fundamental and second harmonic of the $n = 6$ T_e fluctuation shown in Figure 3.1.

3.2 MHD modeling and n=6 flux surfaces

The next step is to compare the size and location of the observed temperature structure against the predicted $n = 6$ magnetic island. Hudson [5] and Biewer [6] developed a technique to model the $n = 6$ magnetic structure by combining reconstructions of the mean (or 'equilibrium') magnetic fields with models of the tearing mode magnetic fields derived from MHD simulations. Then the flux surfaces for the $n = 6$ magnetic island (neglecting the other tearing modes for the moment) can be found, to see how the temperature structure matches the shape of the $n = 6$ island. The agreement is found to be good, validating this approach.

The MHD simulations are done in periodic cylindrical coordinates, while the equilibrium reconstruction is toroidal. The flux surface calculation is done in periodic cylindrical coordinates (which simplifies the math), so the equilibrium model is adapted to periodic cylindrical geometry. For more about MST coordinates and conversions to DEBS periodic cylindrical coordinates see Chapter 8. A fully toroidal calculation would be preferable. However, the

toroidal effects are not important for a qualitative understanding of the magnetic structure. It is necessary to account for the Shafranov shift (a toroidal effect, described below) which impacts the locations of the TS measurement points relative to the magnetic axis of the plasma.

3.2.1 Equilibrium reconstructions

The process begins with MSTFIT reconstruction of the MST discharge. MSTFIT is an axisymmetric equilibrium solver [7]. It solves the Grad-Shafranov equation in ideal MHD, balancing the plasma thermal pressure against the magnetic pressure $\nabla P = \mathbf{J} \times \boldsymbol{B}$ with the assumption of rotational symmetry in the toroidal angle (axisymmetry). The plasma pressure is supplied by combining the density measured from an interferometer with the mean temperature profile from Thomson scattering. The total toroidal current and flux of the plasma, as well as poloidal magnetic fields, are measured with coils around the outside of the plasma, providing constraints. The code guesses initial current and pressure profiles and iteratively adjusts them to minimize disagreement with the measurements, quantified by a χ^2 cost function.

The axisymmetric flux surfaces produced by MSTFIT are shown in Figure 3.3a. MSTFIT assumes that flux surfaces are circular but not necessarily concentric. The Shafranov shift $\Delta R = R_{surf} - R_0$ is an outward displacement in major radius R of the centers of the flux surfaces R_{surf}. The shift increases as the flux surface radius ρ decreases, with maximum shift occuring at the magnetic axis ($\rho = 0$). The Shafranov shift prevents the Thomson scattering diagnostic from measuring all the way to the magnetic axis. The Shafranov shift also causes a phase shift because the TS measurement points go from below the magnetic axis to beside it, a 90° rotation in poloidal angle as measured from an origin centered on the magnetic axis

(see Figure 3.3a). These effects were noted by Parke in [8] and illustrated graphically in [9, Fig. 2.20]. The corrected poloidal angle and the flux surface radius at the TS measurement points (in the cylindrical approximation to MST) are

$$\theta = \frac{\pi}{2} + \tan^{-1}\left(\frac{\Delta R}{z}\right) \tag{3.1}$$

$$r = \sqrt{z^2 + (\Delta R)^2} = \rho, \tag{3.2}$$

where θ is measured in the right-handed system used in this thesis, with $\theta = 0$ at the outboard midplane. Also recall that z is measured downward from the midplane in the context of TS measurement locations.

The q-profile from MSTFIT is correct for the field lines as they lie on the flux surfaces in toroidal geometry. However, using the poloidally-averaged magnetic field $\langle B_{tor}\rangle$, $\langle B_{pol}\rangle$ profiles from MSTFIT in periodic cylindrical geometry would result in an incorrect q-profile:

$$q_{tor} = \left\langle \frac{\rho B_{tor}(\rho,\theta)}{R(\rho,\theta)B_{pol}(\rho,\theta)} \right\rangle \neq \frac{\rho\langle B_{tor}(\rho)\rangle}{R_0\langle B_{pol}(\rho)\rangle} = q_{cyl} \tag{3.3}$$

Therefore, to maintain the proper field line pitch, it is necessary to modify at least one of the two mean field profiles. It is most natural to adjust the toroidal field (shown in Figure 3.3b) while preserving $\langle B_{pol}\rangle$ and q_{tor}. The conversion from MSTFIT profiles to a periodic cylindrical system is then

$$q_{cyl} \equiv q_{tor} \tag{3.4}$$

$$B_\theta \equiv \langle B_{pol} \rangle \tag{3.5}$$

$$B_z \equiv \frac{q_{tor} R_0 \langle B_{pol} \rangle}{\rho}. \tag{3.6}$$

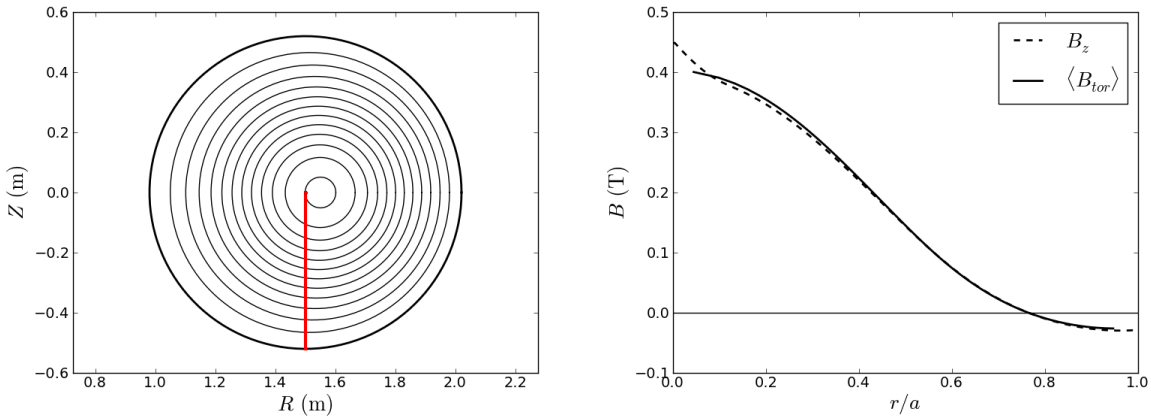

(a) **(b)**

Figure 3.3: (a) Axisymmetric flux surfaces in a toroidal plane $\phi = const.$ from MSTFIT. The red vertical line denotes the TS measurement positions. (b) The toroidal field from MSTFIT is adjusted slightly to give the correct q-profile in a periodic cylindrical calculation. Here B_Z is the 'toroidal' field in periodic cylindrical geometry.

3.2.2 Tearing mode magnetic fields

The tearing mode magnetic fields are derived from DEBS MHD simulations. DEBS [10] is a nonlinear 3D viscoresistive MHD simulation in periodic cylindrical geometry. RFP simulations with DEBS exhibit many aspects of MST plasmas, especially tearing mode activity and the sawtooth cycle. However, the simulated tearing mode amplitudes are typically twice as large as those observed in MST. The cause of the discrepancy has not been identi-

fied conclusively, although it may be due to two-fluid effects not captured by DEBS (which uses single-fluid MHD) [11, 12]. The modes are consequently rescaled to match the amplitudes measured by the toroidal array in MST at a particular time. This operation, and the ensemble-averaging described in the next paragraph, mean that the modes are no longer a consistent solution of the nonlinear equations. The use of the DEBS modes is motivated by the fact that the MST tearing modes are in the nonlinear, rather than the linear, regime.

Because the simulations are dynamic in time, especially with respect to the sawtooth cycle, it is necessary to find the tearing mode structure at times which match the conditions of the MST discharge at the time the observation of the temperature structure took place. The particular simulation used here is one conducted by J. A. Reusch, detailed in [13, ch. 5], which includes plasma pressure. The equivalent plasma current was 400 kA, but the reversal parameter was slightly less negative ($F = -0.22$ on average) than the MST discharge ($F = -0.32$). Therefore, the tearing mode structure was produced by averaging over times during the DEBS simulation where $F \approx -0.32$.

In a periodic cylinder, each tearing mode magnetic field is composed of a single Fourier mode in toroidal and poloidal angle. Each vector component of $\mathbf{B}^{(m,n)}(r,\theta,Z)$ can be written as $B_x^{(m,n)}(r,\theta,Z) = B_{x,c}^{(m,n)}(r)\cos\zeta + B_{x,s}^{(m,n)}(r)\sin\zeta$, where $\zeta = m\theta + n\frac{Z}{R_0} + \delta(t)$ is the helical phase angle of the mode, and x stands for one of $\{r,\theta,Z\}$. (Here Z is denotes the 'toroidal' coordinate in periodic cylindrical geometry, where z is reserved for the vertical direction in MST Thomson system coordinates.) In periodic cylindrical simulations it happens that the radial component $B_r^{(m,n)}$ is $\pi/2$ radians out of phase from the other two components, with the phase of each component remaining constant in radius [12]. With the convention that $B_\theta^{(m,n)}(r,\zeta) = B_\theta^{(m,n)}(r)\cos\zeta$ (which fixes the mode phase δ), the other two components become $B_z^{(m,n)}(r)\cos\zeta$ and $B_r^{(m,n)}(r)\sin\zeta$. From this point on the subscripts c, s are dropped. The amplitude of the mode is normalized during the ensemble-averaging process such that

$B_\theta^{(m,n)}(a) = 1$. The averaging procedure thus yields a characteristic field for the mode which can then be set to match the phase and amplitude of the measurement of $B_\theta^{(n)}(a)$ from the toroidal array in MST.

The time evolution of the reversal parameter in the DEBS simulation is shown in Figure 3.4a. The effect on the $n = 6$ mode from changing the constraint on F for the ensembling procedure is seen in Figure 3.4b to be small relative to the uncertainties. This shows that the mode structure is not highly sensitive to this ensembling criterion. Proximity to a sawtooth event does not cause especially large variability in the mode structure.

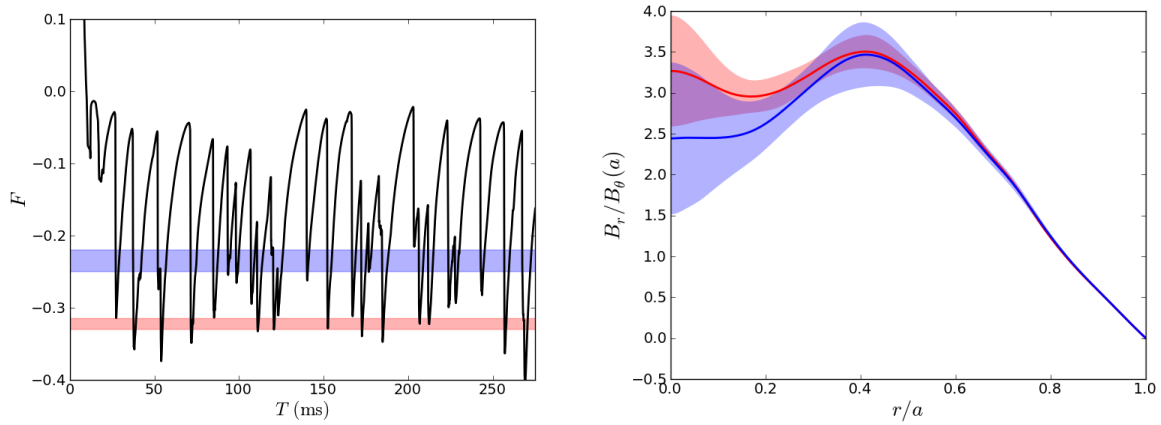

(a) **(b)**

Figure 3.4: (a) The reversal parameter F exhibits sawteeth in the DEBS simulation. The lower shaded region represents the range of F which matches the MST discharge, while the upper shaded region was used to test the extent to which the mode structure varied with reversal parameter. (b) The effect on the $n = 6$ mode B_r structure from using the two ranges of the reversal parameter F is not much larger than the standard deviation (shaded band) within either ensemble.

3.2.3 Helical coordinates and fluxes

One good reason for working in the periodic cylinder as an approximation to a torus (beyond the restrictions of DEBS) is the possibility of turning a three-dimensional problem into a two-dimensional one by making use of helical symmetry. The transformation from cylindrical coordinates into helical coordinates uses the relations

$$r = r \tag{3.7}$$

$$\zeta = m\theta + n\frac{Z}{R_0} + \delta \tag{3.8}$$

$$\eta = p\theta + lZ, \tag{3.9}$$

where the coordinate ζ is the helical phase of the tearing mode. One can chose p, l (which define the ignorable coordinate η) in any way one pleases, as long as η is linearly independent of ζ. Particularly simple choices are $\eta = \theta$ or $\eta = Z$. Nothing depends on this choice, since it is assumed that the magnetic field only depends on r, ζ. (This is not true in toroidal geometry, since the toroidal curvature breaks the symmetry in the poloidal direction. It can be shown that a cylindrical helical coordinate system is the most general coordinate system in which there exists a continuous symmetry direction [14, 15].)

The goal then becomes to find a helically-symmetric flux function in this coordinate system. A flux function ψ has the property that $\mathbf{B} \cdot \nabla\psi = 0$, which means that the component of the magnetic field which is normal to a surface of constant flux is always zero. This implies that a magnetic field line which starts on a flux surface remains on it always, and that no field lines pass through a flux surface. Biskamp [16, ch.2] shows that a divergence-free magnetic field with helical symmetry can be written as

$$\mathbf{B} = \nabla\psi(r,\zeta) \times \mathbf{h} + \mathbf{h} f(r,\zeta). \tag{3.10}$$

The flux function ψ obviously satisfies $\mathbf{B} \cdot \nabla\psi = 0$ when $\mathbf{B}$ is defined this way. Here $\mathbf{h}$ is a vector that points in the symmetry direction. It is one of three orthogonal vectors used in this coordinate system (hatted vectors have unit length):

$$\boldsymbol{\zeta} \equiv r\nabla\zeta = m\hat{\boldsymbol{\theta}} + \frac{nr}{R_0}\hat{\mathbf{z}} \tag{3.11}$$

$$\hat{\mathbf{r}} = \nabla r \tag{3.12}$$

$$\mathbf{h} \equiv \frac{1}{|\boldsymbol{\zeta}|}\hat{\mathbf{r}} \times \hat{\boldsymbol{\zeta}} = \frac{m\hat{\mathbf{z}} - \frac{nr}{R_0}\hat{\boldsymbol{\theta}}}{m^2 + (\frac{nr}{R_0})^2}. \tag{3.13}$$

The vector $\boldsymbol{\zeta}$ can be thought of as the wavevector of the tearing mode. The component of $\mathbf{B}$ parallel to $\mathbf{h}$ (given by f) is the part of the field parallel to the symmetry direction. It is uninformative as to the shape of the flux surfaces. In order to find the flux surfaces from a magnetic field, it is necessary to analyze the other two components of $\mathbf{B}$ arising from $\nabla\psi \times \mathbf{h}$, which are perpendicular to the symmetry direction. Since ψ only depends on r, ζ, one can write:

$$\nabla\psi = \frac{\partial\psi}{\partial\zeta}\nabla\zeta + \frac{\partial\psi}{\partial r}\nabla r. \tag{3.14}$$

Inserting the gradient expression into $\nabla\psi \times \mathbf{h}$ leads to an equation for the components of $\mathbf{B}$ in the directions perpendicular to $\mathbf{h}$:

$$\frac{\partial \psi}{\partial r} = -\mathbf{B} \cdot \boldsymbol{\zeta} = -\left(mB_\theta + \frac{nr}{R_0} B_Z\right) \tag{3.15}$$

$$\frac{\partial \psi}{\partial \zeta} = rB_r. \tag{3.16}$$

It is now possible to solve for ψ in terms of a specified $\mathbf{B}$ with helical symmetry. Like the magnetic field, the flux can be separated into a mean (or 'equilibrium') part which is independent of ζ, and a fluctuating part due to the tearing mode: $\psi(r, \zeta) = \psi_0(r) + \psi_1(r) \cos \zeta$. Equation 3.16 yields a direct relationship between the tearing mode radial field and the oscillating part of the flux:

$$\psi_1(r) \sin \zeta = r B_r^{(m,n)}(r) \sin \zeta. \tag{3.17}$$

This shows that $B_r^{(m,n)}(r)$ is the only vector component of $\mathbf{B}^{(m,n)}$ necessary to specify the tearing mode's contribution to the helical flux (and hence the size and shape of the island). The equilibrium part of the helical flux $\psi_0(r)$ is found by numerical integration:

$$\psi_0(r) = -\int_0^r \left(mB_\theta^{(0,0)}(r') + \frac{nr}{R_0} B_Z^{(0,0)}(r')\right) dr'. \tag{3.18}$$

The resonance condition $q = -m/n$ corresponds to

$$\frac{\partial \psi_0}{\partial r} = -mB_\theta^{(0,0)} \left(1 + \frac{nq}{m}\right) = 0, \tag{3.19}$$

which shows that the island occurs at the local maximum (or minimum) of ψ_0. Note that the equilibrium helical flux ψ_0 is still specific to the helicity defined by $\zeta = m\theta + nZ/R_0 + \delta$. Also note that any monotonic function F of ψ will serve as a flux surface coordinate, since such

a re-scaling will change the magnitude of $\nabla\psi$ but not the direction, preserving the property $\mathbf{B}\cdot\nabla F(\psi) \propto \mathbf{B}\cdot\nabla\psi = 0$.

It can be shown [17, p. 181] that the fluctuating part of $f(r,\zeta)$ associated with the mode must go to zero at the edge of the plasma if we impose the boundary condition that current cannot not flow across the vacuum boundary layer from the plasma into the wall: $J_r(a) = 0$. Inserting the fluctuating part of the magnetic field in the symmetry direction $\mathbf{B}_h^{(m,n)} \equiv f_1(r)\cos(\zeta)\mathbf{h}$ into expression for the radial current density from Ampere's law,

$$\mu_0 J_r = \frac{1}{r}\frac{\partial B_Z}{\partial\theta} - \frac{\partial B_\theta}{\partial z}, \tag{3.20}$$

leads to

$$\mu_0 r J_r = -f_1(r)\sin\zeta. \tag{3.21}$$

Therefore, at $r = a$, we expect that the fluctuating magnetic field has $\mathbf{B}\cdot\mathbf{h} = 0$. Due to the conducting wall, $\mathbf{B}\cdot\hat{\mathbf{r}} = 0$ as well. The only remaining component of the fluctuating magnetic field at the edge is that in the direction of $\boldsymbol{\zeta}$. Another way to state this is that (at the edge) the mode is polarized along the direction $\boldsymbol{\zeta}$ of the wavevector. This is observed to hold true for the DEBS modes, and is approximately correct for MST mode measurements as well (although toroidicity changes this picture slightly [17, ch. 8]).

Combining $\mathbf{B}\cdot\mathbf{h} = 0$ with Equation 3.15 yields

$$\frac{\partial\psi}{\partial r} = -mB_\theta\left(1 + \left(\frac{nr}{mR_0}\right)^2\right). \tag{3.22}$$

Thus at $r = a$, $B_\theta^{(m,n)}$ and ψ_1 should have the same phase dependence (as $\cos\zeta$), with a

possible sign difference. Note that $\psi_1(r)$ must be go to zero at $r = a$, since $B_r(r) \propto \psi_1(r)$ must be zero at the wall. That makes $\frac{1}{\psi_1}\frac{\partial \psi_1}{\partial r} < 0$. Then $mB_\theta^{(m,n)}/\psi_1$ is positive. Thus the phase of the flux is the same as the phase of $B_\theta^{(m,n)}(a)$, with the convention that $m > 0$. The relationship between the X-point and O-point locations and the phase of the mode depends on the curvature $\psi_0''(r_s) \approx mB_\theta^{(0,0)} q'(r_s)$ of the equilibrium flux at the rational surface radius. (Here primes denote radial derivatives.) Positive $\psi_0''(r_s)$ makes the X-point at $\zeta = 0$, while $\psi_0''(r_s) < 0$ makes the O-point at $\zeta = 0$. In the case of MST, the O-point is at $\zeta = 0$, which is reversed from [18] due to a difference in the sign of ψ_0''.

3.2.4 Comparison of temperature structure and n=6 flux surfaces

The flux surfaces with the $n = 6$ mode from DEBS (re-scaled to match the $B_\theta^6(a) = 13\,\mathrm{G}$ measured in MST) and the equilibrium from MSTFIT are shown in Figure 3.5. The width of the modeled $n = 6$ island is 16 cm, or 31% of the minor radius. The temperature peak is centered on the island O-point. The low-r side of the separatrix matches the edge of the hot core region as well. There are no adjustable parameters in this model, so the agreement was not a forgone conclusion. This gives a great deal of support to the accuracy of the magnetic modeling. Note that the O-point of the island is at $\zeta = 0$ as expected. There is variation of T_e along flux surfaces. Some of variation may be attributed measurement errors (both systematic and random), as well as to remaining misalignment of the flux surfaces with the ideal $n = 6$ flux surfaces. It is possible, but not certain, that there is actual structure in T_e not captured by the pure $n = 6$ field structure.

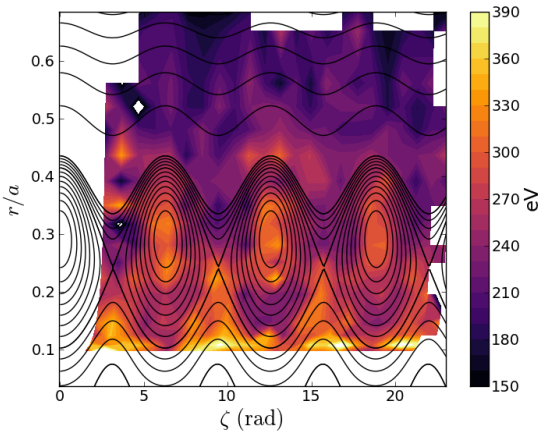

Figure 3.5: T_e color contours overlayed with flux contours (black) as a function of helical angle and flux surface radius. The TS measurement positions have been corrected for the Shafranov shift in both radius and poloidal angle.

3.3 Field line tracing and quantifying chaos

Although the $n = 6$ mode was by far the largest-amplitude mode in MST at the time the temperature structure was observed, it was not the only mode. As it happened, the adjacent $n = 7, 8$ tearing modes were sufficiently large to interfere with the $n = 6$ island, as is shown by the overlap of the island widths in Figure 3.6. Overlap of islands with different helicities breaks the helical symmetry that underpins the flux surface modeling of the previous section, producing chaotic magnetic field trajectories that require a full three-dimensional calculation. However, it appears that the field line wandering is sufficiently constrained by the residual effect of the $n = 6$ island that the temperature peaking can be explained.

3.3.1 Magnetic chaos

The MAL code [5, 6, 11, 13] is part of the RIO suite of tools for calculating field and particle trajectories in a magnetized plasma. Although MAL (unlike DEBS) is compatible with both

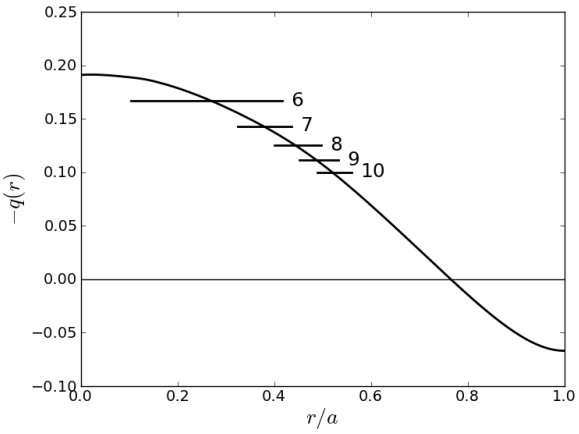

Figure 3.6: Widths and resonant locations of the core-most several tearing mode islands, displaying significant radial overlap.

periodic cylindrical and toroidal geometries, the calculations in this section were done in periodic cylindrical coordinates. The fields for the remaining tearing modes were determined in the same manner as for the $n = 6$ mode described in Section 3.2.2. The same ensemble criterion was used, $-0.33 < F < -0.315$. The phases of all the modes were set to zero. The mode amplitudes were rescaled to match the toroidal-array-measured values for $B_\theta^{(m,n)}(r = a)$. The fields are summarized in Figure 3.7. The fields were then provided to MAL, along with a set of initial positions for the field lines. MAL then traced the field lines for a specified number of steps (in this case, up to two kilometers of field line length).

If only a single tearing mode is inserted, the field lines should trace out the flux surfaces of the island. This allows benchmarking between the flux surface calculations and the field line tracing of MAL. The comparison in Figure 3.8 between a Poincaré plot from MAL and flux contours shows good agreement between these two methods. Figure 3.9 shows the behavior of three sets of field lines propagated in the magnetic field that contains the $n = 5 - 8$ magnetic modes. The structure of the $n = 6$ island is evident from the motion of the field lines, but the field lines are able to cross the former $n = 6$ flux surfaces and move in and out

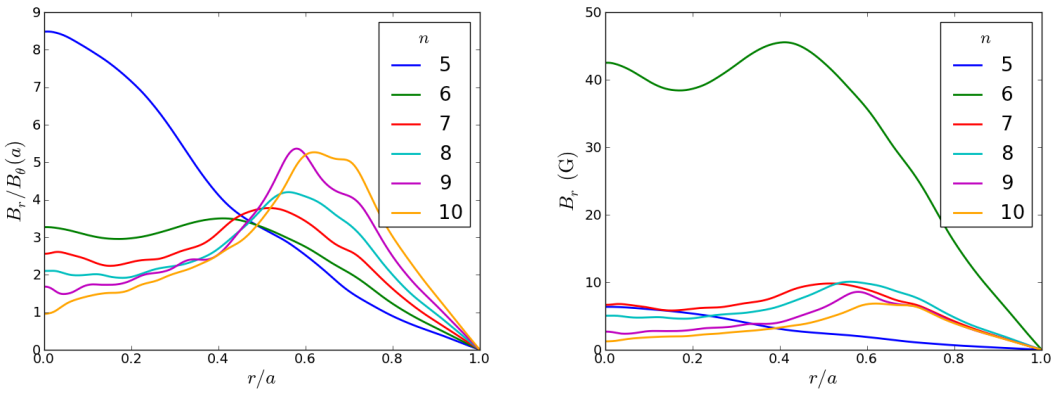

(a) **(b)**

Figure 3.7: (a) Magnetic mode profiles for several core tearing modes from ensembling of DEBS. The $n = 5$ mode has a qualitatively different profile because it is non-resonant. (b) The mode profiles are now each scaled to match the respective measured $B^n_\theta(a)$ amplitudes from MST. The $n = 6$ mode is by far the largest.

of the island at certain places. This indicates the presence of a homoclinic tangle, which is a chaotic structure resulting from a perturbed separatrix. Homoclinic tangles control where field lines exit the enclosed region [19]. Small regions of closed flux surfaces within the former island volume in Figure 3.9. These correspond to secondary islands which forms on the large $n = 6$ island due to the perturbation of the $n = 7$ mode, as illustrated in detail below.

The origin of the secondary islands can be demonstrated by removing all but the $n = 6, 7$ modes and reducing the $n = 7$ amplitude. This process, illustrated in Figure 3.10 reveals that the $n = 7$ mode forms two sets of islands. One lies on the (perturbed) toroidal flux surfaces outside the $n = 6$ separatrix. The other forms on closed flux surfaces within the $n = 6$ island. The $n = 6$ island flux surfaces can be considered as the equilibrium flux surfaces of a helical-axis stellarator that the $n = 7$ mode perturbs, creating islands with an effective poloidal periodicity of two. Increasing the $n = 7$ amplitude to the value obtained from MST causes the elliptical distortion of the core of the $n = 6$ island by the secondary

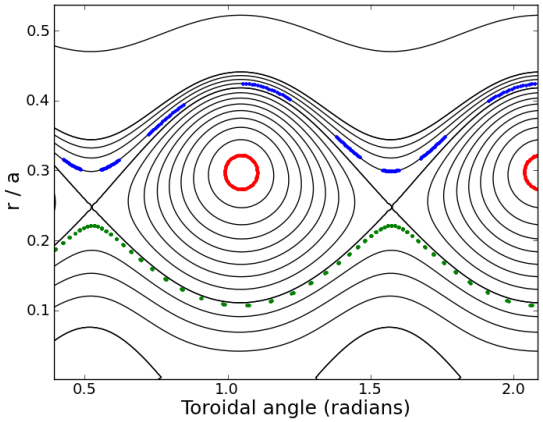

Figure 3.8: Three field lines (red, blue, green) follows the $n = 6$ flux surfaces (black) when only the $n = 6$ mode is present. Only one-third of the total toroidal angle is shown for clarity.

islands. This explains the elongated structure which is evident in the field lines launched near the $n = 6$ O-point in Figure 3.9.

Another way of visualizing the chaotic structure is to calculate the connection length of field lines from one region to another. The connection length is inversely related to the rapidity of transport between two regions along field lines. In this case, the connection length to the $n = 6$ separatrix was calculated for field lines starting inside the remnant $n = 6$ island. Figure 3.11 shows that the majority of connection lengths inside the island are greater than the mean free path (125 m) over a substantial portion of the interior, suggesting that thermal insulation from the separatrix is possible. On the other hand, the field lines with long and short connection lengths are mixed on small spatial scales, which could allow the short-connection-length field lines to dominate the heat loss given a small perpendicular conductivity. The connection length grows exponentially as one approaches the secondary islands, a phenomenon referred to as 'stickiness' [20].

This leads to the question of whether the disruption of the $n = 6$ island flux surfaces is

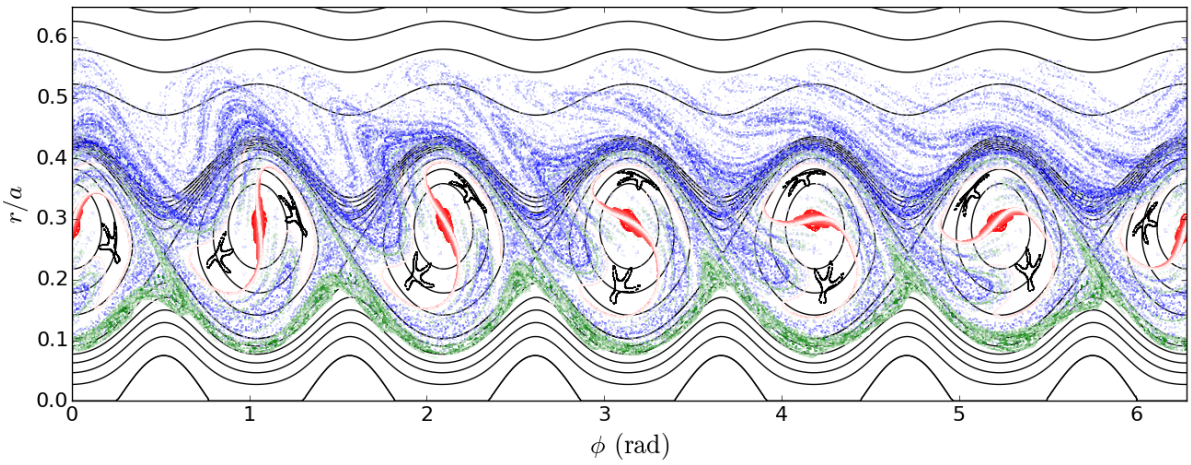

Figure 3.9: The set of points shown in Figure 3.8 were used to launch field lines of the same colors in the magnetic field with $n = 5 - 10$ modes included. The color of the field lines fades to white over 125 m in order to emphasize the localization of the field lines. The black points correspond to a field line launched at a single point on a flux surface of a small remnant 'secondary' island. This field line was followed for ≈ 10 km to fill out the flux surface, with no fading effect.

consistent with the observed temperature peaking. It is possible that transport along chaotic field lines would be so large as to prevent significant island heating (given the Ohmic heating power deposited inside the remnant island). The following section presents evidence that the chaos does not preclude the island heating.

One may also ask whether it is possible to identify substructure of the remnant island (such as the secondary islands or the transport barrier near the separatrix) from the TS temperature measurements, for comparison with the chaotic magnetic field structure. At this time, the limited quantity of data appears to preclude this, although future efforts should certainly be made to obtain more observations with good signal-to-noise ratio. At the time of the observation analyzed in this chapter, the magnetic mode rotation rates were such that the modes remained phase-locked together. This indicates that one should not expect to have seen the rotation of the secondary islands in the poloidal plane. This is consistent with the

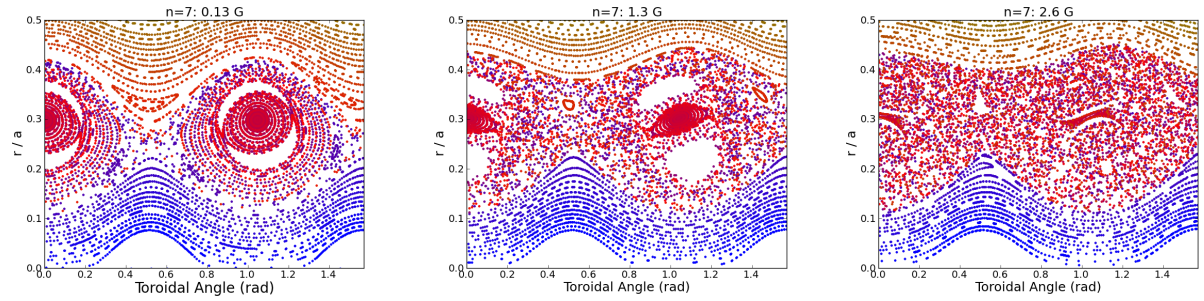

Figure 3.10: Scan of $n = 7$ mode amplitude with fixed $n = 6$ amplitude. Only one-quarter of the full toroidal angle is shown. The field lines are followed for 900 m. (a) With 0.05 times the MST $n = 7$ amplitude. (b) With 0.5 times the MST $n = 7$ amplitude. (c) With the MST $n = 7$ amplitude.

observed temperature structure, which does not exhibit such rotation.

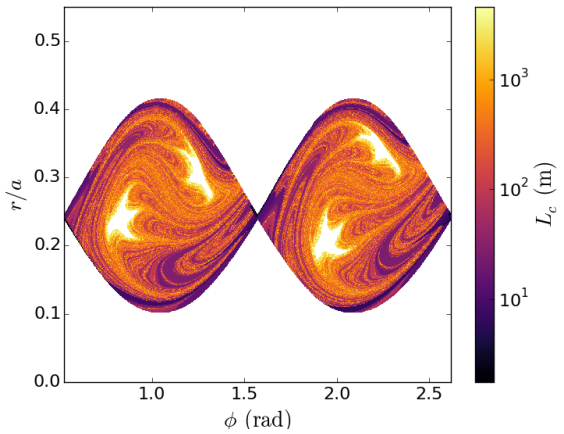

Figure 3.11: Connection lengths from island interior to separatrix. Only two periods were investigated to save time. The field lines were followed for a maximum of 50 km.

3.3.2 Field line spreading in flux coordinates

In order to quantify the degree to which chaos inside the remnant $n = 6$ island causes field lines to wander from their original flux surfaces, the field line trajectories can be mapped in terms of the flux coordinate of the $n = 6$ island. This will indicate the rate at which the field lines escape the island. A simple way of quantifying the rate of spreading of the field lines is to take the second moment of the distribution of the field line displacements, refered to here as the field line dispersion,

$$\sigma^2 \equiv \langle (\Delta\rho)^2 \rangle, \tag{3.23}$$

where $\Delta\rho(L) = \rho(L) - \rho(0)$ is the displacement of a field line from its starting position in terms of ρ, the effective radial coordinate of the island flux surfaces. Here $\rho(\psi) \equiv r_{\max}(\psi) - r_0$ is the effective radius of an island flux surface with flux value ψ as measured by the distance between the O-point at r_0 and the outer edge of the flux surface at r_{max}. This flux coordinate ρ thus has meaningful units of distance, as opposed to ψ, which does not.

The scaling of the dispersion σ^2 with field line length L is expected to be a power law [21, 22]. Diffusive spreading is characterized by $\sigma^2 \propto L^\alpha$ with $\alpha = 1$. The transport is said to be superdiffusive if $\alpha > 1$, or subdiffusive if $\alpha < 1$. Thus, the normalized dispersion $\frac{\sigma^2}{2L}$ will be a constant in the diffusive case. If the normalized dispersion asymptotes to a constant value, this is defined as the diffusion coefficient:

$$D_m \equiv \lim_{L\to\infty} \frac{\sigma^2}{2L}, \tag{3.24}$$

Even if the scaling is non-diffusive, the normalized dispersion $\frac{\sigma^2}{2L}$ can still be interpreted as a measure of the mean spreading rate of the field lines over a particular scale length.

Figure 3.12a shows the result of calculating $\frac{\sigma^2}{2L}$ for a set of 1000 field lines launched near the island O-point. The normalized dispersion increases approximately linearly with L, constituting superdiffusive field line motion. Superdiffusion indicates that the field lines remain correlated with their initial positions over a long distance. This long-distance correlation is also obvious from Figure 3.9. The roll-over of $\frac{\sigma^2}{2L}$ occurs because the field lines eventually reach the edge of the chaotic region and can go no further, so σ^2 approaches a constant, maximum value [23]. A more detailed view of the field line motion can be obtained from the distribution of field lines in ρ. Figure 3.12b shows that within 75 m the first field lines approach the separatrix, but then a barrier is encountered. This barrier is evident in Figure 3.9 as well, deflecting the field lines just inside the former separatrix of the $n = 6$ island.

The normalized dispersion is dependent on the initial value of ρ (that is, on how far from the island axis the field lines are launched). This is a consequence of the superdiffusive nature of the field line trajectories. However, the label 'superdiffusive' refers only to the scaling of the field line transport. The magnitude of the transport may actually be smaller than the properly-diffusive field line transport that occurs in the thoroughly stochastic magnetic

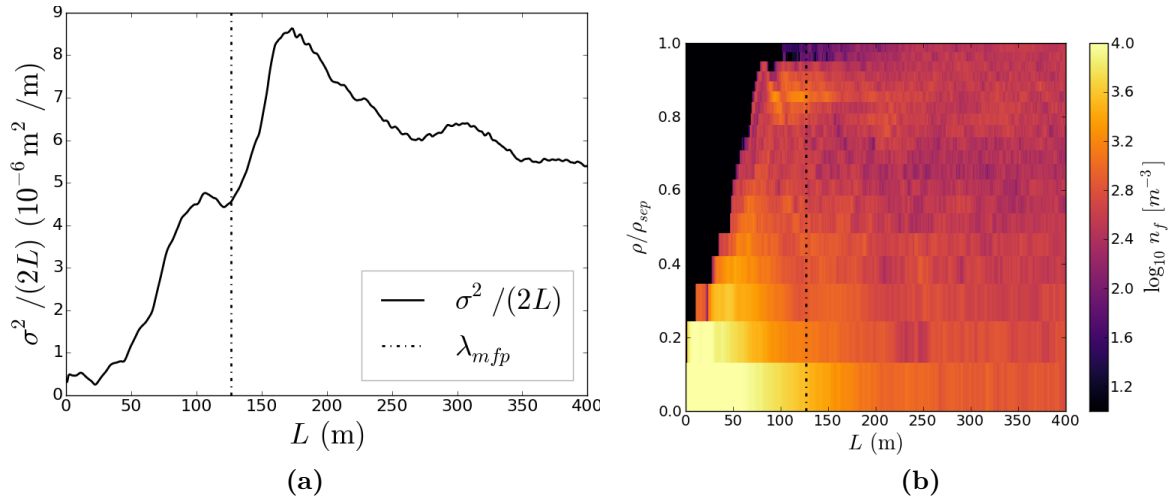

Figure 3.12: (a) Magnetic field line normalized dispersion $\sigma^2/2L$ as a function of field line length L. The electron mean free path is marked. (b) The distribution of magnetic field line endpoints over the island radial coordinate ρ as a number density n_f, plotted for different values of L. For both plots, the rescaled $n = 5$ to 10 modes are used.

fields found at larger radius.

3.3.3 Estimate of electron thermal transport due to magnetic chaos

Only magnetic field line transport has been considered so far. The electron transport is not identical to the field line transport, as electrons undergo collisions such that they may speed up, slow down, or reverse course along the field line. Collisions also cause electrons to be displaced from one field line to another. The relevant length and time scales are the electron mean free path $\lambda_{mfp} = v_{th,e}/\nu_{ei}$ and the electron-ion collision frequency ν_{ei}, where $v_{th,e}$ is the electron thermal velocity. (For these plasma conditions, electron-ion collisions are the dominant collisional process affecting electrons. The collisional mean free path is calculated from the Braginskii formula [24, p.430].) After traveling for one mean free path, the electron velocity becomes decorrelated from its initial value. This suggests that the maximum length

at which the magnetic field line spreading is relevant is the mean free path. For this reason, the normalized dispersion is evaluated at the mean free path length, yielding a value of $\frac{\sigma^2}{2L} \approx 4.5 \times 10^{-6}\mathrm{m}^2/\mathrm{s}$. This is comparable to the value for D_m found by Hudson [5, fig. 3.13] in the outer region in improved-confinement plasmas.

In order to convert the magnetic field line spreading as a function of distance into an electron thermal conductivity, the electron velocity is used to convert from field line length to time: $\chi_{e,m} \propto v_{th,e}\left(\frac{\sigma^2}{2L}\right)$. One additional effect to consider is electron trapping due to the mirror effect [24, p.39]. A fraction of electrons are prevented from completing a full poloidal circuit along a field line because the magnitude of the field increases on the inboard side of the plasma. MSTFIT estimates that for the equilibrium field, the passing fraction f_p of electrons is about 60%. A similar value may be estimated from [25, fig. 4], where trapped-passing particle collisions are accounted for. (For the island, the inverse aspect ratio is $\epsilon \approx 0.1$. The ratio L_T/λ_{mfp} is about 10^0 to 10^2, where L_T is the temperature gradient length scale estimated from the connection length and the island temperature.) Incorporating the effect of trapping was shown to improve agreement between the estimates of $\chi_{e,m}$ and $\chi_{e,th}$ in the stochastic region of MST, where the form $\chi_{e,m} = f_p v_{th,e} D_m$ was used for the chaotic conductivity [11].

The final form of the estimate of the electron thermal conductivity in this case is thus:

$$\chi_{e,m} = f_p v_{th,e}\left(\frac{\sigma^2}{2\lambda_{mfp}}\right), \tag{3.25}$$

where σ^2 is evaluated at $L = \lambda_{mfp}$. This is the equation used to evaluate the estimated thermal conductivity for electrons launched at the center of the remnant island structure. For 350 eV electrons, the thermal velocity is $v_{th,e} = 1.1\times10^7\mathrm{m}^2/\mathrm{s}$. This results in a value of $\chi_{e,m} \approx 30\,\mathrm{m}^2/\mathrm{s}$. This is far lower than the equivalent value computed for the stochastic diffusion in

the outer region, which has conductivity as large as $\chi_{e,m} \approx \chi_{e,th} \approx 500 - 1000\,\mathrm{m}^2/\mathrm{s}$, but it is comparable to the conductivity in the outer region during improved confinement discharges [6, 11, 13, 26].

There are several caveats to this estimation of the chaos-induced transport. First, the assumption of a Gaussian distribution for the magnetic field lines does not hold here due to the complicated magnetic field structure. Thus, the growth rate of the second moment σ of the field line distribution does not completely characterize the spreading rate of the magnetic field lines, as is assumed in the ideal picture of Brownian motion. Second, there may exist correlations between the magnetic field lines and the electrons that are not captured by simply evaluating the mean spread of the field lines at the mean distance traveled by electrons during a collision period. Such correlations could alter the resulting transport. In order to do justice to the complexity of the situation, it would be desirable to perform a 3D simulation using a kinetic treatment (such as drift-kinetics). This is beyond the scope of the present work, however. The electron thermal transport estimate presented here is intended as a plausible estimate that combines magnetic field line spreading with collisional decorrelation of electrons from field lines.

3.3.4 Comparison with thermal transport

The final step is to estimate the effective thermal conductivity in the direction perpendicular to the original $n = 6$ flux surfaces based on the observed temperature peaking. This provides the counterpart to the estimate of thermal transport due to field line diffusion across the $n = 6$ flux surfaces. As a reminder, this is not to say that the $n = 6$ flux surfaces are preserved in the plasma. The flux merely provides a convenient local coordinate to use when estimating the transport. Several simplifying assumptions are made for this calculation.

Variations in temperature along the flux surfaces are smaller than variations between flux surfaces, so it is reasonable to approximate the temperature as constant on a flux surface. This reduces the problem from two dimensions (r, ζ) to one (ψ). The Ohmic heating power density ηJ^2 and electron density n_e are also approximated as constant. The electron thermal conductivity $\chi_{e,th}$ is assumed to be a function of the flux. The temperature is assumed to be steady-state.

Starting with the continuity equation for thermal energy density W and the definition of the diffusive heat flux $\mathbf{Q}$,

$$-\nabla \cdot \mathbf{Q} + \eta J^2 = \frac{dW}{dt} = 0 \tag{3.26}$$

$$\mathbf{Q} = n_e \chi_{e,th} \nabla T_e \tag{3.27}$$

integration over the volume enclosed within a flux surface leads to:

$$V \eta J^2 = n_e \chi_{e,th} \frac{\partial T_e}{\partial \psi} \int \nabla \psi \cdot d\mathbf{A} \tag{3.28}$$

$$\eta J^2 = n_e \chi_{e,th} \langle T_e^{'} \rangle (A/V) \tag{3.29}$$

$$\langle T_e^{'} \rangle = \frac{\partial T_e}{\partial \psi} \int \nabla \psi \cdot d\mathbf{A}, \tag{3.30}$$

where V and A are the enclosed volume and surface area of the flux surface. (Note that V is the total volume within the flux surface, not the differential volume between surfaces.) The geometry of the flux surfaces is distilled to the ratio A/V and the integral $\int \nabla \psi \cdot d\mathbf{A}$, leaving an algebraic problem of solving for either the effective conductivity $\chi_{e,th}$ or the temperature gradient $\langle T_e^{'} \rangle$ in terms of the other constants and functions of flux. In this case, $\chi_{e,th}$ is specified, and the temperature as a function of flux can be found and compared to the

observations. (If the temperature is mapped back to (r, ζ) coordinates, one can compute the fluctuation profiles as well.)

The temperature measurement points from Figure 3.5 are mapped from (r, ζ) coordinates to

$$\Psi \equiv (\psi(r, \zeta) - \psi_{O-point}) \,/\, (\psi_{separatrix} - \psi_{O-point}) \tag{3.31}$$

in Figure 3.13. This coordinate is convenient since it is proportional to flux surface volume rather than radius, which makes the temperature profiles approximately linear rather than parabolic. The geometric integrals over the flux surfaces are computed numerically for the $n = 6$ flux surfaces. Figure 3.13 also shows the modeled temperature profiles based on assuming constant conductivity in the island ($\chi_{e,th} = 20\,\mathrm{m}^2/\mathrm{s}$), outer region ($\chi_{e,th} = 400\,\mathrm{m}^2/\mathrm{s}$), and core ($\chi_{e,th} = 3\,\mathrm{m}^2/\mathrm{s}$). The boundary condition for integrating $\frac{\partial T_e}{\partial \psi}$ in each region was the specification of the temperature at the separatrix $T_{sep} = 250\,\mathrm{eV}$. The conductivities and T_{sep} were selected manually. The uncertainty range in the island conductivity is $\chi_{e,th} = 10 - 40\,\mathrm{m}^2/\mathrm{s}$. Most of the uncertainty is from estimation of the temperature gradient and the Ohmic power density. This result is in agreement with the estimated magnetic-chaos-induced conductivity $\chi_{e,m} \approx 30\,\mathrm{m}^2/\mathrm{s}$ found in the previous section. This suggests that the chaos-induced transport is sufficiently small in this case to allow the existence of an Ohmically-heated temperature peak inside the remnant island structure.

3.3.5 Other possible observations

Four other possible hot island observations were obtained in the discharges just before or after discharge 1140726089. These examples had lower plasma density with correspondingly large errors in the Thomson scattering measurements of T_e. Only a preliminary analysis

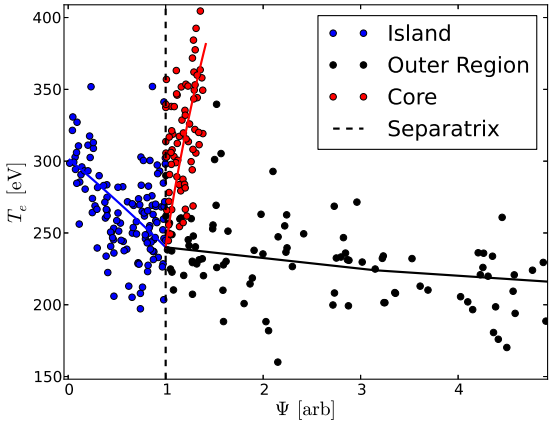

Figure 3.13: T_e as a function of flux for the island interior (blue, left of separatrix) and the outer region (black, right of separatrix). The core, shown in red, is degenerate in flux value with the outer region because the flux is not single-valued since it has a minimum at the island. The solid lines are the solution to the thermal equation with the constant values of conductivity in each region: core $\chi_{e,th} = 3\,\mathrm{m}^2/\mathrm{s}$; island $\chi_{e,th} = 20\,\mathrm{m}^2/\mathrm{s}$; outer region $\chi_{e,th} = 400\,\mathrm{m}^2/\mathrm{s}$

was conducted. Of the four other possible hot island observations in hand, all had a simpler structure according to preliminary Poincaré plots. Some volume of closed $n = 6$ magnetic surfaces remained at the O-point in each case, surrounded by chaos. However, the existence of these observations does suggest that island heating is relatively common, in agreement with the ensemble analysis. A hot island was observed not to occur in one case where a large $n = 6$ mode was completely chaotic with no closed surfaces remaining at all.

References

[1] G. E. P. Box and N. R. Draper, *Emperical model-building and response surfaces* (John Wiley & Sons, New York, 1987) p. 74.

[2] W. C. Young, L. A. Morton, E. Parke, and D. J. Den Hartog, Journal of Instrumentation

8, C11013 (2013).

[3] W. C. Young and D. J. Den Hartog, Journal of Instrumentation **10**, C12021 (2015).

[4] D. J. Den Hartog and W. C. Young, Journal of Instrumentation **10**, C12008 (2015).

[5] B. F. Hudson, *Fast Ion Confinement in The Reversed-Field Pinch*, Phd thesis, University of Wisconsin (2006).

[6] T. M. Biewer, C. B. Forest, J. K. Anderson, G. Fiksel, B. Hudson, S. C. Prager, J. S. Sarff, J. C. Wright, D. L. Brower, W. X. Ding, and S. D. Terry, Physical Review Letters **91**, 045004 (2003).

[7] J. K. Anderson, C. B. Forest, T. M. Biewer, J. S. Sarff, and J. C. Wright, Nuclear Fusion **44**, 162 (2004).

[8] E. Parke, J. K. Anderson, D. L. Brower, D. J. Den Hartog, W. X. Ding, C. A. Johnson, and L. Lin, Physics of Plasmas **23**, 056108 (2016).

[9] E. Parke, *Diagnosis of Equilibrium Magnetic Profiles, Current Transport, and Internal Structures in a Reversed-Field Pinch Using Electron Temperature Fluctuations*, Phd thesis, University of Wisconsin - Madison (2014).

[10] D. D. Schnack, D. C. Barnes, Z. Mikic, D. S. Harned, and E. J. Caramana, J. Comp. Phys. **70**, 330 (1987).

[11] J. A. Reusch, J. K. Anderson, D. J. Den Hartog, F. Ebrahimi, D. D. Schnack, H. D. Stephens, and C. B. Forest, Physical Review Letters **107**, 155002 (2011).

[12] J. R. King, C. R. Sovinec, and V. V. Mirnov, Physics of Plasmas **18**, 042303 (2011).

[13] J. A. Reusch, *Measured and Simulated Electron Thermal Transport in the Madison Symmetric Torus Reversed Field Pinch*, Phd thesis, University of Wisconsin - Madison (2011).

[14] J. W. Edenstrasser, Journal of Plasma Physics **24**, 299 (1980).

[15] J. W. Edenstrasser, Journal of Plasma Physics **24**, 515 (1980).

[16] D. Biskamp, *Nonlinear Magnetohydrodynamics* (Cambridge University Press, 1993).

[17] J. Sauppe, *Extended Magnetohydrodynamic Modeling of Plasma Relaxation Dynamics in the Reversed-Field Pinch*, Phd thesis, University of Wisconsin - Madison (2015).

[18] R. Fitzpatrick, Physics of Plasmas **2**, 825 (1995).

[19] T. E. Evans, R. K. W. Roeder, J. A. Carter, B. I. Rapoport, M. E. Fenstermacher, and C. J. Lasnier, Journal of Physics: Conference Series **7**, 174 (2005).

[20] G. Contopoulos and M. Harsoula, Celestial Mechanics and Dynamical Astronomy **107**, 77 (2010).

[21] A. K. Ram, B. Dasgupta, V. Krishnamurthy, and D. Mitra, Physics of Plasmas **21**, 072309 (2014).

[22] D. Perrone, R. O. Dendy, I. Furno, R. Sanchez, G. Zimbardo, A. Bovet, A. Fasoli, K. Gustafson, S. Perri, P. Ricci, and F. Valentini, Space Science Reviews **178**, 233 (2013).

[23] F. D'Angelo and R. Paccagnella, Phys. Plasmas **3**, 2353 (1996).

[24] D. A. Gurnett and A. Bhattacharjee, *Introduction to Plasma Physics* (Cambridge University Press, 2005).

[25] E. D. Held, J. D. Callen, C. C. Hegna, and C. R. Sovinec, Physics of Plasmas **8**, 1171 (2001).

[26] J. K. Anderson, J. Adney, A. Almagri, A. Blair, D. L. Brower, M. Cengher, B. E. Chapman, S. Choi, D. Craig, D. R. Demers, D. J. Den Hartog, B. Deng, W. X. Ding,

F. Ebrahimi, D. Ennis, G. Fiksel, C. B. Forest, P. Franz, J. Goetz, R. W. Harvey, D. Holly, G. T. A. Huijsmans, M. Kaufman, T. Lovell, L. Marrelli, P. Martin, K. McCollam, V. V. Mirnov, P. Nonn, R. O'Connell, S. Oliva, P. Piovesan, S. C. Prager, I. Predebon, J. S. Sarff, G. Spizzo, V. Svidzinski, M. Thomas, and M. D. Wyman, Physics of Plasmas **12**, 056118 (2005).

4 Turbulence modification by a large static island in the DIII-D tokamak

> *But physicists are, at bottom, a naive breed, forever trying to come to terms with the 'world out there' by methods which, however imaginative and refined, involve in essence the same element of direct contact as a well-placed kick.*
>
> — Bryce S. Dewitt and R. Neill Graham, *Resource Letter IQM-1 on the Interpretation of Quantum Mechanics [1]*

The behavior of turbulence and transport in the vicinity of a magnetic island is an interesting and important topic. Externally-induced magnetic islands are used to modify transport in the plasma edge in island divertor scenarios [2] and in resonant magnetic perturbation (RMP) suppression [3] of edge-localized modes (ELMs). In a recent experiment on DIII-D, a large static $m = 2$, $n = 1$ island was induced by an externally-applied resonant magnetic perturbation (RMP). The beam emission spectroscopy (BES) diagnostic was used to measure density fluctuations resulting from drift wave turbulence in two dimensions around the island, with high spatial resolution.

Although the analysis of the data is on-going, preliminary results presented in this chapter show that there is significant modulation of the turbulence in the vicinity of the island.

As expected, the turbulence is reduced inside the O-point and increased near the X-point, since the island is wider than the turbulence correlation length. Unexpectedly, the enhanced turbulence appears to occur inboard from the rational surface as judged from the island T_e contours. When the RMP is applied but does not produce an island due to plasma rotation, the turbulence response smaller and less radially-localized.

4.1 Background

The experiment described in this chapter was prompted by earlier experiments on DIII-D that showed evidence of a spontaneous transition in the thermal response of large static islands to heat pulses propagating outward from the interior of the plasma past the islands. The heat pulses initially penetrated the island, demonstrating transport from the exterior to the interior. Then a transition occurred, after which the effect inside the island of the heat pulses was attenuated and delayed. The transition in heat-pulse response was hypothesized to result from reduction of chaos or from expulsion of turbulence [4].

The present experiment was designed to reproduce the conditions favorable to the observation of this transition in island thermal response. Density fluctuation diagnostics were recruited to probe the response of turbulence to the presence of the island and to the transition in island thermal response. This chapter focuses on the results obtained using the BES diagnostic, which is sensitive to density fluctuations on the ion scale. The results presented here are a characterization of the turbulence in two dimensions around the island. Density turbulence in discharges without islands has already been well-characterized in DIII-D using the BES diagnostic [5].

There are several potential mechanisms by which a magnetic island could influence turbu-

lence. Drift wave stability is influenced by the steepness of the driving gradients and the topology of the equilibrium magnetic field, among many other things [6]. Flow shear is also able to suppress drift wave turbulence and transport [7]. Magnetic islands modify the topology of flux surfaces, the density and temperature gradients, and possibly flow shear as well. This leads naturally to the consideration of how magnetic islands impact turbulence.

Gradient modifications by a magnetic island lead to the expectation of enhanced turbulence intensity at the X-point of a magnetic island and reduced intensity at the O-point, with respect to turbulence in the absence of an island [8, 9]. The turbulence may not be poloidally symmetric about the X-point, however [9, 10, 11]. Turbulence spreading could reintroduce transport and gradients inside the island if the island width is not much larger than the turbulence correlation length [10, 12].

The magnetic topology of an island could directly modify drift wave linear stability according to gyrokinetic simulations [13]. Even small magnetic perturbations can increase the level of turbulence by disrupting zonal flows which otherwise keep the turbulence level in check [14, 15]. There is already experimental evidence from DIII-D that magnetic perturbations directly act to increase turbulence, bypassing the mechanism of changing the gradients which drive the turbulence [16].

In the LHD [17] and TJ-II [18] stellarators it has been shown that large static magnetic islands modify the poloidal $\mathbf{E} \times \mathbf{B}$ velocity, which could have an effect on turbulence and transport. In the JT-60U tokamak improved ion thermal confinement has been measured inside a static island, attributed to flow shear suppression of turbulence [19]. Recent probe measurements in the J-TEXT tokamak conducted at a single toroidal phase of an island have shown a 30% reduction of turbulence inside the island, along with modifications to flows [20]. Recent results from DIII-D with a rotating neoclassical tearing mode island also

show suppression of turbulence by 14% across the island [21, 22]. A full two-dimensional mapping of turbulence, flows and correlations around a large static island has so far been lacking, however.

4.2 Experimental configuration

The flux surface shape in DIII-D for the present experiment is shown in Figure 4.1a. Although DIII-D is often operated with a divertor, in this experiment the plasma was limited on the inner wall (a simpler plasma topology from the standpoint of modeling). The plasma current was 1.3 MA. The toroidal field strength at the magnetic axis was 1.96 T. The q-profile is shown in Figure 4.1b. The lowest-order resonances are those with periodicity $m, n = m, 1$ with $m = 1$ to 4. The plasma electron density and temperature were about $3.5 \times 10^{13}\,\mathrm{cm}^{-3}$ and 1.3 keV respectively.

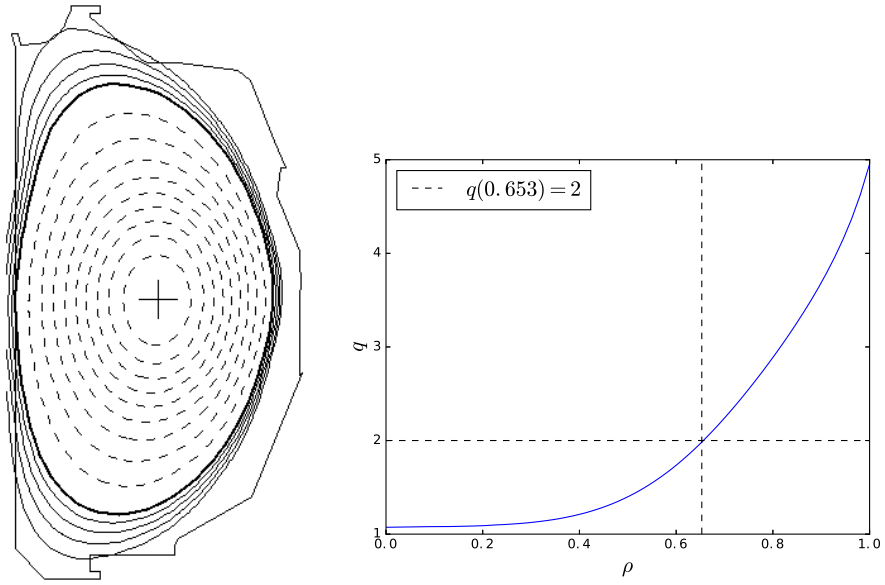

Figure 4.1: (a) DIII-D flux surfaces and (b) DIII-D q-profile in terms of minor radius ρ, both from discharge 165210.

Neutral beam injection and electron cyclotron resonance heating were both employed, driven by diagnostic considerations rather than by plasma sustainment requirements. The total injected power was in fact limited to 3 MW in this experiment in order to avoid the transition from L-mode into H-mode. H-mode discharges exhibit ELMs, which would complicate fluctuation diagnostic analysis. H-mode plasmas are also easily disrupted by large magnetic islands.

Of the total power injected, 1.5 MW was injected as electron cyclotron resonance heating (ECH). The ECH system was run at a 50% duty cycle at 40 or 50 Hz, so the injected power was square-wave modulated from about 0 to 3 MW. This produced heat pulses for studying the island thermal transport. The ECH absorption location was closer to the core of the plasma than the $q = 2$ surface, so that the heat pulses propagated outward past the $m = 2$ island.

The remaining 1.5 MW of power was injected by a set of neutral beams. The neutrals beams also serve as probes of the plasma, forming the basis for both the BES and motional Stark effect (MSE) diagnostics. The MSE diagnostic measures the local magnetic field line pitch, allowing the q-profile to be determined more accurately than is possible from reconstructions with only external magnetic measurements [23]. This capability was desired in order to locate the resonant surface of the magnetic islands. The BES diagnostic was one of the primary turbulence diagnostics. However, the MSE and BES diagnostics do not use the same beam. Both beams could not be used simultaneously due to the restrictions on the injected power. Thus the MSE diagnostic was used for a small number of reference discharges, while the BES diagnostic was used instead during the majority of discharges in the experiment.

Because the neutral beams enter the plasma tangentially, they impart toroidal angular momentum (or equivalently, impose a torque on the plasma). The net neutral beam torque was

limited to $< 0.2\,\mathrm{N}\cdot\mathrm{m}$ to keep the plasma rotation sufficiently low. If the rotation is too high, the RMP is 'screened' by the plasma, preventing the island from forming [24]. One neutral beam is directed opposite to the other three on DIII-D, allowing it to cancel some of the torque from the others. By reducing the beam velocities to reduce input power and using the reversed beam to reduce the net torque, the rotation and power limits were satisfied while still allowing the beam-based diagnostics to function.

The RMP which triggers the island formation is produced by external coils. There are six such coils (called C-coils [25]) arranged toroidally around the equatorial plane of the torus as shown in Figure 4.2. The coils are linked in opposing pairs, allowing $n = 1$ perturbations to be applied with arbitrary phasing. The position of the induced $n = 1$, $m = 2$ island can be rotated to ensure good sampling by the diagnostics. Previous experiments had demonstrated the use of π phase flips to allow temperature diagnostics (electron cyclotron emission [26] and soft X-ray emission [27]) to view the X-point and O-point of the island [24]. Without the RMP, no island forms.

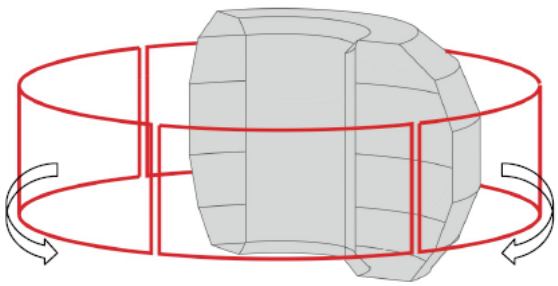

Figure 4.2: Schematic view of the C-coil locations with respect to the DIII-D vessel. Courtesy of Dr. M. W. Shafer.

In this experiment the phase of the applied $n = 1$ perturbation was changed in two different patterns. The first pattern consisted of a set of 16 discrete steps which were carried out over

two sequential discharges. The second pattern was a 4π continuous rotation conducted during a single discharge. The discrete steps allowed the plasma to settle into a stationary state so that the diagnostics could acquire good statistics about the fluctuations. The continuous rotations, on the other hand, ensured total phase coverage using only a single discharge.

4.2.1 Beam emission spectroscopy

The beam emission spectroscopy (BES) diagnostic is capable of resolving fluctuations with spatial scales on the order of one centimeter, which is the appropriate scale length to observe ion-scale drift waves in DIII-D [28]. BES relies on excitation of injected neutral deuterium atoms by collisions with plasma electrons. The excited states decay rapidly, emitting photons. The collisional excitation rate depends on plasma density, so the photon emission is proportional to the local density. The transition wavelength (in this case, the Balmer D_α line) is Doppler-shifted due to the beam velocity, which allows the beam emission to be separated from the background emission occurring at the plasma edge. The density fluctuations rotate with the plasma, giving rise to a frequency $f = v/\lambda$ where v is the velocity of the fluctuation and λ is the wavelength [5]. The diagnostic can measure up to 400 kHz [29].

The frequency spectra of fluctuations are directly available from the single-point measurements of the density. Finding the wavelength spectrum requires combining measurements from two or more spatial points. Correlating poloidally separated measurement points allows one to determine the phase delay (or time delay) between the two points, yielding the turbulence poloidal velocity. The turbulence poloidal and correlation length can also be obtained in this manner. Correlating two poloidally-adjacent channels helps reject photonic and electronic noise [29].

Correlation methods do not, however, remove spurious fluctuations caused by modulation of

the beam itself. Beam modulations can arise from fluctuations in the injector or from varying beam absorption caused by fluctuations of the plasma edge density. The beam modulations occur at lower frequencies, setting the low-frequency limit on the diagnostic sensitivity to about 20 kHz [29]. In this chapter, unless otherwise noted, the spectral crosspower and the turbulence intensity derived from it are produced by nearest-neighbor poloidal correlation. The turbulence intensity is taken by integrating the fluctuations between 25-150 kHz, and is normalized to the mean signal, to produce a relative fluctuation in intensity $\delta I/\langle I\rangle$.

The BES system has 64 measurement locations which can be distributed in a two-dimensional array [30]. For this experiment, the array was arranged with a 7×8 rectangular grid with spacing about one centimeter in both radial and poloidal directions, and two 4-channel 'wings' providing extra radial coverage. The location of the array in the overall cross-section of the plasma is shown in Figure 4.3a. The flux surfaces of the equilibrium field from DIII-D discharge 165210 (which had no applied RMP) are shown. This reconstruction using EFIT [31] incorporated MSE measurements, so rational surfaces are also shown. The array was targeted at the resonant location of the $m, n = 2, 1$ island.

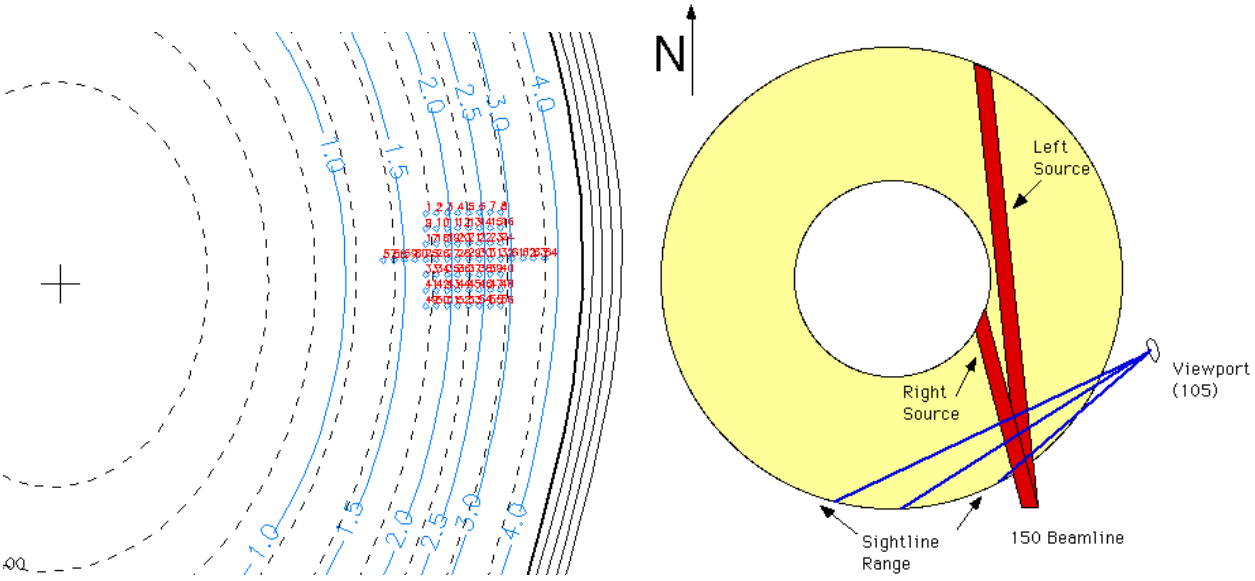

(a) (b)

Figure 4.3: (a) Flux surfaces and q rational contours in a poloidal plane from EFIT with MSE diagnosis on discharge 165210 (the first reference discharge with MSE). The BES array location is marked. (b) Top view of the BES diagnostic geometry. Courtesy of Dr. G. R. McKee.

4.2.2 Island location

Field line tracing using the TRIP3D code [32] was performed by Dr. M. W. Shafer using the target discharge (154921) from the previous experiment. The equilibrium fields were used, with the RMP fields (as calculated in the absence of a plasma) superimposed. The q-profile of this discharge was not the same as in the reference discharge for the present experiment, so the island radial locations are not identical, but the poloidal locations should be valid. Poincaré plots were produced in the poloidal plane at $\phi = 145°$ (the approximate toroidal location of the BES measurement volumes), providing a preliminary expectation for the diagnostic's view of the islands. Figure 4.4 shows that with a C-coil phase of 55°, the X-point of the $m, n = 2, 1$ magnetic island would lie at the outboard mid-plane ($\theta = 0$),

the approximate BES poloidal location. In actuality, the plasma response may introduce a phase shift. Neither the edge magnetic response nor the electron temperature structure has yet been analyzed to detect this shift, however.

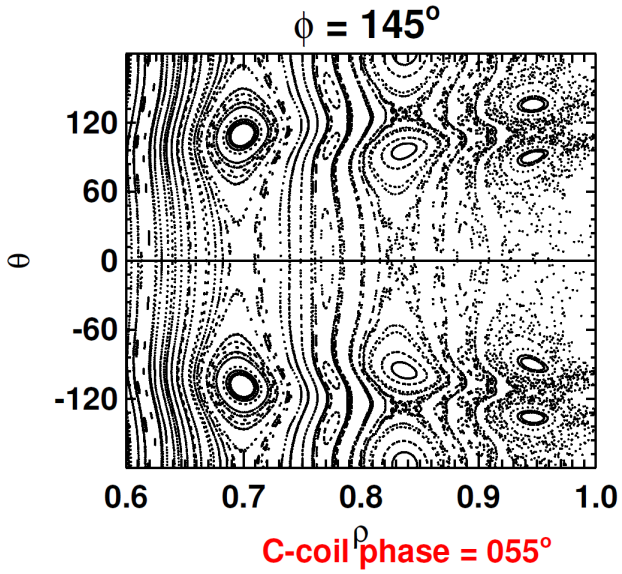

Figure 4.4: TRIP3D Poincaré plot based on discharge 154921 (the reference discharge from the previous experiment) with the C-coil RMP phase such that the X-point of the $m, n = 2, 1$ island is at the outboard midplane at the toroidal location of the BES diagnostic. The q-profile of this discharge differs from the q-profile of the reference discharge for the present experiment (165210), so the island radial locations are not informative. Courtesy of Dr. M. W. Shafer.

The presence of a large island ($\approx$ 8 cm wide) is confirmed by the ECE diagnostic, which measures a heated island structure in the electron temperature (Figure 4.5). The island is much larger than the critical width $w_c \sim 10\rho_i \sim 2\,\text{cm}$ for turbulence spreading [12]. (Here ρ_i is the ion gyroradius.) Thus, we would expect the turbulence to be excluded from the O-point of the island, assuming that the gradients driving the turbulence are reduced within the island.

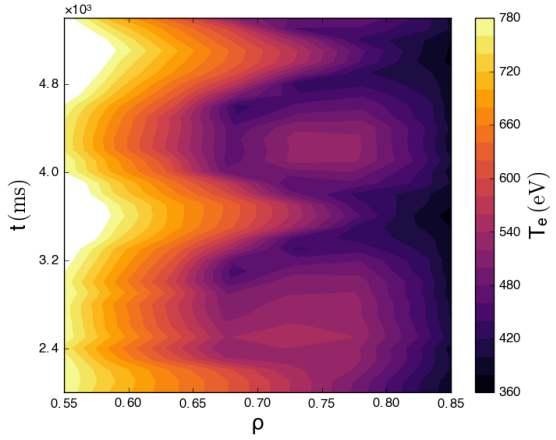

Figure 4.5: The electron temperature from ECE showing the location of the induced island during a rotational scan. Produced using OMFITprofiles [33].

4.3 Density fluctuation results

The spectrum of density fluctuations is dramatically altered by the presence and position of a magnetic island in the BES field-of-view. Figure 4.6 compares the turbulent crosspower spectra for two opposite phases of the $n = 1$ RMP against the turbulence in the absence of the RMP. The radial location $\rho = 0.65$ of the predicted rational surface location was chosen to emphasize the effect. The RMP phase of 10° brings the X-point nearer the BES measurement location than does the 205° phase. The turbulence is seen to be enhanced near the X-point and reduced near the O-point, as expected for an island larger than the turbulence correlation length. The crosspower is increased or decreased several-fold from the baseline presented by the no-RMP case in discharge 165210.

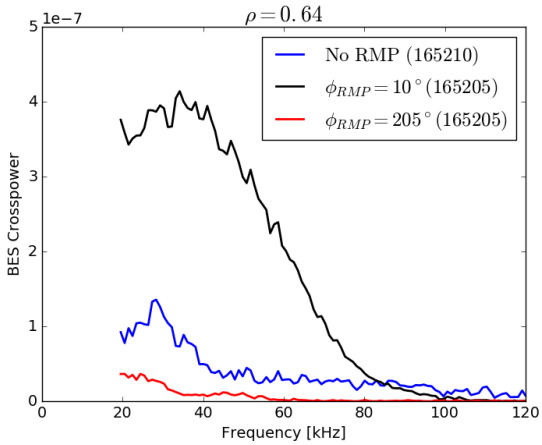

Figure 4.6: The BES crosspower spectra for the no-RMP case and two phases of the RMP.

Exploring the radial dependence of the spectrum in Figure 4.7 shows that the turbulence is markedly different near the X-point ($\phi_{RMP} = 10°$). There is a strong radial dependence, with larger turbulence crosspower at $\rho < 0.67$. The radial dependence of the turbulence in the no-RMP case is far less pronounced. The turbulence is reduced across all radii near the O-point ($\phi_{RMP} = 205°$).

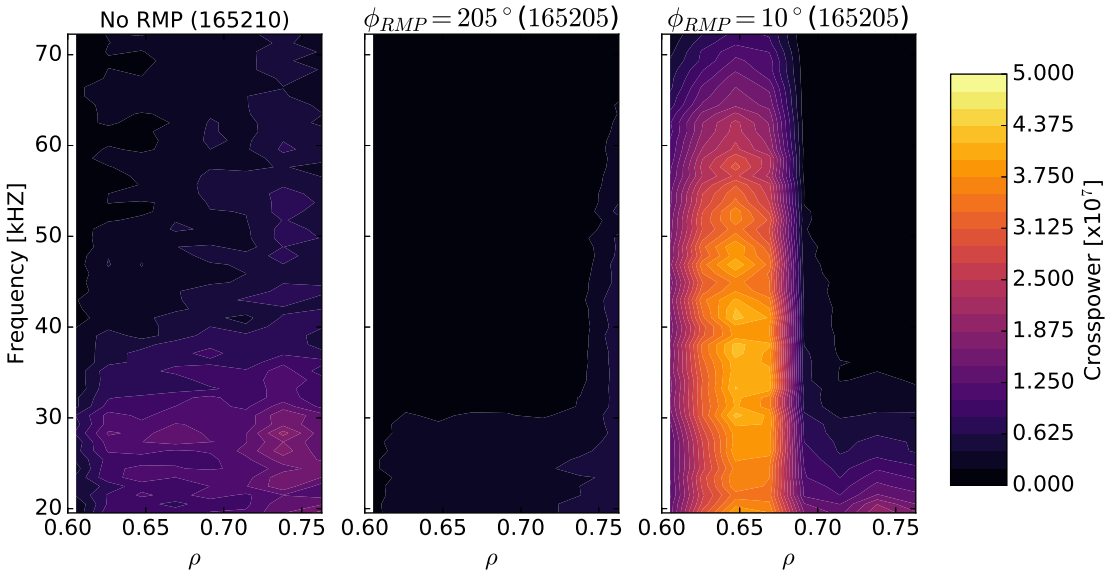

Figure 4.7: BES crosspower as a function of frequency and ρ in three cases. The color scales are the same for each plot.

A two-dimensional spatial picture of the turbulence intensity in terms of ρ and RMP phase can also be obtained. Figure 4.8a is made using discrete time bins from a continuous rotation. The fluctuation intensity is maximized near $\phi_{RMP} = 0 - 50°$. This is close to, but somewhat offset from, the expected phase for which the X-point would be present at the BES location ($\phi_{RMP} = 55°$). As noted in Section 4.1, a phase shift of the turbulence intensification away from the X-point would not be unexpected based on theory and simulations.

The radial location of the turbulence enhancement near the X-point appears to be located inboard of the X-point radius. In Figure 4.8a, the outermost radial point with significant turbulence enhancement is at $\rho \approx 0.65$. However, referring to Figure 4.5 shows that center of the electron temperature hot spot is near $\rho = 0.75$. An explanation for both the radial and poloidal offsets awaits further modeling to determine the precise location and shape of the magnetic island, as well as the expected turbulence response based on the observed island shape and measured gradients.

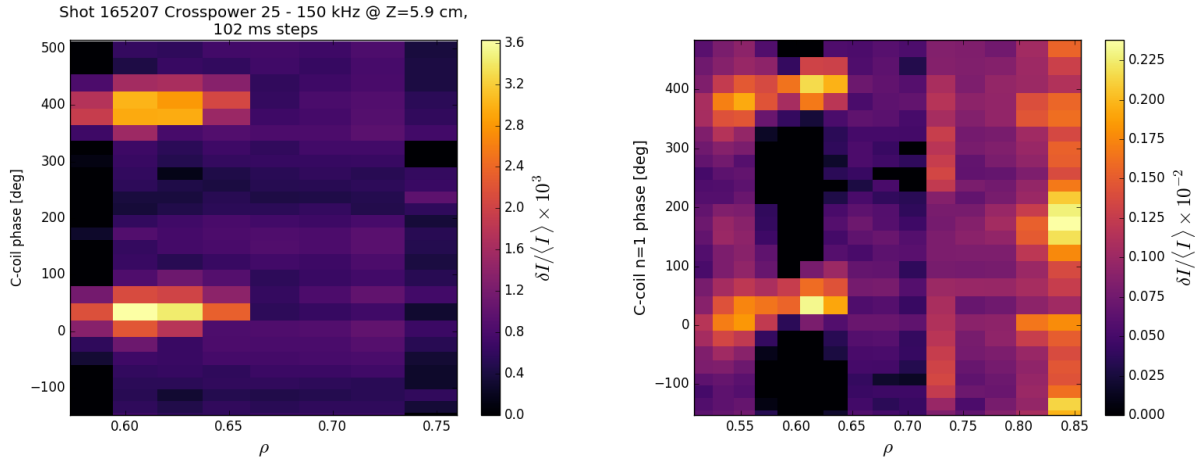

(a) **(b)**

Figure 4.8: (a) Relative fluctuation intensity as function of radius ρ and RMP phase. The center of the rectangular regions corresponds to the mean phase and radius of the measurement. (b) Extended radial view of the turbulence using radial cross-correlations (rather than poloidal ones) to take advantage of the BES array 'wings.'

In order to get a broader view of the turbulence around the island region, the 'wings' of the BES array can be included (Figure 4.8b). This requires the use of radial (rather than poloidal) nearest-neighbor correlations, so the results are not strictly comparable to the other values in this chapter. Nonetheless, the picture is quite similar to Figure 4.8a. Interestingly, the turbulence concentration near the X-point has a slight tilt that is less apparent in the narrower radial view of Figure 4.8a. The tilt might be due to turbulence advection in a sheared poloidal flow. Determination of the turbulence poloidal velocity from the BES data is a high priority for further analysis.

In DIII-D discharge 165204, the torque limit for production of the $m, n = 2, 1$ island was exceeded, so the RMP failed to produce a large static island. Nevertheless, the RMP still had an effect on the turbulence, as might be expected based on previous results in H-mode plasmas [16]. Figure 4.9 compares the spectra at $\rho = 0.65$ in the case of the screened RMP

and of the island, at the same pair of phases: $\phi_{RMP} = 10, 205°$. The screened RMP has a similar but much smaller effect than the island-forming RMP. The sharp step change in the turbulence response across the rational surface is absent in the case of the screened RMP (Figure 4.10). The screened RMP case was not repeated with other phases, so a full two-dimensional map of the turbulence response is not available.

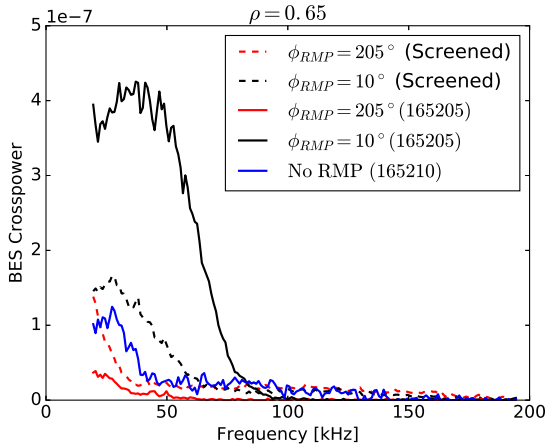

Figure 4.9: Comparison of the BES crosspower in the case of an RMP with and without an island. The screened RMP occurred in discharge 165204.

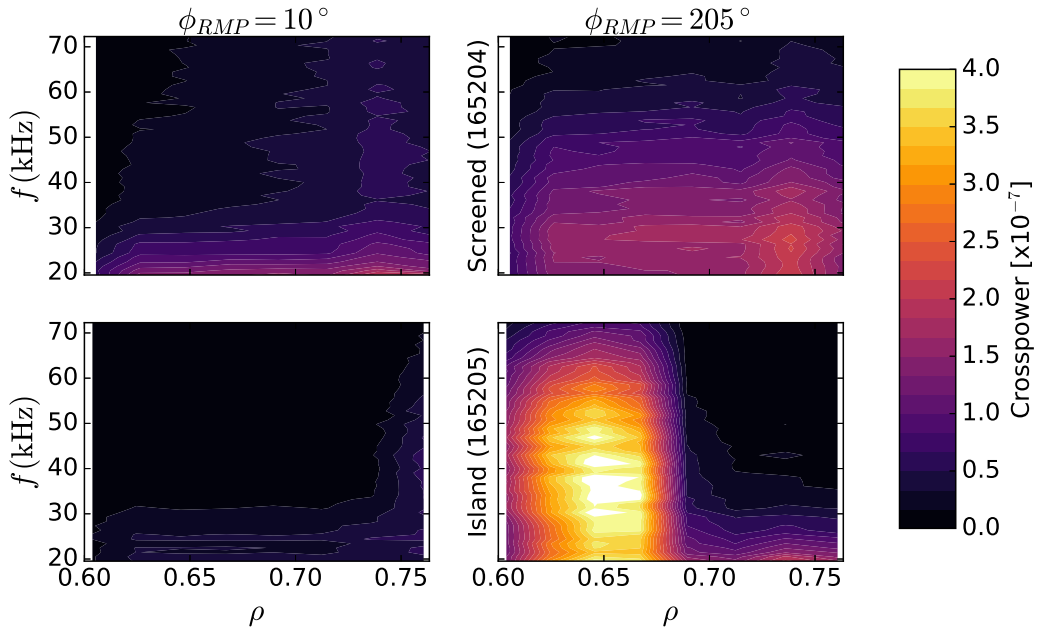

Figure 4.10: Comparison of the radial dependence of the BES spectra with a screened RMP against the case where the RMP forms an island. The top row is the screened RMP case. The bottom row shows the case with the island.

4.4 Summary

Although only preliminary results are available so far, the experiment was quite successful. The low-torque beam injection allowed the C-coils to trigger the $m, n = 2, 1$ island formation reliably. The island phase scan gave diagnostic access to the full two-dimensional cross-section of the island. The BES diagnostic was able to capture a strong modulation of the turbulence intensity in the vicinity of the island, matching some qualitative expectations based on gradient modifications by the island. The failure of the island formation due to above-threshold plasma rotation also showed that the screened RMP produces a much smaller effect on the turbulence.

Much remains to be done. The turbulence velocity and correlation lengths have not yet

been extracted from the BES data. Data from other turbulence diagnostics such as cross-polarization scattering and Doppler backscattering also awaits analysis. Inference of the island geometry from T_e and comparison to gyrokinetic simulations, as in Refs. [21] and [22] respectively, are logical next steps. Comparison between the static island case reported here and the rotating island experiments ([21, 22]) could also shed light on the role that island rotation plays in turbulence modification.

References

[1] B. S. Dewitt and R. N. Graham, American Journal of Physics **39**, 724 (1971).

[2] R. König, P. Grigull, K. McCormick, Y. Feng, J. Kisslinger, A. Komori, S. Masuzaki, K. Matsuoka, T. Obiki, N. Ohyabu, H. Renner, F. Sardei, F. Wagner, and A. Werner, Plasma Physics and Controlled Fusion **44**, 2365 (2002).

[3] T. E. Evans, R. A. Moyer, P. R. Thomas, J. G. Watkins, T. H. Osborne, J. A. Boedo, E. J. Doyle, M. E. Fenstermacher, K. H. Finken, R. J. Groebner, M. Groth, J. H. Harris, R. J. La Haye, C. J. Lasnier, S. Masuzaki, N. Ohyabu, D. G. Pretty, T. L. Rhodes, H. Reimerdes, D. L. Rudakov, M. J. Schaffer, G. Wang, and L. Zeng, Phys. Rev. Lett. **92**, 235003 (2004).

[4] K. Ida, T. Kobayashi, T. E. Evans, S. Inagaki, M. E. Austin, M. W. Shafer, S. Ohdachi, Y. Suzuki, S.-I. Itoh, and K. Itoh, Scientific Reports **5**, 16165 (2015).

[5] M. W. Shafer, R. J. Fonck, G. R. McKee, C. Holland, A. E. White, and D. J. Schlossberg, Physics of Plasmas **19**, 032504 (2012).

[6] W. Horton, Reviews of Modern Physics **71**, 735 (1999).

[7] P. W. Terry, Reviews of Modern Physics **72**, 109 (2000).

[8] E. Poli, A. Bottino, W. A. Hornsby, A. G. Peeters, T. Ribeiro, B. D. Scott, and M. Siccinio, Plasma Physics and Controlled Fusion **52**, 124021 (2010).

[9] O. Izacard, C. Holland, S. D. James, and D. P. Brennan, Physics of Plasmas **23**, 022304 (2016).

[10] W. A. Hornsby, A. G. Peeters, A. P. Snodin, F. J. Casson, Y. Camenen, G. Szepesi, M. Siccinio, and E. Poli, Physics of Plasmas **17**, 092301 (2010).

[11] D. Zarzoso, W. A. Hornsby, E. Poli, F. J. Casson, A. G. Peeters, and S. Nasr, Nuclear Fusion **55**, 113018 (2015).

[12] P. Hill, F. Hariri, and M. Ottaviani, Physics of Plasmas **22**, 042308 (2015), arXiv:arXiv:1412.6303v2 .

[13] P. Jiang, Z. Lin, I. Holod, and C. Xiao, Physics of Plasmas **21**, 122513 (2014).

[14] P. W. Terry, M. J. Pueschel, D. Carmody, and W. M. Nevins, Physics of Plasmas **20**, 112502 (2013).

[15] D. Carmody, M. J. Pueschel, J. K. Anderson, and P. W. Terry, Physics of Plasmas **22**, 012504 (2015).

[16] G. R. McKee, Z. Yan, C. Holland, R. J. Buttery, T. E. Evans, R. A. Moyer, S. Mordijck, R. Nazikian, T. L. Rhodes, O. Schmitz, and M. R. Wade, Nuclear Fusion **53**, 113011 (2013).

[17] K. Ida, N. Ohyabu, T. Morisaki, Y. Nagayama, S. Inagaki, K. Itoh, Y. Liang, K. Narihara, A. Y. Kostrioukov, B. J. Peterson, K. Tanaka, T. Tokuzawa, K. Kawahata, H. Suzuki, A. Komori, and LHD Experimental Group, Physical Review Letters **88**, 015002 (2002).

[18] T. Estrada, E. Ascasíbar, E. Blanco, A. Cappa, C. Hidalgo, K. Ida, A. López-Fraguas, and B. P. van Milligen, Nuclear Fusion **56**, 026011 (2016).

[19] K. Ida, K. Kamiya, A. Isayama, Y. Sakamoto, and JT-60 Team, Physical Review Letters **109**, 065001 (2012).

[20] K. J. Zhao, Y. J. Shi, S. H. Hahn, P. H. Diamond, Y. Sun, J. Cheng, H. Liu, N. Lie, Z. P. Chen, Y. H. Ding, Z. Y. Chen, B. Rao, M. Leconte, J. G. Bak, Z. F. Cheng, L. Gao, X. Q. Zhang, Z. J. Yang, N. C. Wang, L. Wang, W. Jin, L. W. Yan, J. Q. Dong, and G. Zhuang, Nuclear Fusion **55**, 073022 (2015).

[21] L. Bardóczi, T. L. Rhodes, T. A. Carter, N. A. Crocker, W. A. Peebles, and B. A. Grierson, Physics of Plasmas **23**, 052507 (2016).

[22] L. Bardóczi, T. L. Rhodes, T. A. Carter, A. Bañón Navarro, W. A. Peebles, F. Jenko, and G. McKee, Physical Review Letters **116**, 215001 (2016).

[23] B. W. Rice, D. G. Nilson, K. H. Burrell, and L. L. Lao, Review of Scientific Instruments **70**, 815 (1999).

[24] M. W. Shafer, E. A. Unterberg, A. Wingen, D. J. Battaglia, T. E. Evans, N. M. Ferraro, J. H. Harris, D. L. Hillis, and R. Nazikian, Physics of Plasmas **21**, 122518 (2014).

[25] J. T. Scoville and R. J. La Haye, Nuclear Fusion **43**, 250 (2003).

[26] M. E. Austin and J. Lohr, Review of Scientific Instruments **74**, 1457 (2003).

[27] M. W. Shafer, D. J. Battaglia, E. A. Unterberg, T. E. Evans, D. L. Hillis, and R. Maingi, Review of Scientific Instruments **81**, 10E534 (2010).

[28] M. W. Shafer, R. J. Fonck, G. R. McKee, and D. J. Schlossberg, Review of Scientific Instruments **77**, 10F110 (2006).

[29] G. R. McKee, R. J. Fonck, D. K. Gupta, D. J. Schlossberg, M. W. Shafer, and R. L. Boivin, Review of Scientific Instruments **77**, 10F104 (2006).

[30] G. R. McKee, R. J. Fonck, M. W. Shafer, I. U. Uzun-Kaymak, and Z. Yan, Review of Scientific Instruments **81**, 10D741 (2010).

[31] L. L. Lao, H. St. John, R. D. Stambaugh, A. G. Kellman, and W. Pfeiffer, Nuclear Fusion **25**, 1611 (1985).

[32] T. E. Evans, R. A. Moyer, and P. Monat, Physics of Plasmas **9**, 4957 (2002).

[33] O. Meneghini, S. P. Smith, L. L. Lao, O. Izacard, Q. Ren, J. M. Park, J. Candy, Z. Wang, C. J. Luna, V. Izzo, B. A. Grierson, P. B. Snyder, C. Holland, J. Penna, G. Lu, P. Raum, A. McCubbin, D. M. Orlov, E. A. Belli, N. Ferraro, R. Prater, T. H. Osborne, A. D. Turnbull, and G. M. Staebler, Nuclear Fusion **55**, 083008 (2015).

5 Electron thermal transport during tearing mode suppression in MST

Observations always involve theory.

— Edwin Hubble, *The Realm of the Nebulae* [1]

This chapter concerns Thomson scattering measurements of electron temperature profiles in improved confinement discharges in MST. Improved confinement is obtained by inductively driving current parallel to the magnetic field in the edge of MST to suppress tearing modes. This technique is referred to as 'pulsed parallel current drive' or PPCD. PPCD exhibits some puzzling thermal transport behavior. Chief among these is the large thermal conductivity of the core. The core tearing mode islands remain in the plasma, as evidenced by highly emissive structures observed by soft X-ray diagnosis [2]. However, the mode overlap is very low, such that there are good flux surfaces separating the islands (see Hudson's thesis [3, fig. 3.12]). This means that stochastic transport cannot explain the core conductivity [4]. Another puzzle is the absence of tearing-mode-correlated electron temperature fluctuations [5, sec. 4.4], which is surprising given the soft X-ray measurements and magnetic modeling.

Following an overview of PPCD (Section 5.1), Section 5.2 discusses how the maximum electron pressure observed in MST has been obtained. The dynamics of the average temperature

profile during PPCD are discussed in Section 5.3. The linear temperature ramp-up suggests that transport is suddenly and completely suppressed at PPCD initiation, so that the rise in temperature is determined only by the available (Ohmic) heating power. Analysis of the thermal power balance in Section 5.4 for a particular discharge supports this hypothesis. Finally, in Section 5.5, the non-observation of island temperature structures by Thomson scattering is revisited. If the temperature has not reached equilibrium, gradients will not have had time to develop, which would explain the lack of island T_e structure observations. The soft X-ray observations could be explained by impurity-confining islands. The large core conductivity remains unexplained.

5.1 Overview

Tearing modes are an integral part of the standard operation of the RFP. The inductively-driven toroidal current must be converted by the MHD dynamo mechanism into poloidal current in order to sustain the reversed toroidal magnetic field [6]. This process occurs spontaneously due to the tearing mode instabilities which derive their energy by reducing the total magnetic energy of the plasma. This flattens the parallel current profile in accordance with the model of Taylor [7]. The side-effect of the tearing mode dynamo process is the stochastic magnetic field which results in reduced energy confinement.

It is possible to drive poloidal current and replace the dynamo, resulting in improved confinement. Although DC injection [8] and RF current drive [9] have been proposed and tested [10], the most successful method to date has been induction (PPCD). To induce a poloidal current, the toroidal flux must be changed, which means modifying the toroidal magnetic field inside the plasma. In practice, this means forcing the edge magnetic field to be even more strongly reversed with respect to the core magnetic field. Thus, the q-profile is modi-

fied. As with any induction, this process cannot be sustained indefinitely. Thus, the poloidal current drive is inherently pulsed.

PPCD discharges transiently achieve tearing mode suppression and improved confinement in the RFP [4, 10, 11, 12, 13, 14, 15, 16, 17]. The highest electron temperatures achieved in MST in this manner are about 2 keV. The electron temperature is often observed to increase linearly throughout the PPCD pulse, only to rapidly fall when the induction ceases and a violent resurgence of the tearing modes occurs.

The mean temperature profile during PPCD is approximately trapezoidal in shape across the diameter, with a steep gradient in the edge but little to no core gradient. The gradient at mid-radius has been shown to be consistent with estimates of stochastic transport [4], but the extremely flat core temperature remains unexplained. The gradient region can be stochastic even at very low tearing mode amplitude due to the closely-spaced resonant surfaces. However, because the mode amplitudes are small, the magnitude of the stochastic transport can be reduced [17]. The thermal conductivity in the mid-radius region has been shown to be proportional to the mean squared amplitude of the higher-n modes [18] (where n is the toroidal mode number).

Not all PPCD discharges achieve tearing mode suppression. Most high-current PPCD discharges in fact experience sawtooth crashes during the PPCD pulse, spoiling the confinement. Roughly one-quarter to one-third of high-current PPCD discharges have long crash-free phases resulting in high temperatures. The low success rate appears to be due to variations in the plasma rather than in the applied induction which is reproducible. It is possible that the planned upgrade to the MST power supplies would allow feedback control of the inductive voltage to match plasma conditions, thereby improving PPCD quality.

5.2 Crash-heating

Two styles of PPCD have been developed: crash-heated PPCD and non-crash-heated. The primary difference is the rapidity with which the field reversal is forced. Crash-heated PPCD involves more rapid and deeper field reversal, resulting in larger inductive electric field $E_{\|}$ and more rapid attainment of high confinement [17]. These differences are illustrated in Figure 5.1.

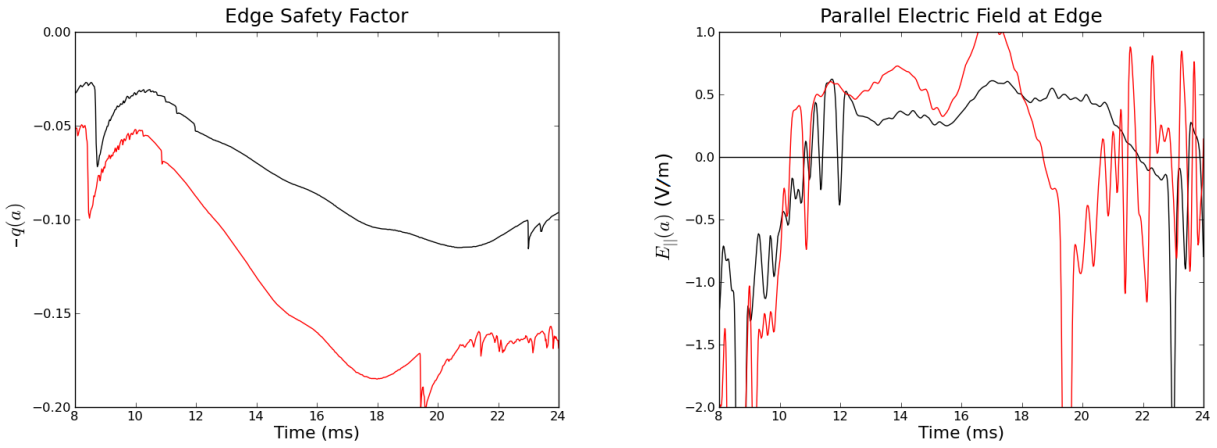

(a) **(b)**

Figure 5.1: (a) Edge q during example crash-heated PPCD (red) and non-crash-heated (black) discharges. (b) Parallel electric field at the wall during the same discharges. Crash-heated PPCD achieves larger inductive field more rapidly, but does not last as long.

The rapid onset of the improved confinement allows ion heating caused by sawtooth crashes occurring prior to the PPCD application to be retained, hence the name crash-heated PPCD [17]. Crash-heating also results in the highest observed electron temperatures $T_e \sim 2\,\mathrm{keV}$. The total electron pressure is a more relevant metric, as shown in Figure 5.2. Crash-heating produces higher maximum electron pressure (defined as the product of the core-averaged electron temperature with the line-averaged electron density) compared to non-crash-heated

PPCD. The highest temperatures observed are at lower density, because the two variables are anti-correlated. This suggests the existence of a limit on the plasma pressure, although it may only be in the form of a limit on the available thermal energy source (Ohmic heating). Experiments with pellet-injection to increase density have shown that the ratio of plasma pressure to magnetic field pressure β can reach 26% without triggering explosive instabilities [19].

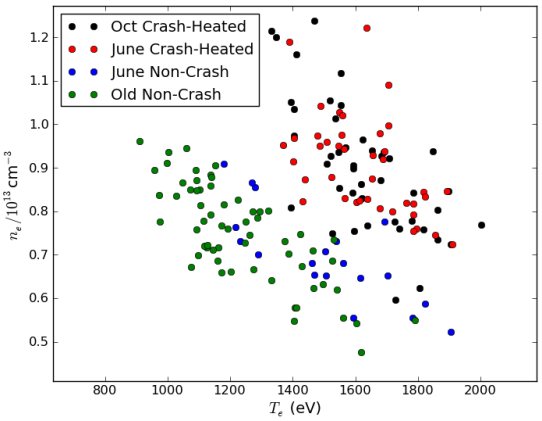

Figure 5.2: PPCD peak electron temperature and density for crash-heated and non-crash-heated discharges. Pressure and density are negatively correlated, indicating a limit on their product (electron pressure). Crash-heated discharges with up to $T_e = 2\,\mathrm{keV}$ are observed.

5.3 PPCD temperature profiles

The temperature profile evolution during a PPCD discharge follows an essentially linear trend with time, up until the point at which it stagnates at a maximum value. In the best-confinement discharges, no stagnation occurs, and the temperature is still rising until the inductive drive runs out and the crash occurs. To illustrate this, a set of high-performance discharges was selected where the Thomson scattering data was taken at a rate of 2 kHz for 30 pulses, covering the PPCD induction period. The time basis of each discharge was shifted so

that the transition to a stagnated state occurred at the same time. The profiles were averaged together to reduce statistical variations. Figure 5.3 shows that the mean temperature profile shape is quite consistent over time, with the amplitude rising essentially linearly with time. Normalizing to the core-averaged temperature results in a clearer demonstration that the temperature profile shape is fixed during the evolution (Figure 5.4).

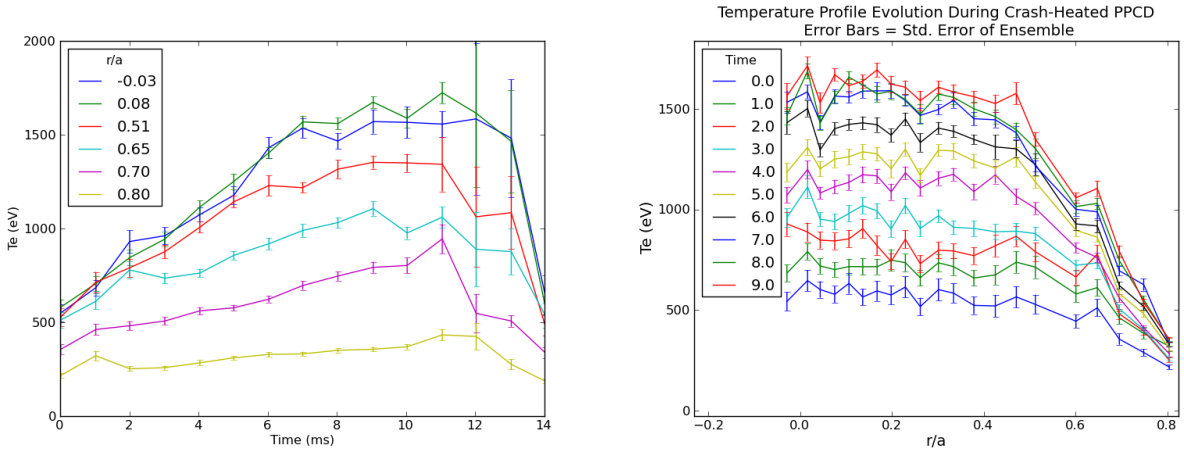

(a) **(b)**

Figure 5.3: PPCD average T_e profile evolution. Prior to averaging, the discharges were shifted in time such that the end of the temperature ramp-up was aligned across discharges. (a) Each curve shows the value of the temperature over time at one radius. (b) Each curve shows the temperature at a fixed time as a function of radius.

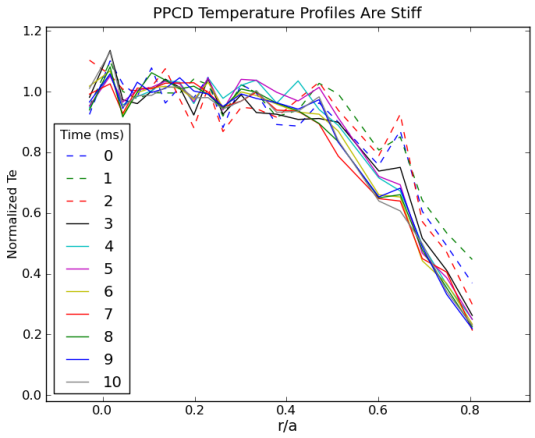

Figure 5.4: PPCD profile consistency is shown by normalizing the temperature profile to the mean value in the core at each time slice.

The linear T_e increase over time is suggestive of the following situation. The application of PPCD rapidly reduces the mode amplitudes, stochasticity, and transport in the mid-radius gradient region to much smaller levels. The input Ohmic heating power is no longer balanced by transport. Therefore, almost all the Ohmic heating power goes toward increasing the plasma temperature. If the Ohmic power is constant and the heat losses remain relatively small, the temperature will rise linearly at all points.

If the mode suppression were maintained indefinitely, the increasing gradients would gradually raise the heat flux until a steady-state temperature profile was reached. The transition from linearly-rising to stagnant temperature occurs rapidly, however, suggesting a sudden change in transport. This prompted an investigation, detailed in the next section, to see whether this stagnation might be a sign of a limit on the electron temperature or pressure gradient, perhaps due to the onset of drift-wave instability and turbulence.

5.4 Power balance analysis

A more detailed look at the energy balance during PPCD was conducted for a particular shot where the temperature evolution rapidly transitioned from linear growth to stagnation. Two time points, one during the linear ramp phase, and one during the (brief) stagnated phase were studied in particular. The temperature was rising at 180 eV/ms in the core at 13 ms, but then stopped rising by 17.5 ms as shown in Figure 5.5.

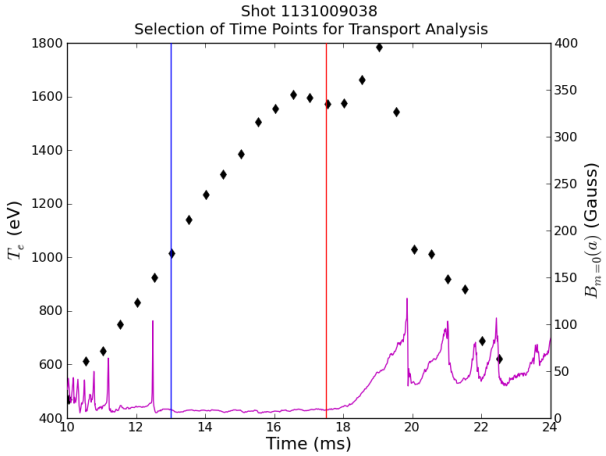

Figure 5.5: Core T_e evolution (black diamonds) during the selected PPCD discharge, along with root-mean-square of the $m = 0$ mode amplitudes at the wall (magenta trace). Vertical lines mark the time points selected for transport analysis. Low $m = 0$ amplitude correlates well with periods of improved confinement [15].

Integrating the thermal energy equation for electrons (where W is the thermal energy density):

$$\eta J^2 + \nabla \cdot \mathbf{Q} = \frac{dW}{dt} \tag{5.1}$$

over flux surfaces yields a relation between the net thermal energy balance and the heat flux

escaping radially outward through a flux surface:

$$P_\Omega - \frac{dE}{dt} = -AQ_{tot}. \tag{5.2}$$

Here E and P_Ω are the total thermal energy and Ohmic heating power integrated over the volume enclosed by the flux surface. Q_{tot} is the average heat flux through the surface, which must be multiplied by the surface area A to yield the thermal power escaping through a flux surface. The transport module of MSTFIT calculates these quantities assuming axisymmetric flux surfaces with circular cross-section. The rate of change of thermal energy $\frac{dE}{dt}$ is calculated by taking the difference in the thermal energy profiles between two adjacent time slices, which in this case were the preceding and following Thomson scattering measurement times. Q_{tot} is inferred from the left-hand-size of Equation 5.2.

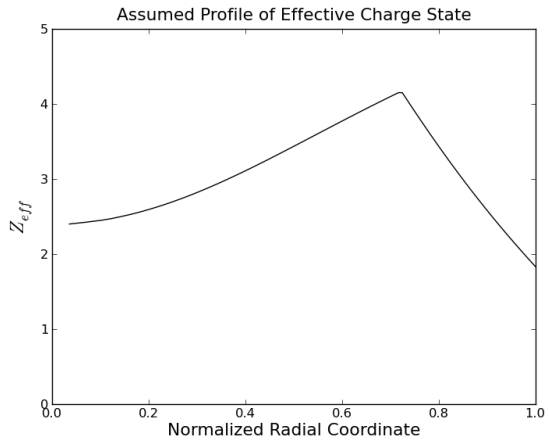

Figure 5.6: Assumed Z_{eff} profile based on prior studies of impurity content in high-current PPCD plasmas [20, 21].

In order to estimate the heating power MSTFIT uses the current density and the resistivity to find ηJ^2. Reconstructions are difficult to do accurately even without the highly dynamic PPCD induction. On the other hand, the total toroidal current in the plasma is well-defined

by edge-measurements, which places a helpful constraint on the problem. The effective ionic charge state Z_{eff} profile is also a key component, since the resistivity η is a function of Z_{eff} (which itself depends on the plasma impurity content). Figure 5.6 shows the Z_{eff} profile based on previous results for high-current PPCD [20, 21].

In Figure 5.7 the three terms in Equation 5.2 are plotted for the two time slices. The integrated Ohmic heating power profile is quite similar at both times. The resistivity decreases with temperature, $\eta \propto T_e^{-3/2}$. At first glance, this seems to imply that the rising temperature during the discharge should cut the Ohmic heating power by a factor of about 1/2 between the 13 and 17.5 ms. However, the core, having smaller volume and already being hotter than the edge, accounts for less of the Ohmic heating power than the edge region, despite the fact that the current density peaks in the core. The net result is that the volume-integrated Ohmic heating power is only slightly reduced by 17.5 ms.

During the linear ramp phase, the thermal energy increase accounts for essentially the entirety of the Ohmic heating power, in agreement with the hypothesis presented earlier to explain the linear rise. Then at 17.5 ms, the thermal energy absorption falls to zero, while the integrated Ohmic heating is still large. This implies a large increase in the heat flux (Figure 5.7b).

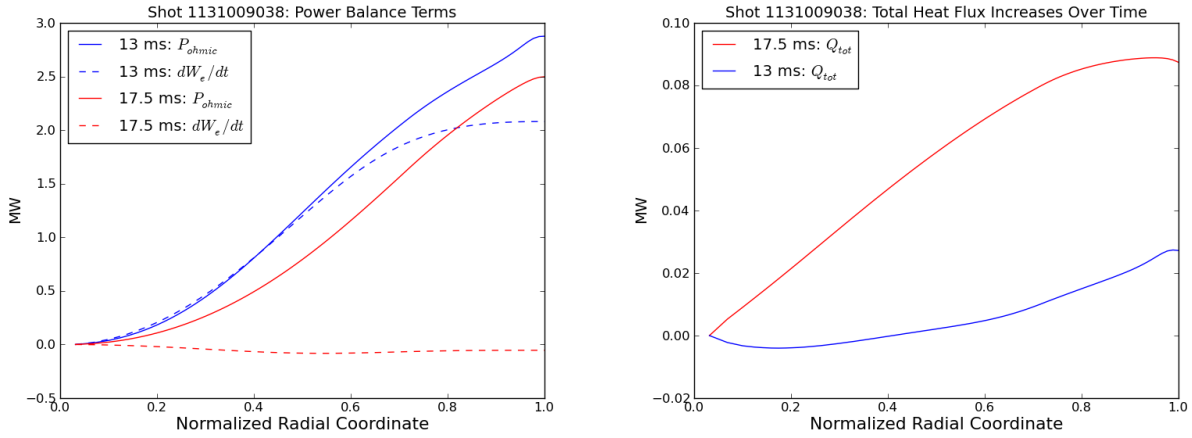

(a) **(b)**

Figure 5.7: (a) Ohmic heating power during the T_e ramp-up is channeled almost entirely into raising the plasma thermal energy, while during the plateau, the rate of thermal energy increase drops to zero. (b) As a consequence, the heat flux escaping the plasma is initially small but increases several-fold by 17.5 ms.

If the thermal flux is conductive (ie, $\mathbf{Q} = n_e \chi_e \nabla T_e$) then the conductivity must have increased sharply. This is shown to be the case in Figure 5.8, where the conductivity estimated via MSTFIT increases an order of magnitude in the gradient region. The natural suspect would be the stochasticity caused by tearing modes.

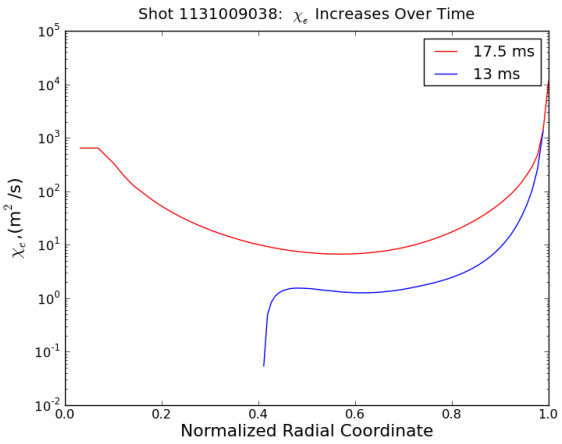

Figure 5.8: Electron thermal conductivity profile from MSTFIT at 13 and 17.5 ms. The conductivity estimate diverges at 13 ms inside $r/a = 0.4$ due to the negative heat flux estimate.

5.4.1 Quasilinear stochastic transport estimate

The relevant tearing modes are the high-n modes that are resonant near the reversal surface, as shown by Yang in Ref. [18]. The mean of the squared mode amplitudes for the $n = 7-15$ modes were used as a proxy for the stochastic transport, since it was shown in [18] that this is a good measure: $\chi_{e,m} \propto \langle B^2_{\phi,n}(a)\rangle_n$. Figure 5.9 shows that the mean square amplitude of the high-n modes increases several-fold between 16 and 17.5 ms, just when the core T_e stops rising. Estimating from Figure 5.9 that at 17.5 ms $\langle B^2_{\phi,n}(a)\rangle \approx 10\,\mathrm{G}^2$ and referring to the scaling in [18, fig. 3.13] indicates an expected $\chi_{e,m} \approx 15\,\mathrm{m}^2/\mathrm{s}$. (The plasmas analyzed in Ref. [18] are also 500 kA PPCD discharges, so this scaling is assumed to be directly applicable.) This conductivity value is consistent with the conductivity profile in Figure 5.8. The fact that $\langle B^2_{\phi,n}(a)\rangle$ is an order of magnitude lower during the ramp phase coincides with the order of magnitude difference between the conductivities at 13 and 17.5 ms. Thus, in this case, the end of the rapid T_e ramp-up can be attributed to an increase in stochastic transport due to

resurgence of the high-n tearing modes just before the final crash at the end of the current drive period.

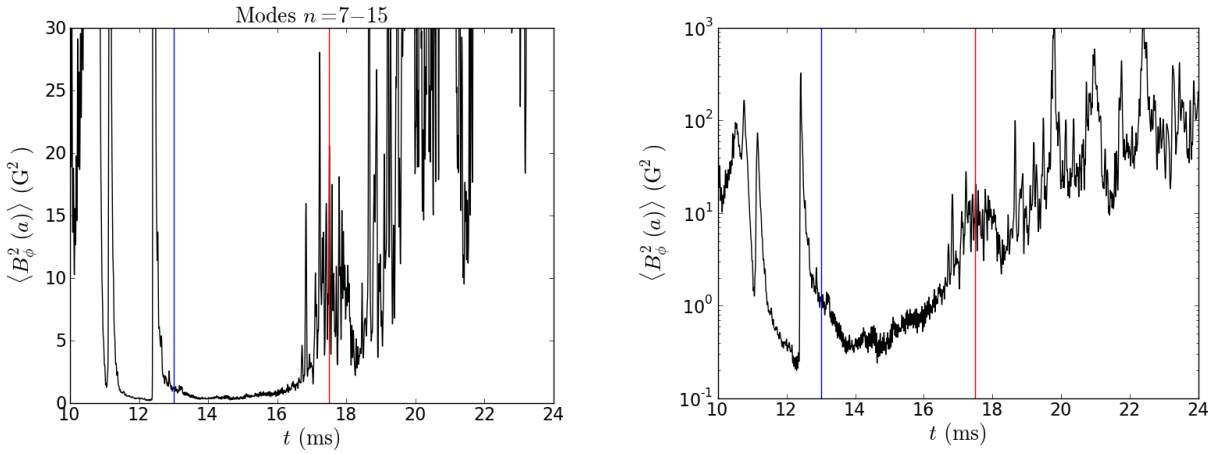

Figure 5.9: Linear (a) and log (b) scale of the mean $n = 7 - 15$ mode squared amplitudes during the discharge.

5.5 Magnetic islands in PPCD

Electron temperature fluctuation measurements made in PPCD discharges have consistently been unable to reveal any temperature fluctuations correlated with tearing modes [5, sec. 4.4]. Even a measurement of general low-frequency T_e fluctuations (not reliant on tearing-mode correlation) shows that PPCD plasmas have reduced fluctuations (see Section 2.3.3). However, soft X-ray tomography has revealed highly emissive structures indicative of magnetic islands with local confinement [2]. PPCD does not totally eliminate tearing mode islands, nor does the improved confinement depend on the disappearance of all islands (as shown in a Poincaré plot made by Hudson for a PPCD discharge [3, fig. 3.12]). The mode overlap simply needs to be reduced, especially in the outer stochastic region, in order to

produce improved confinement. The lack of observed island temperature structures is thus not explained by the vanishing of magnetic islands.

One possible explanation is that there is no effect of the magnetic island topology on the temperature simply because the transport is far from equilibrium. Here equilibrium means the condition that $\frac{dW}{dt} \ll P_\Omega$ such that the outward heat flux is nearly equal to the Ohmic power. If the thermal transport is far from equilibrium, $\frac{dW}{dt} \approx P_\Omega$ while transport is small. In the non-equilibrium situation, the integral over time of the Ohmic heating power at a particular location yields the local temperature value, according to

$$T_e(t) = T_e(t_0) + \frac{1}{n_e} \int_{t_0}^{t} dt' \eta J^2. \tag{5.3}$$

Transport does not appear in the equation, so the flux surface geometry does not play a role in shaping the temperature, at least in the strongly non-equilibrium approximation used here. If current profile control could be maintained indefinitely, so that the temperature could reach equilibrium, then gradients would be reestablished and any islands remaining might be detected by TS. In the non-equilibrium scenario for PPCD, the soft X-ray emissivity coming from the islands would be due to the confinement of impurities rather than thermal energy. There is precedent (in tokamaks) for the presence of impurity-confining core islands [22].

5.6 Conclusion

The transport situation in PPCD is not completely understood. In particular, the extremely flat core temperature profile seems to imply large core conductivity, which cannot be explained as stochastic transport [4]. Stochasticity does account for the transport at mid-radius

[18]. The evidence in this chapter indicates that the linear T_e ramp-up is a consequence of the large (order of magnitude) and sudden drop of the stochastic transport upon application of the parallel current drive. The temperature evolves according to $dW/dt \approx \eta J^2$ because the transport is negligible, even up to 1.5 keV core T_e. The lack of observation of temperature islands can be attributed, according to this model, to the fact that the temperature does not reach a steady-state condition such that gradients can be established in the core.

For the shot analyzed in detail in this chapter, the resurgence of the high-n tearing modes is probably the cause of the T_e stagnation just before the final crash. It remains to be seen if this is the case for all discharges, or whether there are instances in which some mechanism other than stochastic transport must be invoked in the gradient region. It is possible that the large pressure gradients drive the tearing mode resurgence at the end of PPCD, rather than the usual current gradients [23]. The maximum plasma beta in the discharge studied in detail here was $\beta < 8\%$. Comparison with low-current PPCD discharges, which reach higher β, would be helpful in this regard. A detailed stability study is necessary before further conclusions can be made about pressure drive for tearing modes in PPCD.

The 2 keV maximum temperature observed so far is probably not a hard limit of MST's performance. An upgrade underway to MST's power supply system will allow fine control of the inductive voltage, perhaps even with feedback to match the plasma conditions. By extending the mode suppression duration and tailoring the inductive drive, even higher temperatures and pressures might be achieved.

References

[1] E. Hubble, *The Realm of the Nebulae* (Yale University Press, New Haven, 1982) p. 35.

[2] P. Franz, L. Marrelli, P. Piovesan, B. E. Chapman, P. Martin, I. Predebon, G. Spizzo, R. B. White, and C. Xiao, Physical Review Letters **92**, 125001 (2004).

[3] B. F. Hudson, *Fast Ion Confinement in The Reversed-Field Pinch*, Phd thesis, University of Wisconsin (2006).

[4] J. K. Anderson, J. Adney, A. Almagri, A. Blair, D. L. Brower, M. Cengher, B. E. Chapman, S. Choi, D. Craig, D. R. Demers, D. J. Den Hartog, B. Deng, W. X. Ding, F. Ebrahimi, D. Ennis, G. Fiksel, C. B. Forest, P. Franz, J. Goetz, R. W. Harvey, D. Holly, G. T. A. Huijsmans, M. Kaufman, T. Lovell, L. Marrelli, P. Martin, K. McCollam, V. V. Mirnov, P. Nonn, R. O'Connell, S. Oliva, P. Piovesan, S. C. Prager, I. Predebon, J. S. Sarff, G. Spizzo, V. Svidzinski, M. Thomas, and M. D. Wyman, Physics of Plasmas **12**, 056118 (2005).

[5] H. D. Stephens, *Electron Temperature Structures Associated With Magnetic Tearing Modes in the Madison Symmetric Torus*, Phd thesis, University of Wisconsin - Madison (2010).

[6] E. Caramana and D. Baker, Nuclear Fusion **24**, 423 (1984).

[7] J. B. Taylor, Physical Review Letters **33**, 1139 (1974).

[8] Y. Ho, Nuclear Fusion **31**, 341 (1991).

[9] E. Uchimoto, M. Cekic, R. W. Harvey, C. Litwin, S. C. Prager, J. S. Sarff, and C. R. Sovinec, Physics of Plasmas **1**, 3517 (1994).

[10] J. S. Sarff, J. K. Anderson, T. M. Biewer, D. L. Brower, B. E. Chapman, P. K. Chattopadhyay, D. Craig, B. H. Deng, D. J. Den Hartog, W. X. Ding, G. Fiksel, C. B. Forest, J. A. Goetz, R. O'Connell, S. C. Prager, and M. A. Thomas, Plasma Physics and Controlled Fusion **43**, 1684 (2003).

[11] J. S. Sarff, S. A. Hokin, H. Ji, S. C. Prager, and C. R. Sovinec, Phys. Rev. Lett. **72**, 3670 (1994).

[12] J. S. Sarff, A. F. Almagri, M. Cekic, C.-S. Chaing, D. Craig, D. J. Den Hartog, G. Fiksel, S. A. Hokin, R. W. Harvey, H. Ji, C. Litwin, S. C. Prager, D. Sinitsyn, C. R. Sovinec, J. C. Sprott, and E. Uchimoto, Phys. Plasmas **2**, 2440 (1995).

[13] M. R. Stoneking, N. E. Lanier, S. C. Prager, J. S. Sarff, and D. Sinitsyn, Physics of Plasmas **4**, 1632 (1997).

[14] B. E. Chapman, T. M. Biewer, P. K. Chattopadhyay, C.-S. Chiang, D. Craig, N. A. Crocker, D. J. Den Hartog, G. Fiksel, P. W. Fontana, S. C. Prager, and J. S. Sarff, Physics of Plasmas **7**, 3491 (2000).

[15] B. E. Chapman, J. K. Anderson, T. M. Biewer, D. L. Brower, S. Castillo, P. K. Chattopadhyay, C.-S. Chiang, D. Craig, D. J. Den Hartog, G. Fiksel, P. W. Fontana, C. B. Forest, S. Gerhardt, A. K. Hansen, D. Holly, Y. Jiang, N. E. Lanier, S. C. Prager, J. C. Reardon, and J. S. Sarff, Physical Review Letters **87**, 205001 (2001).

[16] B. E. Chapman, A. F. Almagri, J. K. Anderson, T. M. Biewer, P. K. Chattopadhyay, C. S. Chiang, D. Craig, D. J. Den Hartog, G. Fiksel, C. B. Forest, A. K. Hansen, D. Holly, N. E. Lanier, R. O'Connell, S. C. Prager, J. C. Reardon, J. S. Sarff, M. D. Wyman, D. L. Brower, W. X. Ding, Y. Jiang, S. D. Terry, P. Franz, L. Marrelli, and P. Martin, Physics of Plasmas **9**, 2061 (2002).

[17] B. E. Chapman, A. F. Almagri, J. K. Anderson, D. L. Brower, K. J. Caspary, D. J. Clayton, D. Craig, D. J. Den Hartog, W. X. Ding, D. A. Ennis, G. Fiksel, S. Gangadhara, S. Kumar, R. M. Magee, R. O'Connell, E. Parke, S. C. Prager, J. A. Reusch, J. S. Sarff, H. D. Stephens, and Y. M. Yang, Plasma Physics and Controlled Fusion **52**, 124048 (2010).

[18] Y. M. Yang, *Stochastic Transport in PPCD Discharges*, Ms thesis, University of Wisconsin - Madison (2010).

[19] M. D. Wyman, B. E. Chapman, J. W. Ahn, A. F. Almagri, J. K. Anderson, F. Bonomo, D. L. Brower, S. K. Combs, D. Craig, D. J. Den Hartog, B. H. Deng, W. X. Ding, F. Ebrahimi, D. A. Ennis, G. Fiksel, C. R. Foust, P. Franz, S. Gangadhara, J. A. Goetz, R. O'Connell, S. P. Oliva, S. C. Prager, J. A. Reusch, J. S. Sarff, H. D. Stephens, and T. Yates, Physics of Plasmas **15**, 010701 (2008).

[20] T. Barbui, L. Carraro, D. J. Den Hartog, S. T. A. Kumar, and M. Nornberg, Plasma Physics and Controlled Fusion **56**, 075012 (2014).

[21] M. E. Galante, L. M. Reusch, D. J. Den Hartog, P. Franz, J. R. Johnson, M. B. McGarry, M. D. Nornberg, and H. D. Stephens, Nuclear Fusion **55**, 123016 (2015).

[22] L. Delgado-Aparicio, L. Sugiyama, R. Granetz, D. A. Gates, J. E. Rice, M. L. Reinke, M. Bitter, E. D. Fredrickson, C. Gao, M. Greenwald, K. Hill, A. Hubbard, J. W. Hughes, E. Marmar, N. Pablant, Y. Podpaly, S. Scott, R. Wilson, S. Wolfe, and S. Wukitch, Physical Review Letters **110**, 065006 (2013).

[23] R. Paccagnella, Physics of Plasmas **20**, 012119 (2013).

6 Thomson scattering calibration improvements

> *Since computing has become cheaper than thinking, the reader should not be afraid to use a simple tool and pound the problem into submission.*
>
> — John F. Monahan, *Numerical Methods of Statistics* [1]

Thomson scattering diagnostics require a variety of calibrations in order to provide accurate measurements of electron temperature, density, and their uncertainties. This chapter details improvements made in the calibration methods used on the MST TS system detectors, both for improved quality of T_e measurements and for ease of use. First, a brief overview of the detector hardware of the MST TS system is presented in Section 6.1. Next, the mathematical model of the detector system used in the analysis software is discussed (Section 6.2), with an emphasis on the role of calibrations in obtaining the model parameters. An explanation of the relationship to, and improvements over, the previous system model are discussed in Section 6.3.

The subsequent sections describe improvements to the three main calibration procedures. The gain calibration and noise calibration, previously conducted simultaneously, can be separated. An alternative method for measuring the detector gain is proposed in keeping with the improved system model (Section 6.4). The noise calibration (Section 6.5) becomes far

less intensive when decoupled from the gain calibration, enabling more frequent calibrations. The noise model has also been extended to cover previously neglected noise source which may be important in certain cases. The spectral calibration reproducibility has been improved by the use of a supercontinuum light source (Section 6.6), which is expected to reduce systematic errors in the measured T_e profiles. This improvement was motivated by experimental needs encountered in studying tearing mode temperature structures.

6.1 Detector hardware

The collection and detection process begins when the Thomson scattered light is imaged on an array of 21 fiber optic cables which transmit the light from the MST machine area back to the Thomson scattering diagnostic room where the detectors are located. The fiber cables lead to 21 filter polychromators, built by General Atomics (GA) [2]. Inside a polychromator, light from the cable is collimated and directed toward a set of narrow-band interference filters. Each filter transmits a portion of the spectrum and reflects the rest. The reflected light from one filter continues to the next filter, so that no light is wasted (see Figure 6.1).

The light transmitted through a filter falls upon a silicon avalanche photodiode (APD), which converts the photon flux to an electrical current with high efficiency (up to 85% [3]). The primary photoelectrons undergo an avalanche process inside the APD, which multiplies the current by a factor of about one hundred. The current is converted to a voltage and amplified by a custom circuit referred to as a preamplifier (also GA-designed) before being sent to a digitizer.

The preamplifier has 'AC' and 'DC' output channels. The DC channel is meant to provide a measurement of the background light level, which is important for estimating the noise

in the measurements. The AC channel discards the low-frequency component in order to efficiently utilize the digitizer dynamic range to resolve the pulsed signal. The DC channel is a full-bandwidth output which is presently digitized on a Strück VME digitizer system with 16-bit resolution and 100 MHz sampling rate. The AC channel is high-pass filtered using a 100 ns delay line and a difference amplifier. This output is digitized with an Acqiris digitizer at 8-bit resolution and 1 GHz sampling rate.

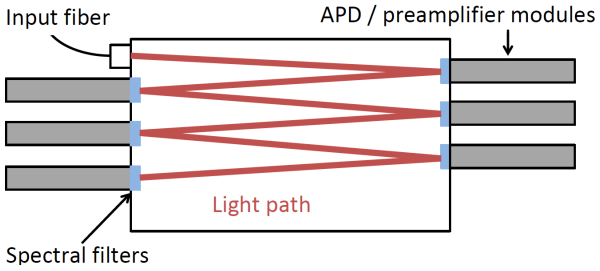

Figure 6.1: Layout of one GA polychromator with six APD detectors and preamplifier modules. Six of the twenty-one polychromators have two additional channels installed.

6.2 Analysis method and system model

The digitized signals from each APD detector on each polychromator are analyzed automatically to produce the best estimate of the electron temperature and density and the uncertainty of the estimate. This is accomplished in two steps. First, the amplitude of the scattered light pulse is determined from the APD signal. The uncertainty in the amplitude is estimated as well. The amplitude estimation is done using the method of characteristic pulse fitting. This method has the advantage of reducing the contribution of background noise relative to other methods of finding the pulse amplitude [4]. It relies on having a reproducible pulse shape. The pulse shape is determined by the laser pulse shape (20 ns wide) and the preamplifier circuit response, which has a shaping time of about 40 ns. Figure 6.2

shows an example scattered light signal and the pulse fit for the DC output of the detector.

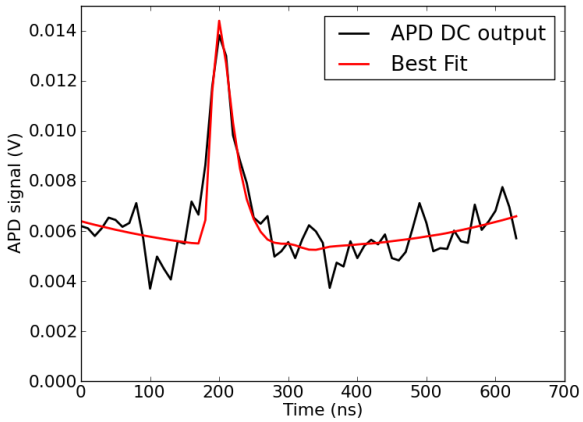

Figure 6.2: Example of fitting characteristic pulse plus background to the digitized DC output from an APD. The integral of the pulse (minus the background contribution) yields the signal S.

In the second analysis step, the temperature T_e and (uncalibrated) density n_e (along with their statistical uncertainties) are solved for in the analysis software using a Bayesian approach. The first part of this process is to minimize the χ^2 cost function of the difference between the measured signal and the model, to find the most probable values of T_e, n_e:

$$\chi^2(T_e, n_e) = \sum_{i=1}^{N} \left(\frac{S_i^{measured} - S_i^{model}(T_e, n_e)}{\sigma_i^{model}} \right)^2. \tag{6.1}$$

For more detail on the spectral model and the Bayesian analysis process, refer to [5, 6, 7]. Figure 6.3 shows the scattered spectrum shape for various values of T_e, as well as an example of fitting to actual data.

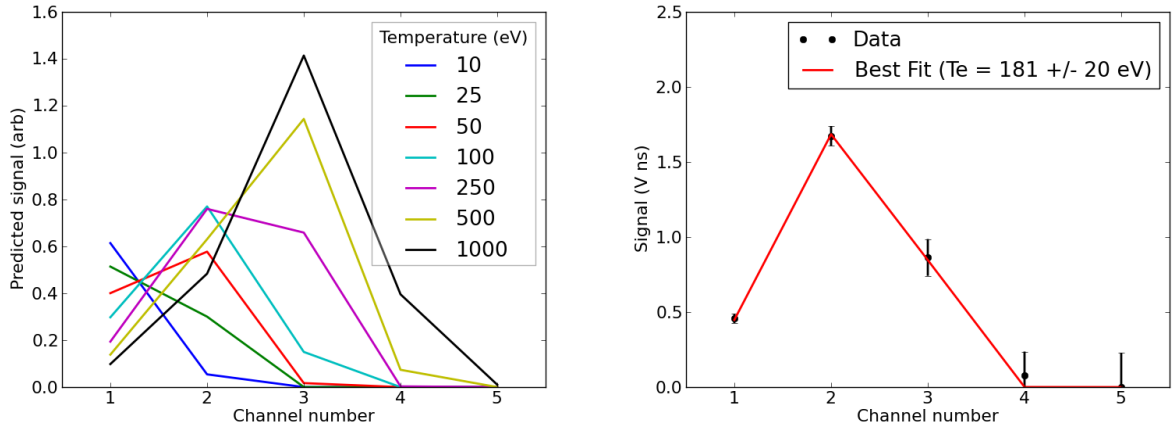

Figure 6.3: (a) Predicted signals S_i from the different wavelength channels on a 6-channel polychromator for a wide range of T_e , illustrating how the spectral shape is informative about T_e. (Note that Channel 0 is not used because it is saturated with stray laser light.) (b) Example of fitting the signal amplitudes S_i to arrive at the best-fit T_e . The uncertainty of T_e is found using Bayesian analysis.

6.2.1 Polychromator spectral model

The analysis of the observed scattered signal amplitudes S_i from each wavelength channel $i = 1, 2, 3...$ on a polychromator to determine the electron temperature T_e hinges on the calibration of the polychromator instrument function. The signals S_i are produced by convolving the instrument function I_i with the scattered spectrum ν:

$$S_i(T_e, n_e) = \int d\lambda I_i(\lambda)\nu(\lambda, T_e, n_e). \tag{6.2}$$

The instrument function,

$$I_i(\lambda) = T_i(\lambda)G_i M_i \eta_i(\lambda), \tag{6.3}$$

is the product of the transmission function T of the interference filter in the polychromator

(and other optics in the collection system) with the overall gain of the APD and preamplifier module. Here $G = G_v R q$ is the gain of the preamplifier in volt-seconds per photon, where G_v is the voltage gain of the preamplifier, R is the current-sensing resistance in Ohms, and q is the elementary charge. The APD avalanche gain is M, and the quantum efficiency is η. The wavelength-dependence of η for an APD from the MST TS system is shown in Figure 6.4.

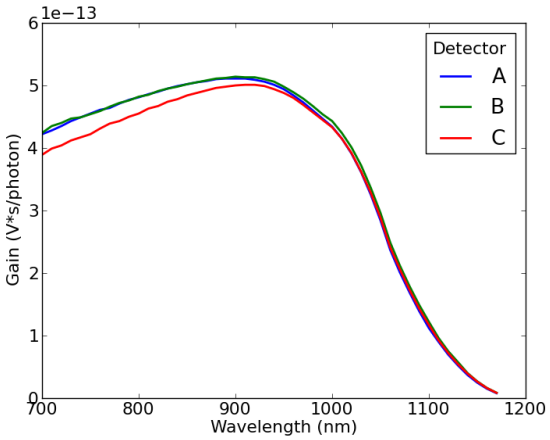

Figure 6.4: Overall gain $GM\eta(\lambda)$ of the reference APDs calibrated by Canadian National Research Council's Institute for National Measurement Standards (INMS) as discussed in [8].

The scattered photon spectral density $\nu(\lambda, T_e, n_e)$ in photons per nanometer arriving at the polychromator is proportional to the plasma electron density n_e: $\nu(\lambda, T_e, n_e) = n_e \hat{\nu}(\lambda, T_e)$, where $\hat{\nu}$ is the spectrum normalized by n_e. In principle, the TS diagnostic could provide a measure of the plasma density as well. In practice, a separate calibration procedure (such as described in [9]) is required to obtain meaningful density measurements. (This density calibration has been preempted for the MST TS system by stray laser light reflecting from the vacuum vessel walls. Efforts to reduce the stray light are on-going.) Therefore, the importance of the spectral calibration (Section 6.6) lies not in the absolute scale of the instrument functions I_i, but in the relative values between the channels on an individual

polychromator which yield the shape of the spectrum and hence T_e.

6.2.2 Detector noise model

Calibration of the detector signal noise σ_i^{model} as a function of the signal amplitude and of the background plasma light level is also important for the precision of temperature measurements. The Bayesian calculation provides the uncertainty in the T_e measurements based on the uncertainty in the signals. This requires accurate uncertainties for the signals to be known. Additionally, an incorrect noise model for a detector can cause an unreliable signal to be weighted more strongly in χ^2 in Equation 6.1, resulting in noisier T_e estimation.

The noise model developed in [4] is written in terms signal variance σ^2:

$$\sigma^2 = \epsilon^2 S^2 + GMFS + (GMFs_{bg} + v_e^2)\tau_{int}. \tag{6.4}$$

This model includes the background electronic noise spectral density v_e^2 in V^2/Hz measured at the output of the detector, and the relative uncertainty ϵ introduced by the numerical integration or pulse-fitting method. These terms were not previously accounted for in the analysis software. Here s_{bg} is the mean background signal level in volts produced by background plasma light, and τ_{int} is the integration time of the integration or pulse-fitting method. The integrated background signal can be defined as $S_{bg} = s_{bg}\tau_{int}$. The integration time determines the amount of background noise that affects the pulsed signal, and depends on the pulse shape and the integration or fitting method used [4, 10].

The photonic noise contribution to the signal variance is:

$$\sigma_{phe}^2 = GMF(S + S_{bg}). \tag{6.5}$$

It arises in the following way. The variance σ^2_{phe} of the number of primary photoelectrons N_{phe} created in the APD is given by $\sigma^2_{phe} = N_{phe}$ due to quantum counting statistics [11]. This variance is multiplied by the APD noise enhancement factor F, yielding an effective variance [12]:

$$\sigma^2_{phe,eff} = FN_{phe}. \tag{6.6}$$

The relations between primary photoelectron number and the signal in volt-seconds (for both the mean and variance) are:

$$\frac{\sigma^2}{G^2M^2} = \sigma^2_{phe,eff} \tag{6.7}$$

$$\frac{S}{GM} = N_{phe}. \tag{6.8}$$

Applying these relations to Equation 6.6 leads to Equation 6.5.

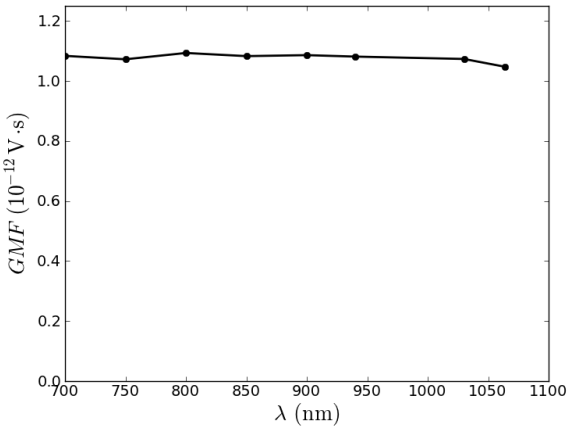

Figure 6.5: The noise term GMF is measured to be constant over wavelength for an APD module from the MST TS system. The measurement was made with a DC light source, which provides $Var(s_{bg})/\langle s_{bg}\rangle = GMFB$, where B is the amplifier bandwidth [4]. The value $B^{-1} = 47$ ns was assumed.

It is not clear *a priori* that the avalanche gain M and noise enhancement factor F would be wavelength-independent. However, the 'reach-through' design of the APDs (EG&G C30956E [3]) used in the MST TS system minimizes the variation of M over wavelength. The 'reach-through' structure physically separates the absorption region from the avalanche region, so that the penetration depth of the photons before absorption (which is wavelength-dependent) has less influence on the avalanche gain experienced by the resulting photoelectrons [12]. This also helps keeps F constant, since F is a function of M. In fact, the noise term GMF has been measured to be constant over the range of 700-1064 nm for an APD from the MST TS system (Figure 6.5). Thus, there is fortunately no need to consider the incident spectrum when modeling the detector noise. A very detailed experimental characterization of the noise properties of an EG&G APD of the same design is found in Ref. [13].

To summarize this section, the important quantities that must be obtained from a calibration are the spectral instrument functions $I = GM\eta(\lambda)T(\lambda)$ as a function of wavelength, and the noise model coefficients ϵ, GMF, v_e^2, and τ_{int} which are wavelength-independent.

6.3 Improvement of the system model

It is desirable to measure GM in order to isolate $R(\lambda) \equiv T(\lambda)\eta(\lambda)$ out of I and F out of GMF:

$$F = \frac{GMF}{GM} \tag{6.9}$$

$$R(\lambda) = \frac{I(\lambda)}{GM} = T(\lambda)\eta(\lambda). \tag{6.10}$$

This normalization makes for more direct comparison between polychromators and APD modules, and may help identify anomalies. It is not necessary for processing the data to obtain T_e and its uncertainty.

Rather than using GM, the previous calibration procedures and analysis software were based on normalizing by the end-to-end gain $G_{APD}(\lambda_{cal}) = GM\eta(\lambda_{cal})$ [14], yielding instead:

$$\frac{F}{\eta(\lambda_{cal})} = \frac{GMF}{G_{APD}(\lambda_{cal})} \tag{6.11}$$

$$\frac{R(\lambda)}{\eta(\lambda_{cal})} = \frac{I(\lambda)}{G_{APD}(\lambda_{cal})} \tag{6.12}$$

In the previous MST TS notation, these quantities were referred to as F/QE and 'transmission' function. The calculations in the analysis software were then performed in terms of the effective number of Thomson-scattered photons N_{ph} arriving at the detector. The effective photon number was defined by:

$$N_{ph}(\lambda_{cal}) = \frac{S}{GM\eta(\lambda_{cal})} \tag{6.13}$$

$$= \int d\lambda \nu(\lambda) \frac{R(\lambda)}{\eta(\lambda_{cal})}. \tag{6.14}$$

This choice of normalization was motivated by the importance of the quantum counting noise, expressed in Ref. [14, eq. 2] as

$$SNR = \sqrt{\frac{N_{ph}(\lambda_{cal})\eta(\lambda_{cal})}{F}}. \tag{6.15}$$

These equations were somewhat ambiguous because the evaluation of η and G_{APD} at λ_{cal} (and hence the dependence of N_{ph} on the choice of λ_{cal} as well) were not maintained explicitly

in the notation of Ref. [14]. This resulted in confusion about the wavelength-dependence of the photonic noise.

Rather than formulating the problem in terms of the number of incident photons, it is more useful to use the number of primary photoelectrons produced in the APD (following absorption of the incident photons):

$$N_{phe} = \frac{S}{GM} \tag{6.16}$$

$$= \int d\lambda R(\lambda)\nu(\lambda) \tag{6.17}$$

This quantity is well-defined and meaningful, unlike N_{ph} which is a function of the (arbitrary) choice of λ_{cal}. The SNR is written more naturally in terms of N_{phe} as well [see Equation 6.6]:

$$SNR = \sqrt{\frac{N_{phe}}{F}} \tag{6.18}$$

$$= \sqrt{\frac{S}{GMF}}. \tag{6.19}$$

The specious wavelength-dependence via η is absent, because the observed quantity $S = GMN_{phe}$ already contains the effect of η. The finite quantum efficiency means that the number of photoelectrons N_{phe} produced by the absorbed photons is always smaller than the number of incident photons. This smaller number of quanta represents the real bottleneck in terms of information transmission, and puts the upper limit on the SNR.

6.4 Alternative gain calibration

The calibration procedure to find G_{APD} entailed significant effort. A set of three APD modules and their power supplies were shipped to the Canadian National Research Council's Institute for National Measurement Standards (INMS) to be calibrated [8]. The calibration of the remaining detectors against these reference detectors was also time-consuming and hence has been done infrequently (approximately every other year). It required disconnecting and removing the polychromators, removing the APD modules, and placing them five at a time on the cooling block for calibration for an hour. Sometimes the detector temperature stability during a calibration was poor, necessitating second or third attempts. With 138 APD modules, the process took several weeks. Because the noise calibration was understood to depend upon finding the absolute photon number, in the past the noise calibration has only been done as part of the gain calibration process. The combined process was referred to as the 'absolute calibration.'

The absolute calibration procedure can be replaced by two separate, easier procedures. First, the noise calibration can be conducted *in-situ* without an absolute reference detector, as demonstrated in the next section. Second, the gain GM may be measured instead of $GM\eta(\lambda_{cal})$. This calibration is optional, because the value of GM on its own does not play a direct role in the quality of the T_e measurements. As shown in Section 6.2.2, the noise and spectral calibrations are all that is needed. The gain calibration serves only as a way to make the other calibration data easier to interpret.

The combined APD and preamplifier gain GM can be found by measuring G and M separately. The preamplifier gain $G = G_v Rq$ is found by removing the APD from the preamplifier circuit and injecting a known current while measuring the output voltage. The avalanche multiplication ratio M can be measured in the following way [15]. The avalanche multipli-

cation ratio M goes to unity when the APD bias is lowered below the avalanche threshold so that the APD photocurrent consists only of the primary photoelectrons. By measuring the output signal at low bias (when $M = 1$) and at the nominal bias voltage, and taking the ratio, the multiplication factor M can be found. This procedure does involve removing the APD modules from the polychromators, which is time-intensive, although less so than the absolute calibration procedure.

6.5 Improved noise calibration

The noise model, Equation 6.4,

$$\sigma^2 = \epsilon^2 S^2 + GMFS + GMFs_{bg}\tau_{int} + v_e^2\tau_{int}$$

relates the variance σ^2 of the signal to its mean S and to background sources. By applying a pulsed light source with a range of amplitudes to an APD, while measuring the mean and variance of the APD signal at each amplitude, the model coefficients ϵ, GMF, and $v_e^2\tau_{int}$ can be found from a quadratic polynomial fit between σ^2 and S. This is similar to the method used in [15]. Next, with a constant pulse amplitude, several levels of background light can be applied to yield $GMF\tau_{int}$ from a linear scaling of σ^2 with s_{bg}. Variability of the output pulse amplitude from the pulsed calibration source scales in the same way as the integration error, however. Therefore, low source variability is important when calibrating the detector noise sources. Note that it is unnecessary to use a reference detector, because the model is specified in terms of the measured signal S and its variance σ^2.

As mentioned in Section 6.4, the noise calibration method used in the past had several drawbacks. First, it was integrated into the absolute calibration, which required the APDs to

be removed from the polychromators for calibration. Second, it only evaluated the photonic noise. Third, the previous calibration was only done with two amplitudes: zero, and a small but finite amplitude ($\approx 10^{-9}\,\mathrm{V}\cdot\mathrm{s}$) typical of TS measurement signals. The small amplitude made it very difficult to distinguish the photonic noise contribution from the background (see [7, fig. 2.14] and surrounding discussion). This necessitated the acquisition of 10^5 pulses to achieve satisfactory results. Finally, the calibration analysis code used numerical integration instead of pulse-fitting to find the pulse amplitude. Thus, the calibration did not yield useful values for τ_{int} or ϵ (which depend on the fitting or integration method [4]). The numerical integration method has a longer τ_{int} than pulse-fitting, incurring larger background noise contributions to the total signal variance. This exacerbated the problem of distinguishing the photonic noise from the electronic background noise.

The improved noise calibration can be carried out *in-situ* using the daily calibration system. The daily calibration system was designed to check the functionality of the detectors and to monitor for drift in detector gain over time [6, sec. 2.3.3]. It consists of three pulsed light sources illuminating three large integrating spheres. The sources are Omnipulse PLDD-50-SP driver boards powering Osram SFH4545 LEDs, which emit at 940 nm. This wavelength was chosen because it is near the peak sensitivity of the APDs (refer to Figure 6.4).

Each APD detector on each polychromator is coupled to an integrating sphere via fiber optics. These fibers bypass the interference filters and shine on each APD obliquely. It was discovered that APDs on several polychromators were recessed such that the light from the daily calibration fibers did not reach them. Fixing this required adjustment of the APD alignment on some polychromators.

The daily calibration sources can supply relatively large signals to the APDs, up to $1.5 \times 10^{-8}\,\mathrm{V}\cdot\mathrm{s}$, more than ten times larger than the signals used in the past for noise calibration.

Due to the design of the drivers, the amplitude of the pulses cannot be adjusted electronically. However, it is sufficient to install neutral density filters of varying attenuation to achieve several different pulse amplitudes. The pulse-to-pulse amplitude variation of these sources is very low, with an upper bound of 0.8% [7].

Figure 6.6 shows the variance σ^2 versus the mean, S, of the signal from a trial calibration. Both the AC and DC outputs of the preamplifier unit were calibrated. The AC output has a larger background variance because the delay line subtraction adds another source of noise (the time-shifted background signal). The quadratic dependence of the variance for the standard pulse-fitting method arises from the integration error $\epsilon \approx 1.4\%$. The pulse width is only a few times the digitizer period (10 ns), leading to large relative fitting error due to the variation of the pulse arrival time with respect to the digitizer sampling times. However, typical pulse amplitudes during TS diagnostic operation are low ($\lesssim 2 \times 10^{-9}\,\mathrm{V\,s}$), such that the integration error is not a dominant error source. Instead, the reduction in background signal provided by the pulse-fitting method is more important at these small signal amplitudes, compared to numerical integration. Interestingly, however, the numerical integration method does not suffer a large integration error from the under-sampling problem, perhaps because it is agnostic about the pulse shape.

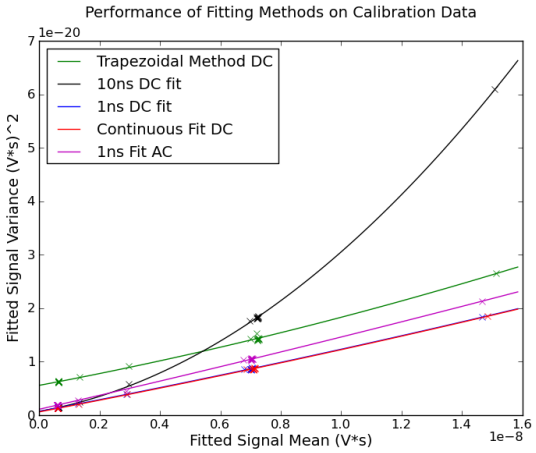

(a)

Best Fit	ϵ	GMF	τ_{int}
Method, Channel	%	$10^{-12}\,\mathrm{V}\cdot\mathrm{s}$	ns
Trapez., DC	0.45	1.06	256
10 ns Fit, DC	1.41	1.00	33
1 ns Fit, DC	0.29	1.08	32
Continuous Fit, DC	0.29	1.08	28
1 ns Fit, AC	0.24	1.29	51

(b)

Figure 6.6: (a) Scaling of the signal variance versus the mean applied signal for various methods of integrating or fitting the pulsed signal. Both the AC and DC output channels of the preamplifier were considered. The lines are polynomial fits to the data points, yielding the coefficients of the model. (b) The resulting noise model coefficients from the polynomial fits. This figure is reproduced from [4]. The copyright is held by IOP, which grants the author the right to reproduce the article (all or part) in a research thesis or dissertation.

The AC output (digitized at 1 GHz) also does not exhibit large integration error, due to higher time resolution. The AC signal has a larger effective integration time due to the doubled impact of the background noise via the delay-line subtraction of the background level. The lowest error overall was achieved by using a characteristic pulse with higher time resolution to fit the DC output, showing that the digitizer under-sampling of the pulse shape can be overcome. Also note that the daily calibration source variance is very small, which makes it possible to identify the other error sources. The upper bound is now 0.24% relative fluctuations for these pulsed sources.

6.6 Improved spectral calibration

The accuracy of the temperature measurement relies on the accuracy of the calibrations of the instrument functions I_i. Monte Carlo simulations demonstrate that errors of a few percent in calibrating I_i for the different wavelength channels on a polychromator result in systematic T_e errors of roughly the same percentage (Figure 6.7). As noted in Chapter 2, systematic errors (which are different for each polychromator) cause unevenness in the mean temperature profile. Present systematic T_e errors are roughly 5%, agreeing with the degree of reproducibility of the previous spectral calibration method. Reducing errors to $< 1\%$ could enable better understanding of the magnetic structures in MST, particularly the nature of $n = 5$ perturbation in the core (as discussed in Section 2.3.1).

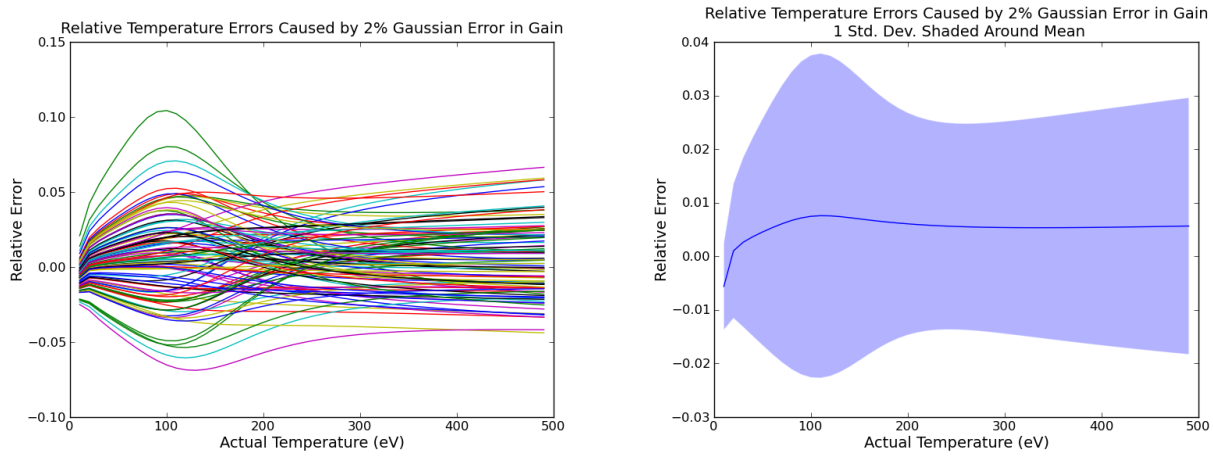

(a) **(b)**

Figure 6.7: (a) Simulation of relative T_e error resulting from introducing 2% Gaussian noise to the relative amplitudes of the instrument functions I_i on a polychromator. Each trace shows the result of a particular set of random errors imposed on the instrument function. The random errors in calibration result in T_e-dependent systematic errors if the erroneous instrument functions are used to calculate T_e. (b) The mean (solid line) and standard deviation (shaded) of the resulting systematic error distribution. The 2% relative error applied to the instrument functions results in roughly a 2-3% systematic error in the resulting temperature values.

The spectral calibration process requires a calibrated reference detector and a stable light source with a broad output spectrum. The source output is passed through a SpectraPro 500i scanning monochromator (with focal length $f = 0.5\,\mathrm{m}$, and a numerical aperture $NA = 0.06$). The monochromator transmits a narrow spectrum with a selectable width and central wavelength. The light is then coupled using fiber optics to the reference detector and the polychromator under calibration. The monochromator central wavelength is scanned over the sensitive range of the detectors, producing the signal $S_i(\lambda)$ from each detector on the polychromator. The instrument function $I_i(\lambda)$ is determined for each wavelength channel on the polychromator as

$$I_i(\lambda) = \frac{S_i(\lambda)}{S_{ref}(\lambda)} I_{ref}(\lambda), \tag{6.20}$$

where the subscript 'ref' refers to the reference detector, and $I_{ref}(\lambda)$ is determined from the calibration of the reference detector.

The previous calibrations relied on a tungsten halogen lamp to produce a broad spectrum of light. There were several disadvantages to using the tungsten source. First, the output was continuous rather than pulsed. This meant that only the DC output of the detector could be calibrated, since the AC output is zero in response to a static signal. In order to obtain the signal amplitude, it is necessary to subtract the voltage output by the detector with the source off (the 'dark voltage') from the voltage with the source turned on. The source could be blocked manually by closing a shutter. This was done for a short period of time at the end of a monochromator wavelength scan (lasting about 20 minutes). However, it was discovered that the dark voltage of an APD module could drift by a fraction of a millivolt on this time-scale. Since the signal itself was only a few millivolts, this drift was unacceptably large.

It is also possible that some of the spectral calibration variability was due to instability in the source output itself, although this was not quantified. Because the optical signal was too weak to be split using an integrating sphere, the entire signal was directed to the polychromator on one scan, and then to the reference detector on a second scan. This meant that drift in the source intensity over time would cause inaccuracies in the calibration.

A better solution was found in the form of a supercontinuum (SC) light source. The source (NKT Photonics SuperK COMPACT) produces a 1.5-ns pulse of light containing a broad spectrum of wavelengths covering the necessary 700-1200 nm range. The SC source contains a strongly nonlinear optical fiber that converts a narrow-band laser pulse at 1064 nm into a broader spectrum. The source spectral power density (0.06-0.07 mW/nm over the 600-1400 nm range according to manufacturer) is sufficiently high to allow the use of an integrating sphere (Thorlabs IS200) to distribute the optical signal from the output of the monochromator. This allows both a reference detector and a polychromator to observe the output simultaneously, eliminating slow drifts of the source intensity as a potential source of error. Even with the signal attenuation due to the integrating sphere (the estimated transmission efficiency is 5×10^{-4}), the resulting signals are up to $3 \times 10^{-9}\,\mathrm{V\,s}$, which is sufficient to achieve good SNR with only 100 pulses acquired.

The polychromator is coupled to the integrating sphere using a fiber similar to the ones used to convey the scattered light from the collection optics to the polychromators. This fiber was not part of the previous calibration methods. Inclusion of this fiber in the calibrations is considered an improvement, since the transmission of the fiber is part of the overall transmission function. There is a dip in the transmission near 910 nm, corresponding to an absorption peak from impurities in the fiber. The reference detectors (described below) are mounted directly to the integrating sphere, so they are not affected by any fiber transmissions.

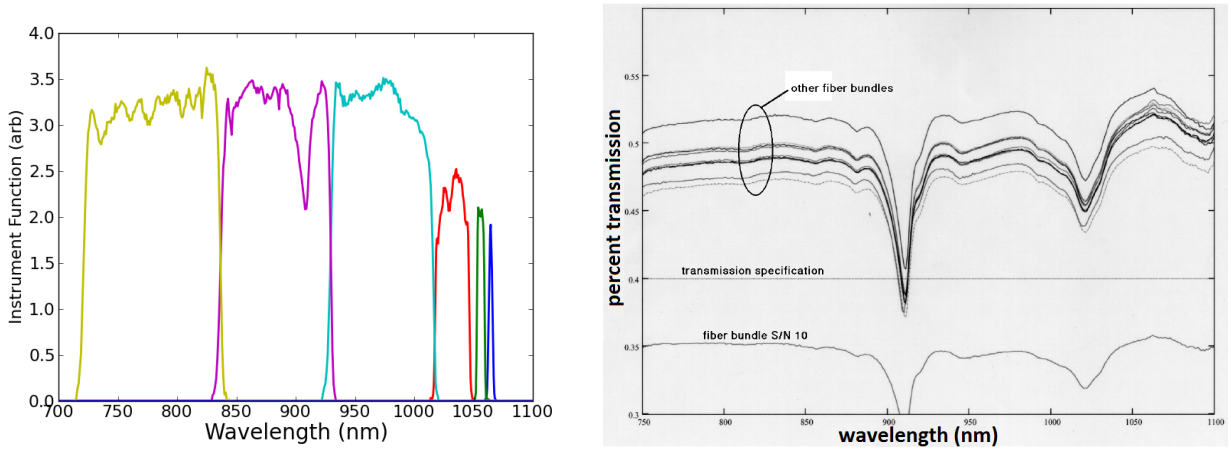

(a) (b)

Figure 6.8: (a) Instrument function of a polychromator showing the dip in transmission at 910 nm. (b) The dip results from the inclusion of the fiber transmission shown here.

The reference detectors now being used are Thorlabs unbiased photodiodes. One detector (model number FDS100-CAL) is made of silicon (Si), the other (model number FGA21-CAL) of indium gallium arsenide (InGaAs). The calibration data is available at integer multiples of 10 nm, ranging from 800-1700 for the InGaAs photodiode to 350-1100 nm for the Si photodiode (Figure 6.9). The use of the InGaAs photodiode was driven by the implementation of a new long-wavelength filter (spanning 1120 to 1180 nm) on a trial basis on a several of polychromators (see Figure 6.10).

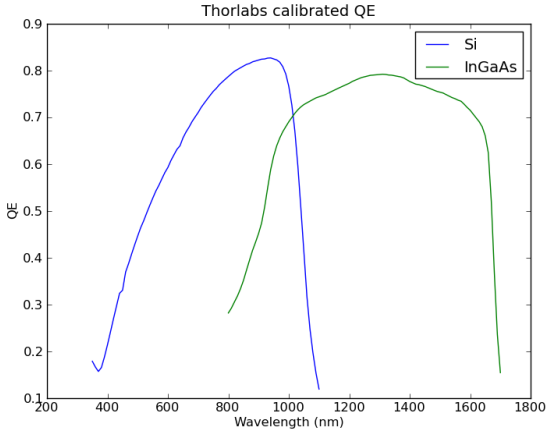

Figure 6.9: Quantum efficiency of the two Thorlabs diodes according to the calibration data supplied by the manufacturer.

The photodiodes are unbiased, so they lack the internal gain $M \sim 100$ of the APDs, resulting in a smaller output current. The photocurrent (several tens of picoamps) is measured using a Keithley 614 electrometer, whose analog output is digitized on the Acqiris digitizer. The output current is time-averaged by the electrometer over the 1 kHz repetition rate set for the SC source during spectral calibrations, resulting in a DC output (rather than resolving the individual pulses). This means that it is necessary to acquire a few samples of data on the Acqiris from the electrometer with no applied signal in order to account for voltage offsets. This is done by halting the monochromator at 600 nm (where the reference detector output goes to zero) for several samples at the beginning of a wavelength scan.

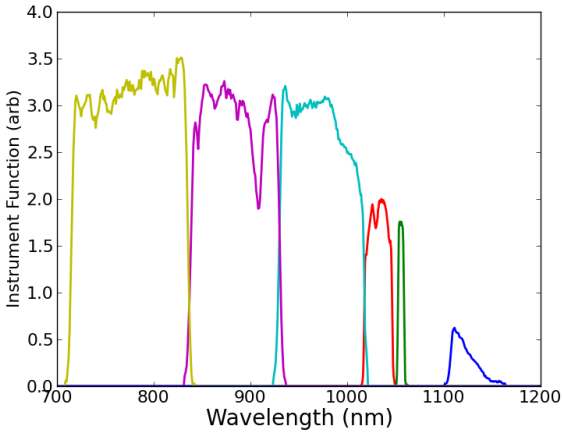

Figure 6.10: Instrument function of a polychromator with long-wavelength filter installed in place of the filter at 1064 nm. The detector efficiency η decreases rapidly above 1064 nm (see Figure 6.4), causing the long-wavelength channel (blue) to be less sensitive than the others, even though the filter transmission is comparable.

The two reference detectors disagree by several percent for wavelengths below 900 nm, so the Si detector (being more similar to the Si APDs) was used for all calibrations except the long-wavelength filters. The agreement between Si and InGaAs detectors was also found to be poor in the past [14]. There is also an overall scale factor of about 2.5 between the calibrations from the Si photodiode and the InGaAs photodiode, which was corrected for in the long-wavelength filter calibrations.

It would be preferable to use a single photodiode for the entire calibration. However, it was decided that the Si reference photodiode was more reliable in the short-wavelength range, which necessitated the split calibration for the long-wavelength filters. If the long-wavelength filters become a permanent part of the system, it would be worth considering an improved reference photodiode scheme. Making use of the set of APD modules that were calibrated at INMS would also be desirable, although the drop in signal above 1064 nm could make the long-wavelength channel calibrations noisy. A large-diameter optical fiber with minimal

structure in its transmission function would be needed to transport light from the integrating sphere to the reference APD modules on the cooling block. The APD modules must be on the cooling block for temperature regulation, unlike the Thorlabs unbiased diodes which are less temperature-sensitive and can be mounted directly to the integrating sphere.

The new calibration method utilizing the SC source produces reproducible spectral calibrations that meet the goal of reducing the relative error in the amplitudes of instrument function between channels to the sub-percent level. This is illustrated by a series of repeated calibrations taken on single day for a particular polychromator in Figure 6.11. The first scan had a larger deviation from the others because the system had not fully come to thermal equilibrium following the start-up of the SC source. The subsequent calibrations illustrate that the statistical variation in the spectral calibration is below 1%. The systematic error in the temperature determination should be reduced to 1% or less based on this finding, meeting the goal that was set to enable improved measurements of the equilibrium temperature gradient.

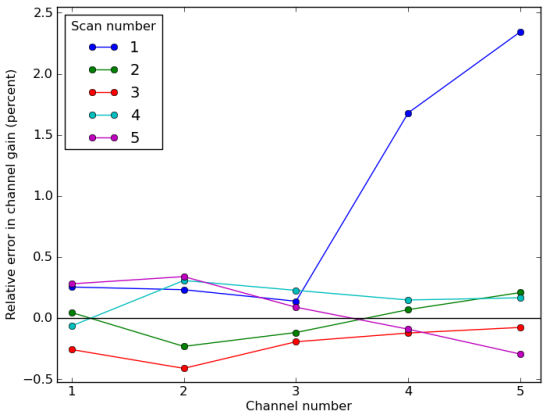

Figure 6.11: The deviation of the overall amplitude of the spectral response of each channel on one polychromator during repeated spectral calibrations.

References

[1] J. F. Monahan, *Numerical Methods of Statistics*, 2nd ed. (Cambridge University Press, 2011) p. 258.

[2] T. N. Carlstrom, J. C. DeBoo, R. Evanko, C. M. Greenfield, C.-L. Hsieh, R. T. Snider, and P. Trost, Review of Scientific Instruments **61**, 2858 (1990).

[3] EG&G Canada, *Photodiode C30954E, C30955E, C30956E Data Sheet*, Tech. Rep.

[4] L. A. Morton, E. Parke, and D. J. Den Hartog, Journal of Instrumentation **8**, C11003 (2013).

[5] R. O'Connell, D. J. Den Hartog, M. T. Borchardt, D. J. Holly, J. A. Reusch, and H. D. Stephens, Review of Scientific Instruments **79**, 10E735 (2008).

[6] H. D. Stephens, *Electron Temperature Structures Associated With Magnetic Tearing Modes in the Madison Symmetric Torus*, Phd thesis, University of Wisconsin - Madison (2010).

[7] E. Parke, *Diagnosis of Equilibrium Magnetic Profiles, Current Transport, and Internal Structures in a Reversed-Field Pinch Using Electron Temperature Fluctuations*, Phd thesis, University of Wisconsin - Madison (2014).

[8] E. Parke, D. J. Den Hartog, L. A. Morton, H. D. Stephens, C. P. Kasten, J. A. Reusch, W. H. Harris, M. T. Borchardt, A. F. Falkowski, N. C. Hurst, A. Plunkett, and J. Goglio, Review of Scientific Instruments **83**, 10E324 (2012).

[9] D. G. Nilson, D. N. Hill, J. C. Evans, T. N. Carlstrom, C. L. Hsieh, and R. E. Stockdale, 11th Topical Conference on High-Temperature Plasma Diagnostics **68**, 704 (1997).

[10] P. J. Windpassinger, M. Kubasik, M. Koschorreck, A. Boisen, N. Kjærgaard, E. S.

Polzik, and J. H. Müller, Measurement Science and Technology **20**, 055301 (2009), arXiv:0903.3398 .

[11] Z. Liu, W. Hunt, M. Vaughan, C. Hostetler, M. McGill, K. Powell, D. Winker, and Y. Hu, Applied Optics **45**, 4437 (2006).

[12] P. Webb, R. McIntyre, and J. Conradi, RCA Review **35**, 234 (1974).

[13] F. Laforce, Proc. SPIE **7212**, 721210 (2009).

[14] H. D. Stephens, M. T. Borchardt, D. J. Den Hartog, A. F. Falkowski, D. J. Holly, R. O'Connell, and J. A. Reusch, Review of Scientific Instruments **79**, 10E734 (2008).

[15] L. Jiangui, A. Fremout, P. Bruyndonckx, S. Tavernier, J.-F. Loude, and C. Morel, in *Nuclear Science Symposium Conference Record, 2001 IEEE*, Vol. 2 (2001) pp. 873–875.

7 Conclusion

All information looks like noise until you break the code.

— Hiro in Neal Stephenson's *Snow Crash*

Turbulence and transport within and around large magnetic islands have been studied in this thesis through the use of high-resolution plasma diagnostics. The high-repetition rate Thomson scattering diagnostic for the MST RFP has provided evidence of hot remnant tearing mode magnetic islands, including a single-shot observation of a hot island structure. The beam emission spectroscopy system at the DIII-D tokamak was used to map out turbulence intensity around a static magnetic island. Together these experiments have shed light on the interesting and important issues of turbulence and transport in the topology of large magnetic islands. Section 7.1 reviews the main physics results in the context of previous research, while Section 7.2 outlines possibilities for future work.

7.1 Summary of key physics results

Chaos-induced transport in remnant tearing mode magnetic islands

In prior work, temperature fluctuations measured in MST by the high-repetition-rate Thomson scattering system were correlated with tearing mode magnetic fields. The temperature

fluctuations for the $n = 6$ and higher modes agreed with the isothermal model for the tearing mode islands [1]. It was recognized that the proximity of the adjacent islands would likely cause chaos and result in remnant islands [2]. This raised the question of how the remnant islands produced large temperature fluctuation signatures. In Chapter 2, a closer examination of the higher harmonics of the $n = 6$ temperature fluctuations showed evidence for confinement of heat within the remnant $n = 6$ island. This finding made the issue of remnant island confinement even more interesting.

Despite the use of Bayesian techniques, ensemble analyses are ultimately limited by plasma irreproducibility. In Chapter 3, the observation of a large hot remnant island during a single discharge using the new Fast Laser [3, 4] for Thomson scattering provided the right conditions to answer the question of confinement within a chaotic island-like structure. Despite comprising primarily chaotic field lines, the chaotic structure can develop temperature peaking due to ohmic heating. Such hot chaotic $n = 6$ structures may be common in MST, based on the ensemble analysis and the (much smaller) Fast Laser dataset. Magnetic fields with a low degree of chaos may exhibit reduced transport compared to highly stochastic magnetic fields. Reduction of transport is not by itself conclusive evidence that closed flux surfaces are restored as in a remnant island. Accurate magnetic field modeling is necessary to determine the degree of magnetic chaos in the plasma. Confidence in the modeling process combining MSTFIT, DEBS and MAL [5, 6] is increased by the good agreement of the $n = 6$ magnetic island flux surface shape with the shape of the observed hot island-like temperature structure. These results also highlight the power of single-shot observations enabled by the Fast Laser.

Ion-scale turbulence in large static magnetic islands

While preliminary, the results of the experiment on DIII-D presented in Chapter 4 confirm some qualitative expectations about the effect of large imposed magnetic islands on ion-scale electron density turbulence. External control coils were used to scan a large a $m, n = 2, 1$ magnetic island past multiple diagnostics. The beam emission spectroscopy (BES) diagnostic [7] provided high-resolution two-dimensional maps of the turbulence intensity and frequency spectra around the island. The island was much wider than the turbulence correlation length in the absence of an island. As expected, the turbulence intensity was decreased at the O-point and increased at the X-point, compared to the intensity without a magnetic island. The turbulence intensification at the X-point was located just inboard of the inferred rational surface. When the control coils failed to induce a large island due to increased plasma rotation, the effect of the applied magnetic perturbation on turbulence was much smaller and more radially uniform.

7.2 Suggestions for future research

All but one of these suggestions are oriented toward research on MST. The DIII-D experimental data obviously requires further analysis. For MST, there is significant untapped potential for use of the Fast Laser to capture further single-shot island observations. The improved Thomson scattering calibrations should also enable the $n = 5$ mode to be studied in greater detail. The model for temperature fluctuations should be extended to incorporate island heating and asymmetry.

Further hot $n = 6$ island observations and modeling in MST

Based on the ensemble analysis and the small set of observations from usage of the Fast Laser, hot $n = 6$ island-like structures appear to be a relatively common occurrence in MST. With the right plasma conditions, it may be possible to collect a large number observations using the Fast Laser. The prevalence of the particular magnetic field situation analyzed in Chapter 3 is probably lower than that of hot island-like structures in general. Applying the power balance and chaotic transport analyses used in this thesis to a larger set of hot structures would improve understanding of this phenomenon and probe the limits of the chaotic transport model. In particular, remnant islands with significant volumes of closed flux surfaces may lead to consideration of other causes of transport. Comparison of the observations with more detailed chaotic field transport simulations such as those of Refs. [8, 9] would help to confirm the conclusions drawn from the magnetic field line spreading estimate used in this work.

Further analysis of DIII-D island turbulence and comparison to simulations

Much work remains to be done in analyzing the data from the DIII-D island turbulence experiment described in Chapter 4. Data from the BES diagnostic contains information not only about the turbulence intensity, but also about the turbulence wavenumber spectrum, correlation lengths, and poloidal velocities. Data from other diagnostics needs analysis as well. In particular, the electron cyclotron emission measurements of T_e should be analyzed to infer the $m, n = 2, 1$ island flux surfaces, in order to better locate the BES measurements with respect to the island. Comparison against dedicated gyrokinetic turbulence simulations using the specific island topology and gradients from the experiment would be very useful,

for testing the simulations as well as for interpreting the experimental data.

Search for hot islands in PPCD using the Fast Laser

The highly dynamic environment of a PPCD discharge does not lend itself well to ensemble-analysis for T_e fluctuation studies. Pairing the Fast Laser with soft X-ray (SXR) tomography would allow simultaneous single-shot analysis of the highly-emissive structures observed by SXR [10] but not (so far) by Thomson scattering. This experiment could distinguish whether emissive islands in PPCD are primarily confining impurities or thermal energy.

Structure of the $n = 5$ mode in MST

With the improved spectral calibrations described in Chapter 6, systematic errors should no longer prevent precise Thomson scattering measurements of the mean T_e gradient in the core of MST. This measurement will elucidate the shape of the $n = 5$ magnetic structure. The curvature of the $n = 5$ structure's flux surfaces is linked to the behavior of the q-profile near the magnetic axis, but also contains information about the $n = 5$ magnetic mode itself. It may be possible to answer the long-standing question (mentioned in [1, 2]) of whether the $n = 5$ magnetic structure has a separatrix and hence constitutes a magnetic island.

Model of hot island T_e for parameter inference in MST

In order to properly infer parameters such as rational surface radius, island width, island shape asymmetry, and degree of temperature peaking from ensemble-averaged T_e fluctuations or single-shot observations, a simple mathematical model of the temperature structure is needed. Bayesian parametric inference (such as used in [1]) requires the model to be evaluated

many times in the process of mapping out the probability in parameter space, so the model must execute rapidly. Extension of the model to include island heating should result in more accurate determination of the rational surface in cases where island heating is appreciable, compared to using the isothermal island model to analyze such cases.

References

[1] E. Parke, J. K. Anderson, D. L. Brower, D. J. Den Hartog, W. X. Ding, C. A. Johnson, and L. Lin, Physics of Plasmas **23**, 056108 (2016).

[2] H. D. Stephens, D. J. Den Hartog, C. C. Hegna, and J. A. Reusch, Physics of Plasmas **17**, 056115 (2010).

[3] D. J. Den Hartog and W. C. Young, Journal of Instrumentation **10**, C12008 (2015).

[4] W. C. Young and D. J. Den Hartog, Journal of Instrumentation **10**, C12021 (2015).

[5] T. M. Biewer, C. B. Forest, J. K. Anderson, G. Fiksel, B. Hudson, S. C. Prager, J. S. Sarff, J. C. Wright, D. L. Brower, W. X. Ding, and S. D. Terry, Physical Review Letters **91**, 045004 (2003).

[6] J. A. Reusch, J. K. Anderson, D. J. Den Hartog, F. Ebrahimi, D. D. Schnack, H. D. Stephens, and C. B. Forest, Physical Review Letters **107**, 155002 (2011).

[7] G. R. McKee, R. J. Fonck, D. K. Gupta, D. J. Schlossberg, M. W. Shafer, and R. L. Boivin, Review of Scientific Instruments **77**, 10F104 (2006).

[8] D. Del-Castillo-Negrete and L. Chacón, Physics of Plasmas **19**, 056112 (2012), arXiv:arXiv:1007.4579v1 .

[9] S. R. Hudson and J. Breslau, Physical Review Letters **100**, 095001 (2008).

[10] P. Franz, L. Marrelli, P. Piovesan, B. E. Chapman, P. Martin, I. Predebon, G. Spizzo, R. B. White, and C. Xiao, Physical Review Letters **92**, 125001 (2004).

8 Appendix: Coordinate systems for MST, DEBS, and MAL

> *[N]ew data that we insist on analyzing in terms of old ideas (that is, old models which are not questioned) cannot lead us out of the old ideas.*
>
> — E. T. Jaynes, Preface to *Probability Theory: The Logic of Science* [1]

The traditional MST coordinate system, as exemplified in the MST port map [2], is a left-handed coordinate system when written as (r, θ, ϕ). However, the direction of ϕ is in agreement with the conventional axial coordinate system shown in Figure 8.1a. In the vertical cylindrical coordinate system, R is the major radius, Z is the vertical distance above the mid-plane, and ϕ is the toroidal angle. Because of this identification, and also because the toroidal magnetic array is labeled in terms of this angle, it is most natural to keep ϕ as defined in this manner. Thus, in order to make (r, θ, ϕ) a right-handed system, θ must be reversed from the usual MST convention. The resulting coordinate system is illustrated in Figure 8.1b. The explicit relations between the coordinates used in this thesis (left) and the conventional MST coordinates (right) are:

$$\theta = -\theta_{portmap} \tag{8.1}$$

$$\phi = \phi_{portmap}. \tag{8.2}$$

The conversion from the cylindrical coordinate system in Figure 8.1a to the coordinate toroidal system used in this thesis is:

$$r \equiv \sqrt{Z^2 + (R - R_0)^2} \tag{8.3}$$

$$\theta \equiv \tan^{-1}\left(\frac{Z}{R_0 - R}\right) \tag{8.4}$$

$$\phi \equiv \phi \tag{8.5}$$

Another reason for using this (r, θ, ϕ) convention is to ease the comparison with periodic cylindrical approximations to the torus. As shown in Figure 8.1b by the diagram labeled 'Periodic Cylinder', the process of cutting the torus at $\phi = 0$ and unwrapping it to form a cylinder thus creates a natural mapping to the usual cylindrical coordinate system:

$$(r, \theta, = \phi/R_0),$$

with the boundary condition that $Z = 0$ and $Z = 2\pi R_0$ refer to the same location. This is how the DEBS MHD simulations, which use a periodic cylindrical geometry, are interpreted as approximating the geometry of a torus (MST). Finally, it should be noted that the MAL field line tracing code uses the same convention as the MST port map when run in periodic cylindrical geometry. In retrospect, it would have been easier to use the convention (r, ϕ, θ)

which makes the port map coordinates right-handed. However, one strong motivation for adopting the convention used in this thesis is that it is based on the diagram of Den Hartog and McCollam [3], which is a useful point of reference for a variety of directional quantities (fields, currents, flows, and more).

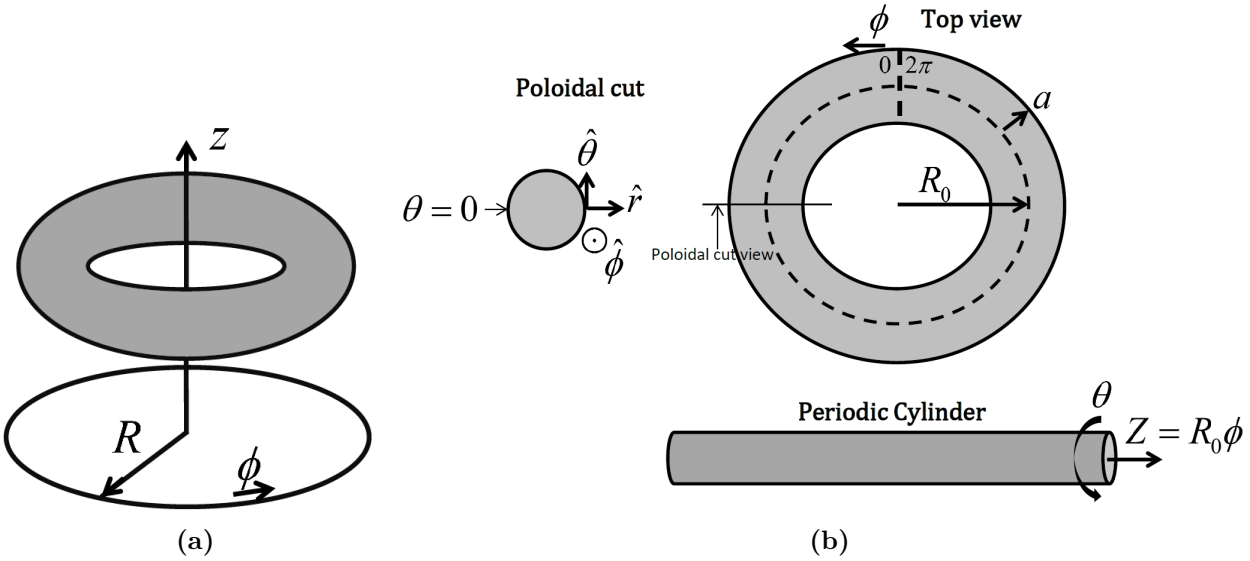

Figure 8.1: A diagram illustrating the coordinate system used in this thesis for MST and a unwrapped cylindrical approximation to it, used in simplified simulations of plasma behavior. This diagram is based on a similar one authored by Den Hartog and McCollam [3]. The poloidal angle θ is referenced from the outboard midplane, and the toroidal angle ϕ is referenced from the poloidal gap (enclosed by the iron transformer core).

References

[1] E. T. Jaynes, *Probability Theory: The Logic of Science*, edited by G. L. Bretthorst (Cambridge University Press, 2003).

[2] P. J. Weix, *MST Port Map*, Tech. Rep. (2013).

[3] D. J. Den Hartog and K. J. McCollam, *Directions in MST*, Tech. Rep. (2010).